NSF Grant ATM-9726464
National Science Foundation, and
NASA TRMM Grant NAG5-4754
National Aeronautics & Space Administration

CLASSIFICATION OF TROPICAL PRECIPITATION REGIMES: A COMPARATIVE ANALYSIS OF DISDROMETER, PROFILER, AND MULTI-PARAMETER RADAR MEASUREMENTS

by Larry R. Belcher, Jr.

Colorado State University

DEPARTMENT OF ATMOSPHERIC SCIENCE

PAPER NO. **698**

CLASSIFICATION OF TROPICAL PRECIPITATION REGIMES: A COMPARATIVE ANALYSIS OF DISDROMETER, PROFILER, AND MULTI-PARAMETER RADAR MEASUREMENTS

by

Larry R. Belcher, Jr.

Department of Atmospheric Science

Colorado State University

Fort Collins, CO 80523

Research Supported by

National Science Foundation and National Aeronautics & Space Administration

under Grants ATM-9726464 and NAG 5-4754

Fall 2000

Atmospheric Science Paper No. 698

ABSTRACT OF THESIS

CLASSIFICATION OF TROPICAL PRECIPITATION REGIMES: A COMPARATIVE ANALYSIS OD DISDROMETER, PROFILER, AND MULTI-PARAMETER RADAR MEASUREMENTS

The key objective of the Tropical Rainfall Measuring Mission is to improve estimates of the diabatic heating in tropical precipitation. These improvements depend on the separation of the convective and stratiform components of a precipitating system since each type of precipitation exhibits a different latent heating profile. The objectives of this study were to develop a classification algorithm using multiparameter radar data and apply it and several existing classification algorithms to the TRMM-LBA data set.

We have developed a precipitation classification algorithm that identifies convective precipitation within the storm complex using multiparameter radar data. This identification depends on the intensity and trend of the estimated precipitation rate. The existing algorithms use disdrometer data, Doppler profiler systems, and radar reflectivity to classify precipitation. Comparisons between each algorithm were made, which provided the opportunity to evaluate the performance of each algorithm over a variety of precipitation events.

The disdrometer-based algorithm failed to classify 14% of the data, leading to poor agreement with the remaining algorithms. The profiler-based, reflectivity-based,

and multiparameter algorithms agreed well; of 430 minutes of precipitation, they classified 36%, 41%, and 40% as convective respectively. The total convective area produced by the reflectivity-based algorithms and the multiparameter algorithm agreed reasonably well. Qualitative inspection of the classification results by the reflectivity-based and multiparameter algorithm showed each algorithm's ability to identify the cellular structure within the precipitating events as convective.

Larry Randall Belcher Jr.

Department of Atmospheric Science

Colorado State University

Fort Collins, CO 80523

Fall 2000

ACKNOWLEDGEMENTS

I would like to thank Dr. Steven Rutledge for the guidance and advice he has given to me over the last two years. I would also like to thank Dr. Richard Eykholt and Dr. Graeme Stephens for being on my graduate committee. I thank everyone involved in TRMM-LBA, especially those involved in the operation of the S-pol radar, and NCAR-ATD for making the S-pol data available. I thank the radar meteorology group for their advice, assistance, and friendship, especially Dr. Larry Carey, Dr. Rob Cifelli, Mr. Paul Hein, and Dr. Walt Petersen. This research was supported by the National Science Foundation under the grant ATM-9726464 and National Aeronautics and Space Administration TRMM grant NAG5-4754.

Table of Contents

List of Tables

List of Figures

Chapter 1

Introduction

1.1 Background motivation

The key objective of the Tropical Rainfall Measuring Mission (TRMM) is to develop more accurate diabiatic heating profiles for use in climate and global circulation models (Simpson et al., 1988). This objective should be achievable by using numerical models and the extensive tropical precipitation data set currently provided by TRMM. Houze (1997) describes two principal modes of heating: a convective portion, in which the entire depth of the cloud region is heated; and a stratiform portion, in which the lower levels of the cloud region are cooled while the upper levels are warmed. These two principle modes must be identified and separated in order to obtain accurate estimates of the diabatic heating due to each mode. The partitioning of precipitating systems between convective and stratiform components, as observed by the precipitation radar on TRMM is a central need, in order to obtain accurate estimates of latent heating.

In the convective region of a storm, local ascent of warm, buoyant air parcels in an unstable environment transport mass upward at high velocities (Wallace and Hobbs, 1977). During this ascent, water vapor condenses, leading to the development of a convective cloud, which in turn releases latent heat. As precipitation-sized particles are

transported upward, they increase in size primarily by accretion of liquid water (Houze, 1993). Many of these hydrometeors grow large enough and fall out of the cloud producing convective precipitation at the surface. Smaller particles such as ice crystals and snow, continue to be carried upward and are eventually transported away from the influence of the updraft into a more stable, stratified region of the storm. This is one of several possible sources leading to the production of frozen hydrometeors in the upper portion of the convective cloud, which eventually leads to the formation of a nimbostratus cloud and stratiform precipitation.

The kinematic conditions leading to stratiform precipitation require that the vertical air motions be small, such that ice crystals and snow fall slowly through the cloud (Houze, 1993). During this slow descent, frozen hydrometeors in the upper region of the cloud continue to grow via depositional processes, which in turn releases latent heat. The ice crystals and aggregates formed by coalescence of the ice crystals continue to fall relative to the weak updraft, eventually reaching the melting level. Upon melting, the particles continue to fall toward the surface as rain. The lower levels of the stratiform region are thus cooled due to melting and evaporation.

The processes described above are clearly a simplification of a typical storm, in which convection develops and eventually weakens leading to the formation of stratiform precipitation. In many cases, a convective cell will grow and eventually dissipate, while new cells develop within the same complex leading to the development of a Mesoscale Convective System (MCS; Houze, 1997). A typical MCS produces widespread precipitation with heavy localized precipitation regions in the vicinity of the convective cells. In this case, one or more convective cells could be embedded within a stratified

region with distinct microphysical and kinematic processes occurring in the different regions. The identification of convective cells is not simple due to constant transitions within the storm complex.

The identification and separation of the convective fraction of a storm is essential in order to obtain accurate rain estimates and diabatic heating profiles. Identifying the stratiform region of a storm would seem to be the simplest and most direct method. As described above, frozen hydrometeors descending in the stratiform region melt as they fall through the 0^{o} C level. As melting occurs, the particles take on a liquid coating thus changing their dielectric properties. Since the dielectric constant of water is greater than that of ice, the reflectivity values increase in the melting region leading to a radar bright band. The identification of a bright band would appear to be a direct method of identifying the stratiform portion of the storm. However, since the resolution of a radar volume decreases with distance from the radar due to beam spreading, a bright band may not always be observed even though melting processes are occurring. Furthermore, higher density particles such as graupel can be associated with stratiform precipitation but fail to produce a well-defined bright band. This is due to the fact that the graupel particles are more compact in size than the aggregates and do not produce significant increases in the radar reflectivity. In many cases, the identification of the bright band is not obvious due to complex kinematics as the storm evolves. Even though a bright band may be present, the structure may not be uniformly stratified as depicted in the typical well-behaved case.

This problem motivated researchers to develop algorithms that identify convective regions of a storm. One such method, developed by Steiner et al. (1995),

identifies convective regions by locating areas that contain substantial reflectivities and also regions in which the reflectivity stands out from the background (i.e. the peakedness condition). Biggerstaff and Listemaa (2000) refined the Steiner algorithm to include analysis of the horizontal and vertical gradients in the radar reflectivity.

Precipitation classification algorithms using disdrometer data and Doppler profiler systems have also been developed. Atlas et al. (1999) discussed a classification algorithm based on trends in rain rate and median volume diameter (D_0) from disdrometer data. This algorithm identifies convective precipitation based on times in which the rain rate exhibits sharp increases, transition precipitation when the rain rate and D_0 are decreasing, and stratiform precipitation during periods of low rain rates. Williams et al. (1995) developed a classification algorithm using reflectivity, Doppler velocity, and the Doppler spectral width based on 915 MHz profiler data. This algorithm identifies transition, and stratiform precipitation based on the presence of a melting layer signature, and convective precipitation based on the absence of a melting layer signature and high values of reflectivity and Doppler spectral width. More complete descriptions of these algorithms will be provided in chapter 2.

Multiparameter radar data can also be used to identify convective and stratiform precipitation. Incorporating the multiparameter measurables can improve precipitation estimates as compared to estimates using only the radar reflectivity (Ryzhkov and Zrnić, 1995). This study also explores a precipitation classification algorithm using multiparameter radar that identifies convection by locating regions producing moderate/heavy precipitation.

1.2 Overview of TRMM-LBA

The Tropical Rainfall Measuring Mission-Large Scale Biosphere-Atmosphere Experiment (TRMM-LBA) conducted in Amazonia provided data from several remote sensing platforms from 10 January 1999 to 28 February 1999 (Rutledge et al., 1998). TRMM-LBA is one of several ground validation experiments conducted in conjunction with TRMM. The TRMM-LBA experiment afforded opportunities to study continental tropical precipitation systems over a remote region of the tropics, providing much needed information in terms of storm dynamics and microphysics. While previous field experiments have been conducted in this region (Amazon Boundary Layer Experiment; Garstang et al., 1994), radar observations were limited to a single X-band non-coherent radar. TRMM-LBA provided ground validation data from two Doppler radars (one polarimetric), a dual-wavelength profiler, and a dense raingauge and disdrometer network. A network of flat plate antennas and magnetic direction finding antenna were deployed to infer total lightning flash rates and locate cloud-to-ground flashes respectively. In addition to the ground-based instruments, two aircraft collected data during TRMM-LBA. The University of North Dakota Citation II collected in-situ cloud data from a cloud particle imager and a high volume precipitation spectrometer. The NASA-ER2 provided X band radar data (EDOP) and data from several radiometers carried on board.

The platforms of interest in this study are the National Center for Atmospheric Research (NCAR) S-pol radar, the Joss-Waldvogel disdrometer, the National Oceanic and Atmospheric Administration (NOAA) 915 MHz profiler, and an array of tipping-

bucket rain gauges. Data from each of these platforms provided the opportunity to investigate the performance of each precipitation classification algorithm mentioned in section 1.1. Especially noteworthy here is the multiparameter radar data from the S-pol radar, which also provided the opportunity to examine the microphysics in convection and stratiform precipitation.

1.3 Scientific Objectives and Organization of this study

This study has two scientific objectives:

1) to develop a precipitation classification algorithm using multiparameter radar data;
2) to apply existing precipitation classification algorithms to case studies from TRMM-LBA and investigate their performance;

This thesis is organized into five chapters (including this introductory chapter). Chapter 2 provides a description of each of the platforms and a description of each of the precipitation classification algorithms used in this study. The precipitation classification results from each of the algorithms from the TRMM-LBA case studies are presented in Chapter 3. These classification results are then compared in Chapter 4. Finally, Chapter 5 provides a summary of this study, conclusions, and suggestions for future research.

CHAPTER 2

Data Analysis and Methodology

This study utilizes data from the S-pol radar, Joss-Waldvogel disdrometer, 915 MHz profiler, and an array of tipping-bucket rain gauges deployed during TRMM-LBA. Section 2.1 provides a brief description of these instruments, including a layout of the platforms (See Fig. 2.1). Data obtained by these four instruments is used in a suite of precipitation classification algorithms. Section 2.2 describes these algorithms, which identify and separate convective and stratiform precipitation.

2.1 TRMM-LBA: Data and observational platforms

2.1.1 S-pol multiparameter Doppler radar data

Data for the storms investigated in this study were obtained using the linearly, dual-polarized S-pol radar operating at S band (2.7 GHz, or 11 cm). Additional specifications for the S-pol radar are shown in Table 2.1. The S-pol radar is capable of transmitting and receiving horizontally and vertically-polarized electromagnetic radiation. This polarization diversity allows the measurement of returned power in two orthogonal planes, which provides information about the size, shape, orientation, and thermodynamic

phase of the hydrometeors (Carey and Rutledge, 1998). The radar parameters used in this study include the horizontal reflectivity (Z_h), differential reflectivity (Z_{dr}), linear depolarization ratio (LDR), specific differential phase (K_{dp}), and the correlation coefficient at zero lag ($\rho_{hv}(0)$).

2.1.1.1 Reflectivity, $Z_{h,v}$

The reflectivity factor (**Z**) is a measure of the total power returned to the radar from the particles in the radar resolution volume. If the particles are spherical and small compared to the wavelength of the radar ($D < 0.07\ \lambda$), the conditions are met that satisfy the Rayleigh approximation. In this case, the reflectivity factor can be written as:

$$\mathbf{Z}=\int_0^\infty N(D)D^6 dD \quad [\mathrm{mm^6 m^{-3}}], \tag{2.1}$$

where D is the diameter of the particles, and N(D) is the number density. A dual-polarized radar measures **Z** for both horizontally and vertically-polarized electromagnetic waves. **Z** is proportional to the sixth power of the particle diameter (See equation 2.1); therefore, large particles will produce much higher reflectivity values than small particles. The values of **Z** can span several orders of magnitude and radar meteorologists commonly use a logarithmic scale to express the radar reflectivity in units of dBZ.

$$Z_{h,v} = 10\log_{10}(\mathbf{Z_{h,v}}) \ \ [\mathrm{dBZ}] \tag{2.2}$$

2.1.1.2 Differential reflectivity, Z_{dr}

The differential reflectivity (Z_{dr}) can be written as the ratio of the horizontal reflectivity factor to the vertical reflectivity factor.

$$Z_{dr} = 10\log_{10}(\mathbf{Z_h}/\mathbf{Z_v}) \text{ [dB]} \tag{2.3}$$

Z_{dr} provides a measure of particle oblateness since the calculation involves the ratio shown in equation 2.3. Due to the aerodynamic forces on a falling raindrop (D>1mm), it will exhibit the shape of an oblate spheroid, with the maximum dimension aligned in the horizontal direction (Pruppacher and Beard, 1970). Thus positive values of Z_{dr} are indicative of rain, with larger values corresponding to larger raindrops.

2.1.1.3 Linear depolarization ratio, LDR

The linear depolarization ratio (LDR) is defined as the ratio of the cross-polar signal power to the co-polar signal power:

$$LDR_{hv} = 10\log_{10}\left(\left\langle|S_{hv}|^2\right\rangle \Big/ \left\langle|S_{vv}|^2\right\rangle\right) \text{ [dB]}, \tag{2.4}$$

or

$$LDR_{vh} = 10\log_{10}\left(\left\langle|S_{hv}|^2\right\rangle \Big/ \left\langle|S_{hh}|^2\right\rangle\right) \text{ [dB]}. \tag{2.5}$$

The above equations contain elements from the backscattering covariance matrix: s_{hv}, s_{vv}, and s_{hh}. These elements refer to the transmitted and received signal power measured by the radar. The angle brackets, $\langle\ \rangle$, denote the signal due to the ensemble average of the hydrometeors in the radar volume. These variables contain two subscripts (i.e. hv, vh, vv, and hh), where the first subscript corresponds to the polarization of the received wave and the second subscript corresponds to the polarization of the transmitted wave. A comprehensive discussion on the backscattering covariance matrix can be found in Doviak and Zrnić (1993).

LDR is a measure of particle shape and canting angle of the hydrometeors in the radar volume. As discussed above (Sec. 2.1.1.2), raindrops typically fall with their maximum dimension aligned in the horizontal direction and thus exhibit a small canting angle in a mean sense, leading to low values (< -27 dB) of LDR (Doviak and Zrnić, 1993).

2.1.1.4 Specific differential phase, K_{dp}

The specific differential phase (K_{dp}) is calculated from the range derivative of the differential propagation phase (ϕ_{dp}). The radar directly measures the total differential phase (Ψ_{dp}), which is composed of two components: ϕ_{dp} and the differential backscatter phase (δ).

$$\Psi_{dp} = \phi_{dp} + \delta \tag{2.6}$$

At S-band, δ in rain is negligible (Jameson, 1985), therefore ϕ_{dp} is directly measured by the S-pol radar. The filtering of ϕ_{dp} with range is necessary to reduce the high degree of variability often observed with this variable (Hubbert and Bringi, 1995).

By using measurements of ϕ_{dp} at two ranges, a finite difference estimate of K_{dp} is calculated.

$$K_{dp} = \frac{1}{2}\frac{d\phi_{dp}}{dr} \approx \frac{\phi_{dp}(r_2) - \phi_{dp}(r_1)}{2(r_2 - r_1)} \tag{2.7}$$

K_{dp} is only affected by anisotropic hydrometeors (i.e. rain) since isotropic hydrometeors produce equal phase shifts for horizontally and vertically-polarized waves. Due to this result and the fact that K_{dp} is not affected by attenuation, rainfall estimates using K_{dp} are more accurate than estimates using only Z_h (Ryzhkov and Zrnić, 1998).

2.1.1.5 Correlation coefficient at zero lag, $\rho_{hv}(0)$

The correlation coefficient at zero lag ($\rho_{hv}(0)$) is defined as:

$$\rho_{hv}(0) = \left\langle s_{vv} s_{hh}^{*} \right\rangle \Big/ \left[\left\langle \left| s_{hh} \right|^2 \right\rangle^{1/2} \left\langle \left| s_{vv} \right|^2 \right\rangle^{1/2} \right]. \tag{2.8}$$

Equation 2.8 contains variables from the backscattering covariance matrix as shown in Doviak and Zrnić (1993). $\rho_{hv}(0)$ is the statistical correlation between the horizontal and

vertical polarized returns measured by the radar. The values of $\rho_{hv}(0)$ typically span from 0.8 to 0.99, with a uniform region of rain producing values greater than 0.97. In regions containing mixed phase hydrometeors, the value of $\rho_{hv}(0)$ tends to decrease due to the variation in canting angle, size, shape, and dielectric constant of the hydrometeors in the radar volume. This decrease makes $\rho_{hv}(0)$ a good indicator of regions in which meting processes are occurring.

2.1.1.6 Data processing

Using an automated routine, the data were edited to remove ground clutter and anomalous propagation returns. The routine utilizes thresholds on $\rho_{hv}(0)$ and the standard deviation of ϕ_{dp} ($sd(\phi_{dp})$) (Ryzhkov and Zrnić, 1998). If the value of $\rho_{hv}(0)$ is less than 0.8, or the $sd(\phi_{dp})$ is greater than 9 for given data point, all data (Z_h, Z_{dr}, LDR, K_{dp}, and $\rho_{hv}(0)$) are flagged as bad data and not used for analysis. Following the editing process, the data are interpolated to a Cartesian grid using the NCAR REORDER software and a Cressman filter with a fixed radius of influence (0.9) for all dimensions (Cressman, 1959).

2.1.2 Joss-Waldvogel disdrometer

This study uses data from the Joss-Waldvogel disdrometer (Joss and Waldvogel, 1967) to classify precipitation as convective, transition, or stratiform. The disdrometer was located at the Ji Parana Airport (latitude: -10.875°, longitude: -61.851°). The

instrument recorded the number of raindrops in twenty size intervals, ranging from 0.35 mm to 5.37 mm, with one-minute resolution. The data were processed following the methods of Keenan et al. (2000), assuming a gamma distribution of the form (Ulbrich, 1983):

$$N(D) = N_0 D^{\mu} e^{(-\Lambda D)} \ (\mathrm{m^{-3}\,cm^{-1}}). \tag{2.9}$$

The following raindrop size distribution (DSD) parameters are obtained from the processed data: number density (N_0) (m^{-3} $cm^{-1-\mu}$), median volume diameter (D_0) (cm), slope (Λ) (cm^{-1}), and shape factor (μ) (dimensionless). D_0 and the rain rate recorded by the disdrometer are necessary in order to apply the disdrometer-based classification algorithm (discussed in section 2.2). The rain rate is calculated using the following equation (Doviak and Zrnić, 1993):

$$R = (0.6 * \pi * 10^{-3}) \int_{D_{\min}}^{D_{\max}} D^3 N(D) \upsilon(D) dD \ (\mathrm{mm\ h^{-1}}), \tag{2.10}$$

where v(D) is the terminal velocity of the raindrops given by (Atlas and Ulbrich, 1977):

$$\upsilon(D) = 3.778 * D^{0.67} \ (\mathrm{m\ s^{-1}}). \tag{2.11}$$

The integral (equation 2.2) is solved numerically, yielding the rain rate from the disdrometer data. To validate these estimates, the rain rates are compared to the co-

located rain gauge (see Fig. 2.2). The results show that the disdrometer is slightly underestimating rain rates compared to the rain gauge. During periods of heavy rain, the disdrometer requires a recovery time between raindrop impacts. During this recovery time, the disdrometer does not record data, which can possibly lead to an under-estimation of rainfall. Another possible source of error can be caused by water accumulation on the impact sensor, leading to a calibration error (Nystuen, 1999). However, there is reasonable agreement between the gamma-distribution rain rates (computed by the above methods) and the rain gauge rain rates, indicating that the gamma DSD fits are accurate.

2.1.3 NOAA 915 MHz Profiler

The 915 MHz (33-cm wavelength) profiler provided measurements of back-scattered power, Doppler velocity, and spectral width. This instrument uses three fixed-position beams, one pointed vertically and two pointed 21° off zenith in orthogonal planes. The profiler has three modes of operation: low-height mode, high-height mode, and Radio Acoustic Sounding System (RASS) mode. Only data collected in the high-height mode are used in this study. This data provided a one-minute resolution and sampled the atmosphere with a 250-meter pulse length to a height of 18 km. The profiler was located at the Ji Parana Airport (latitude: -10.875°, longitude: -61.851°). A detailed discussion of the 915 MHZ profiler data processing and operational characteristics can be found in Williams et al. (1995).

2.1.4 TRMM-LBA rain gauge networks

Rain rate (R) data from rain gauge network #1 (latitude: -10.89°, longitude: -61.86°) and network #2 (latitude: -10.79°, longitude: -62.2°) are used in this study. Each of these rain gauge networks contained 13 tipping bucket rain gauges, which provided one-minute resolution rain rates for each case investigated. Sources of error for this instrument include spillage of water between tips in heavy rainfall and reduction in catchment due to wind (Nystuen, 1999). While the rain rates from the gauges are not used in the classification algorithms, the data are used in comparisons with the radar and disdrometer-inferred rain estimates. Instantaneous rain rates are also used to measure the performance of the classification algorithms at various times and locations.

2.2 Precipitation classification algorithms

2.2.1 Disdrometer-based classification

The work of Atlas et al. (1999, henceforth A99) describes a method of classifying convection, transition, and stratiform precipitation based on the temporal trends in R, and D_0. These variables are obtained from the processed Joss-Waldvogel disdrometer data. Per A99, if R rises sharply to a peak in excess of 10-15 mm h^{-1} and D_0 does not vary greatly, the precipitation is classified as convective. If R and D_0 are decreasing following a convective period, the precipitation is classified as transition. Lastly, if R falls below

10 mm h^{-1} while D_0 remains constant or is increasing, the precipitation is classified as stratiform.

2.2.2 Profiler-based classification

Williams et al. (1995, henceforth W95) developed an algorithm to classify precipitation using a 915 MHz profiler. This algorithm uses the presence or absence of three criteria to classify precipitation: a melting layer signature, enhanced turbulence above the melting layer (0° C isotherm), and hydrometeors above the melting layer. The separation of deep and shallow convection is based on the last criterion mentioned above. However, this separation is not used in this study. The W95 study utilized 30-minute averaged profiles, while this study uses instantaneous profiles correlated in time with the radar and disdrometer observations.

In order to determine the presence of a melting layer signature, the maximum gradient in the Doppler velocity (DVG) is calculated between the heights of 3.5 and 5 km. DVG values exceeding 2.0 m s^{-1} km^{-1} indicate the presence of a melting layer signature. In the absence of this melting layer signature, the precipitation is classified as convective.

Given the presence of a melting layer signature, the algorithm produces a mixed convective/stratiform (transition) or stratiform classification. These two categories are separated based on the amount of turbulence above the melting layer. If the maximum spectral width (MSW) exceeds 2.5 m s^{-1} in a cloud well above the melting layer (7 km AGL), the precipitation is classified as transition, otherwise it is classified as stratiform.

The application of this algorithm to the data set initially failed to classify cases of obvious convection. These misclassifications were due to the presence of high DVG values in several cases that exhibited high reflectivity (>40 dBZ) and spectral width (> 4 m s^{-1}) values. The algorithm was refined to include a test on the maximum reflectivity (MZ) below the 0° C isotherm, and a threshold on the MSW above 7 km AGL. If the MZ exceeded 40 dBZ and/or the MSW exceeded 4 m s^{-1}, the profile was classified as convective, regardless of the DVG criteria.

2.2.3 Reflectivity-based classification

The reflectivity (or peakedness) algorithm developed by Steiner et al. (1995, henceforth S95) is used operationally in the TRMM ground-validation program to classify precipitation from ground-based radar. The algorithm is also one of two steps (TRMM 2A23) used in classifying precipitation from the precipitation radar (PR) on the TRMM satellite. The first step in the algorithm is the identification of regions exhibiting high values of reflectivity. If the reflectivity in a grid point in the radar volume exceeds 40 dBZ, the point is classified as convective.

The second step is to identify grid points that exceed the average intensity over the surrounding background area (peakedness). The background reflectivity (Z_{bg}) is calculated by finding the average reflectivity within an 11 km radius surrounding a given grid point. The reflectivity difference (ΔZ) is then calculated based on Z_{bg} as follows:

$$\Delta Z = \begin{cases} 10, & Z_{bg} < 0 \\ 10\text{-}(Z^2_{bg}/180), & 0 \le Z_{bg} < 42.43 \\ 0, & Z_{bg} \ge 42.43. \end{cases} \quad (2.12)$$

If Z_h of a grid point minus Z_{bg} is greater than ΔZ, then the grid point is classified as convective.

The last step in the algorithm is to calculate a convective radius (CR) around all points classified as convective. This calculation is based on the magnitude of Z_{bg} and is as follows:

$$CR = \begin{cases} 1 \text{ km}, & Z_{bg} \le 25 \text{ dBZ} \\ 2 \text{ km}, & 25 < Z_{bg} \le 30 \text{ dBZ} \\ 3 \text{ km}, & 30 < Z_{bg} \le 35 \text{ dBZ} \\ 4 \text{ km}, & 35 < Z_{bg} \le 40 \text{ dBZ} \\ 5 \text{ km}, & Z_{bg} > 40 \text{ dBZ} \end{cases} \quad (2.13)$$

These CR values are based on the "medium" size convective radii (see S95, Fig. 6). In this analysis, the algorithm is applied to the Cartesian radar data on a 2-km horizontal grid resolution.

2.2.4 Improved reflectivity-based classification

The next classification algorithm presented here was developed by Biggerstaff and Listemaa (2000, henceforth BL00). The initial step in the algorithm is based on the S95 algorithm. The S95 results are then investigated for possible re-classification.

The horizontal ($|\nabla_H Z_h|$) and vertical ($\nabla_z Z_h$) gradients are calculated at each grid point in the radar volume. The $\nabla_z Z_h$ is calculated by first determining the level of maximum Z_h. $\nabla_z Z_h$ is then calculated in a layer 3 km above this level. If the value of $\nabla_z Z_h$ is greater than 3.5 dB km^{-1}, the grid point is classified as stratiform. This is based on the fact that in stratiform precipitation, a bright band in Z_h is usually present. Given the presence of a bright band, the vertical gradient in Z_h will positively (negatively) increase sharply below (above) the melting layer.

Next, the $|\nabla_H Z_h|$ is calculated around a given convective grid point. In convection, Z_h typically falls off rapidly away from the core, while stratiform precipitation usually produces a homogeneous reflectivity field. If the value of $|\nabla_H Z_h|$ is less than 3.0 dB km^{-1}, the grid point is re-classified as stratiform. For this analysis, the algorithm is applied to the Cartesian radar data on a 2-km horizontal grid resolution.

2.2.5 *Multiparameter-based classification algorithm*

Multiparameter radar can accurately estimate precipitation and offers advantages over estimates that only include reflectivity measurements (Ryzhkov and Zrnić, 1998; Gorgucci et al., 1997). For example, incorporating the differential reflectivity (Z_{dr}) and

specific differential phase (K_{dp}) can improve precipitation estimates as compared to a standard *Z-R* estimator (Ryzhkov and Zrnić, 1995). Also, including a set of multiparameter rain estimators can more accurately identify regions of moderate/heavy rain, leading to the identification of the convective region of a storm.

The first step in the multiparameter classification algorithm (henceforth MP) requires the development of a set of accurate polarimetric rain-estimating algorithms. The probability matching method as described by Gorgucci et al. (1997) was applied to the February 15, 1999 case study. This method assumes that the rain rate at the ground is related to the reflectivity (or some combination of polarimetric variables) at 0.5 km above ground level (AGL). The effects of advection and evaporation of the raindrops are neglected in this study. However, the radar-based rain rate estimates were compared to the rain gauge rain rates using a 3-minute lag to account for the fall-time of the raindrops from 0.5 km AGL to the ground. The correct relationship of Z to R defines an exact match of the probability density functions as follows:

$$p(R_i)dR = p(Z_i)dZ\,. \tag{2.14}$$

The pairs of (R_I,Z_I) define the relationship between Z and R. The PMM is as follows:

1) Obtain the radar variables Z_h, Z_{dr}, and K_{dp} at grid points 0.5 km (AGL) that correspond to the location of a surface rain gauge.

2) Using rain-estimating algorithms of the form:

$$R = a(Z_h)^b\,, \tag{2.15}$$

$$R = a(K_{dp})^b\,, \tag{2.16}$$

$$R = a\left(K_{dp}\right)^{b} * \left(Z_{dr}\right)^{c}, \tag{2.17}$$

$$R = a\left(Z_{h}\right)^{b} * 10^{-c*Z_{dr}}, \tag{2.18}$$

develop a cumulative frequency diagram (CFD) of rain rates based on the radar measurable.

3) Develop a cumulative frequency diagram of rain rates recorded by the rain gauge at each point for each time in the radar volume.

4) Minimize the summed square error (SSE) between the CFDs by iterating *a* and *b* (and *c* if applicable) in equations (2.15) to (2.18).

The PMM-derived estimators (see Table 2.2) have been compared to a set of rain-estimating equations derived as a function of drop shape and diameter relationships (T-matrix method). (See Appendix A for a complete description of the T-matrix method.) The comparisons (see Table 2.3) indicate that the PMM estimators better represent total rain accumulation than do the T-matrix estimators for the February 15 case study. The ability of the PMM and the T-matrix estimators to estimate instantaneous rain rates was also investigated for a variety of times and storms. In each case, the PMM estimators proved to be the best rain estimators for this data set.

The next step is to define a rain rate that is associated with convective rain. Selecting a rain rate indicative of convection, however, is not straightforward. Tokay et al. (1996) developed a partitioning algorithm based on a threshold between the DSD parameter N_0 and rain rate using Joss-Waldvogel disdrometer data. This threshold is shown in the following equation:

$$N_0 = 4x10^9 * R^{-4.3} \tag{2.19}$$

For a given rain rate, the value for the right hand side of equation (2.19) is first calculated. If the measured value of N_0 exceeds this value, the precipitation is classified as convective, otherwise it is classified as stratiform. For example, if the disdrometer measures a rain rate of 10 mm h^{-1}, and N_0 is greater than 2.00474 x 10^5, the precipitation is classified as convective. For N_0 less than or equal to the above value, the precipitation is classified as stratiform. Using this algorithm (N_0/R threshold), Tokay et al. (1999) reported that almost all cases of rain rates greater than 10 mm/hr are convective.

To investigate the validity of this convective rain rate threshold (i.e. 10 mm h^{-1}), convective and stratiform classification results from W95 and the S95 algorithms were compared to the averaged rain rates recorded by nearby rain gauges. The rain rates were separated based on the results of the above partitioning algorithms (W95 and S95), and a cumulative frequency diagram has been constructed for each precipitation category (see Fig. 2.3)

The results show that 34% of the rain rates are below 10 mm/hr in convection based on W95, while this value is 41% based on S95. These results also show that 95% of the rain rates are below 10 mm/hr in stratiform precipitation based on W95, with a value of 92% based on S95. These results indicate that the rain rate describing convection is perhaps slightly less than 10 mm/hr. However, the results do not account for possible classification error in each of the algorithms, but do show that the demarcation between convective and stratiform rain rates is variable.

Given this variability, a rain rate of 10 mm h^{-1} was chosen as a "starting point" to identify convective grid points. If the calculated rain rate in a given grid point exceeded 10 mm h^{-1}, the point was considered convective. However, due to the variability previously described, the remaining grid points were subjected to further analysis.

This analysis involved calculating the trend in the rain rate for all grid points in the radar volume being investigated. The trend in rain rate is calculated by investigating the preceding radar volume and the radar volume following the time of interest. This is typically a five to ten-minute window surrounding the time being investigated. The highest available temporal resolution of the radar data was used in this study to ensure an accurate calculation of the trend in rain rate. If the rain rate exceeds 5 mm/hr and is increasing significantly (by a factor of 60%), the grid point is classified as convective.

For this test to classify the grid point as convective, the rain rate would have to increase from a value greater than 5 mm h^{-1} to a value exceeding 8 mm h^{-1}. The variability of rain rate exists in all types of precipitation, however this type of increase is commonly observed in convection (A99; Tokay et al., 1995; Tokay et al., 1999). In this analysis, the algorithm is applied to the Cartesian radar data with a 1-km horizontal resolution.

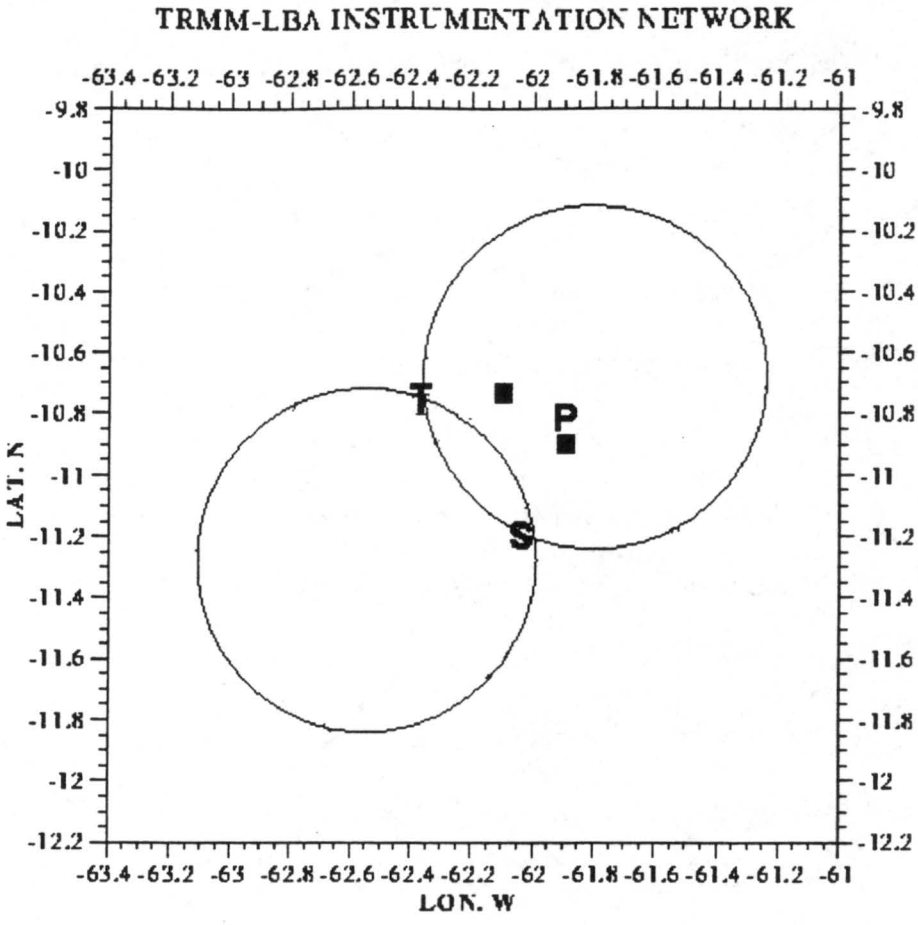

Figure 2.1. Instrumentation plan showing location of the SPOL radar (**S**), 915 MHz profiler and Joss-Waldvogel disdrometer (**P**), and rain gauge network #1 and 2 (■). *Source: CSU Radar Meteorology (http://radarmet.atmos.colostate.edu/lba_trmm/map2.gif)*

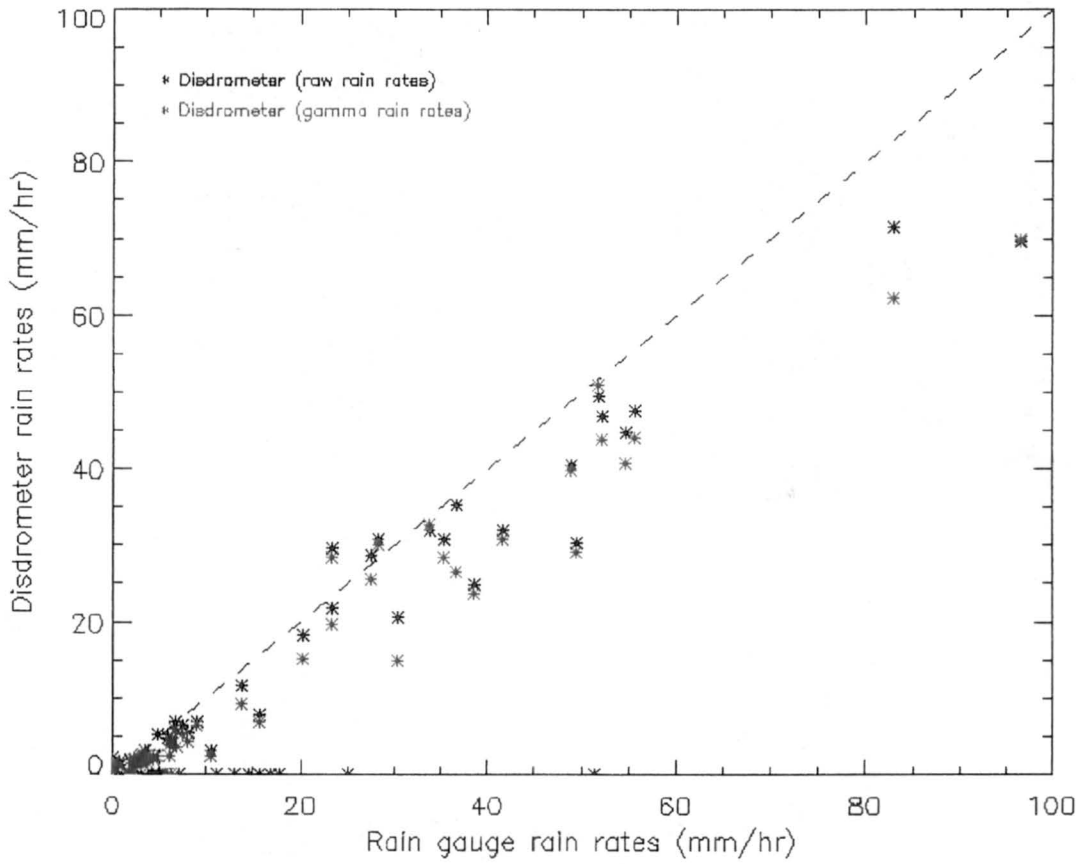

Figure 2.2. Disdrometer rain rates (raw and gamma distribution) versus rain gauge rain rates for January 23, February 15, 17, and 27 case studies.

a)

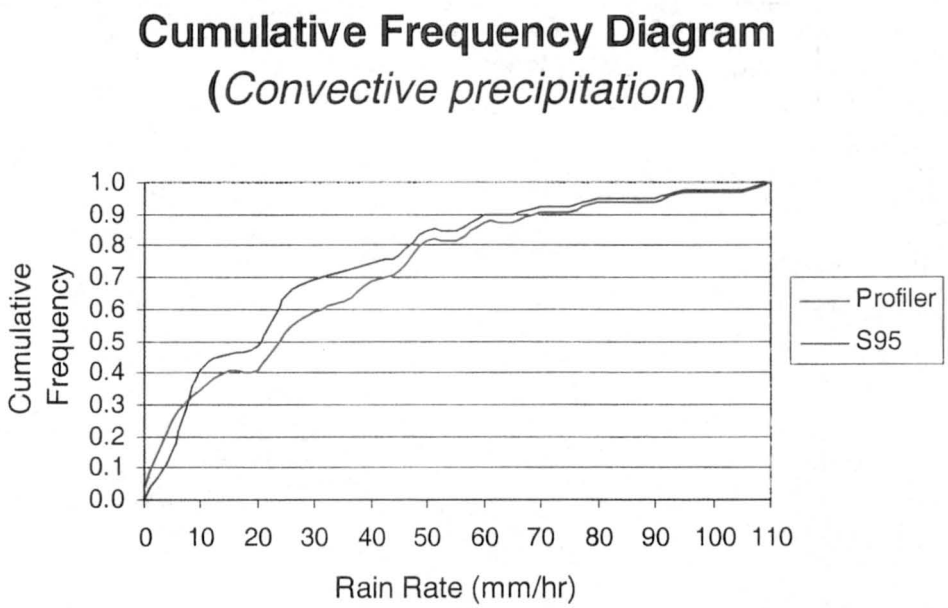

b)

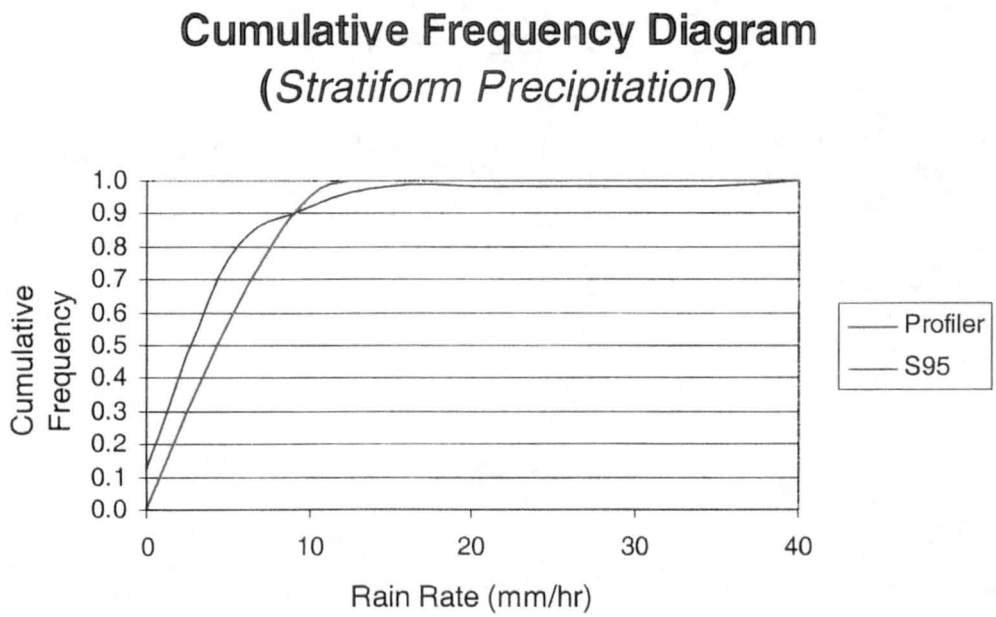

Figure 2.3. Cumulative frequency diagrams of convective (a) and stratiform (b) rain rates, based on the W95 and S95 classification algorithms.

Transmitter	2.7 -- 2.9 GHz
Pulse Width	.3 -- 1.4 μsec-tapered
PRF	0 -- 1300 Hz
Peak power	>1Mw
Receivers (2)	H & V simultaneously
Noise power	-115.5 dBm
Radar Noise figure	2.9 dB
Dynamic range	90 dB
Bandwidth	.738 MHz
Digital IF	Linear floating point processing
I-Q image rejection	50 dB
Minimum detectable dBZ at 50km/1km	-15 dBZ/-52 dBZ at -6 dB SNR
Polarization switching	H-V alternating or H only
Gain	44.5 dB including wave guide loss
Antenna	Parabolic, center feed
Diameter	8.5 m (28 ft.)
Beamwidth	0.91 degrees
First sidelobe	better than -30 dB
Scan rate	Up to 18°/s each axis, 30°/s with pulley change
Wind limit for operation	30 m/s / 60 m/s (no radome)
Number of range gates 4000	Gate spacing 37.5 -- 1000m
Times series (I/Q) capability Yes	Real time scientific display NCAR Zebra
Recorded variables	PhiDP, PhoHV, NCP, ZH, ZDR, LDR, Kdp, PHH, PVV, V, W, R(1)HV, R(1)VH|, |R(2)|

Table 2.1. Operating and technical specifications of the NCAR S-pol radar.

	$R = aZ^b$		$R = a(K_{dp})^b$		$R = a(K_{dp})^b * (Z_{dr})^c$			$R = a(Z_h)^b * 10^{-cZdr}$		
Estimator	a	b	a	b	a	b	c	a	b	c
T-matrix	0.031	0.68	59.0	0.77	60.4	0.82	-0.23	0.003543	0.727	-0.376
PMM	0.02	0.745	45.9	0.89	64.09	0.95	-0.109	0.015	0.8	-0.101

Table 2.2. Radar rain rate equations using T- matrix and PMM estimators.

Rain-estimator	*PMM (mm)*	*T-Matrix(mm)*
Z-R	*389*	*332*
$R(K_{dp})$	*336*	*495*
$R(Z/Z_{dr})$	*385*	*299*
$R(K_{dp}/Z_{dr})$	*349*	*299*
Gauges	*400*	

Table 2.3. Total rain accumulation as measured by rain gauges and radar rain estimators for February 15, 1999 case study.

Chapter 3

Classification results from TRMM-LBA case studies

This study analyzes six TRMM-LBA case studies, which are each briefly described in Section 3.1. The MP and S95 classification algorithms are applied to all cases, while the A99 and W95 classification algorithms are applied to four cases: January 23, February 15, February 17, and February 27. The disdrometer and co-located rain gauge (gauge #27) recorded precipitation for only 10 minutes during the January 26 case. Due to the short time scale of this precipitation event, the A99 and W95 algorithms were not applied to this case. The A99 and W95 algorithms were not applied to the February 23 case, as this event occurred well to the north (40 to 70 km) of the disdrometer and profiler.

The BL00 classification algorithm is applied to two cases (January 26 and February 23). This algorithm relies on the vertical gradient of reflectivity in order to classify precipitation. Therefore, the radar data must provide good vertical coverage of the storm. The January 26 and February 23 cases satisfy these requirements. However, the BL00 algorithm was not applied to the remaining cases, as the radar coverage did not satisfy these requirements.

3.1 Overview of case studies

3.1.1 January 23, 1999

This storm exhibited strong convection with storm motion in the easterly phase (i.e., propagating from the east). The storm passed within 60 km to the north of the S-pol radar. The period of analysis runs from 2130 to 2230 UTC (all times denoted are UTC). A time-series of images showing the evolution captured by the S-pol radar is presented in Fig. 3.1. Early in the analysis period (2130), the storm exhibited a strong leading convective region, with reflectivity (Z_h) values exceeding 50 dBZ. By 2220, several individual cells had developed and had begun to decay around 2230. This case study will be used to demonstrate the MP, A99, W95, and S95 classification algorithms (shown later). The storm (individual convective cells) began to weaken after 2230 (not shown).

3.1.2 January 26, 1999

This storm exhibited squall line characteristics with multi-cellular convection throughout the period of analysis. Again, storm motion was from the east. The period of analysis runs from 2100 to 2350. Images from the S-pol radar showing storm evolution are presented in Fig. 3.2. The line passed directly over the S-pol radar, which compromised horizontal coverage of the storm for a short period (2150 to 2210). This case study will be used to demonstrate the MP, S95, and BL00 classification algorithms.

3.1.3 February 15, 1999

During this case, the S-pol radar captured the passage of several convective lines. Again, storm motion was from the east. The period of analysis runs from 0340 to 0700. Images from the S-pol radar showing storm evolution are presented in Fig. 3.3. The scanning strategy for this case focused on capturing the storm as it passed over the rain gauge networks. The scans provided a one-minute resolution data set for radar/rain gauge comparisons. These comparisons led to the development of a set of polarimetric rain-estimating algorithms, using the PMM (as discussed in the previous chapter). This case study will be used to demonstrate the MP, A99, W95, and S95 classification algorithms.

3.1.4 February 17, 1999

This storm exhibited strong convection building to the northeast of the S-pol radar around 1700. Also at this time, several convective cells well to the north of the S-pol radar had begun to decay. Images from the S-pol radar showing storm evolution are presented in Fig. 3.4. The period of analysis runs from 1700 to 1800. Again, storm motion was from the east, and by 1730, a fairly strong squall line had developed. This squall line passed over rain gauge network #1 and produced rain rates greater than 100 mm h^{-1}. Near the end of the analysis, several new convective cells had developed to the north and northeast of the S-pol radar. This case study will be used to demonstrate the MP, A99, W95, and S95 classification algorithms.

3.1.5 February 23, 1999

This storm exhibited organized convection 100 km north of the S-pol radar. The period of analysis runs from 2100 to 2200. The storm motion was in the westerly (monsoonal) phase (Rutledge et al., 2000). Radar images showing storm evolution are presented in Fig. 3.5. The precipitation radar (PR) on the TRMM satellite captured this storm early in the period of analysis (2100). This case demonstrates the MP, S95, and BL00 classification results. The classification results from the ground-based algorithms are also compared to the satellite-based, precipitation classification algorithm (TRMM 2A23) near 2100 UTC.

3.1.6 February 27, 1999

This storm exhibited weak convection embedded within predominantly stratiform precipitation. The period of analysis runs from 1000 to 1200. The storm motion was in the westerly phase, and images showing storm evolution are presented in Fig. 3.6. Early in the period, the S-pol radar data indicated a region of 40-dBZ reflectivity, which decayed shortly thereafter. This case demonstrates the MP, A99, W96, and S95 classification algorithms.

3.2 Disdrometer-based classification results

The A99 classification algorithm was applied to the January 23, February 15, 17, and 27 case studies. Fig. 3.7 shows the classification results, the rain rate recorded by the disdrometer and the co-located raingauge #27 (G27), and the median volume diameter (D_0) recorded by the disdrometer for each case. These results are compared to the co-located 915 MHz profiler images (see Fig. 3.8), which show the vertical structure of each storm as it passed over the disdrometer, providing qualitative validation of each algorithm's performance.

3.2.1 January 23, 1999

Early in this case, the rain rate recorded by the disdrometer was 40 mm h^{-1}, and D_0 exceeded 2 mm (see Fig. 3.7a). The high rain rates and large values of D_0 indicate convection over the disdrometer. The profiler data (see Fig. 3.8a) showed values of reflectivity exceeding 40 dBZ and large values of spectral width (4-5 m s^{-1}), indicating the presence of hydrometeors and broad Doppler spectra. Both quantities are consistent with the presence of convection (S95; Cifelli and Rutledge, 1998). The A99 algorithm classified the first twenty minutes of the case as convective (2130 to 2150). By 2150, the rain rate and D_0 had decreased to 10 mm h^{-1} and 0.5 mm respectively. The algorithm produced a stratiform classification at this time and for the remainder of the case.

3.2.2 February 15, 1999

During this case, several convective events passed over the disdrometer. The classification results are shown in Fig. 3.7b. The algorithm classified the first hour of the case as stratiform (0340 to 0440). However, the profiler image indicates that a brief period of convection occurred at 0400 (see Fig. 3.8b). The reflectivity at this time exceeded 40 dBZ, and the spectral width exceeded 4 m s^{-1}. Based on this information, it seems likely that the algorithm misclassified this early convective event. The disdrometer recorded rain rates less than 10 mm h^{-1}, thus producing the stratiform classification. Otherwise, the algorithm succesfully classified the remaining three convective events.

3.2.3 February 17, 1999

Fig. 3.7c shows that the algorithm captured this isolated convective event successfully. The A99 algorithm produced a convective classification from 1705 to 1730, a brief transition period at 1730, and the remainder of the case is unclassified. The rain rates for this case reached 70 mm h^{-1}, and the trend in D_0 was highly correlated with the rain rate, with values reaching 2.5 mm. The classification results are confirmed by inspection of the profiler image (see Fig. 3.8c), which shows an isolated convective event from 1700 to 1730. The period from 1735 to 1800 was unclassified since the disdrometer was not recording precipitation during these times.

3.2.4 February 27, 1999

The A99 algorithm classified this case as stratiform for the entire period (see Fig. 3.7d) from 1025 to 1200. The case was not classified prior to this period (1000 to 1025) since the disdrometer was not recording precipitation. The profiler image (see Fig. 3.8d) indicates a well-defined radar bright band for the entire period, confirming the classification results as stratiform.

3.3 Profiler-based classification results

The W95 classification algorithm was applied to the January 23, February 15, 17, and 27 case studies. Fig. 3.9 shows the classification results, the maximum vertical velocity gradient (MVG, m s^{-1} km^{-1}), the maximum spectral width (MSW, m s^{-1}) above 7 km, and the maximum reflectivity (MZ, dBZ) below 3.5 km. As discussed in Sect. 3.2, the 915 MHz profiler images (Fig. 3.8) show the vertical structure of each storm. These images, along with the S-pol radar images (Fig. 3.1 to 3.6) will be used here in order to provide a qualitative assessment of the W95 algorithm performance.

3.3.1 January 23, 1999

Fig. 3.9a shows the classification results for the January 23 case. The W95 algorithm produced a convective classification from 2130 to 2215. The results are consistent with the profiler images (see Fig. 3.8a), which show high values of

reflectivity and spectral width during the times that the algorithm indicated convection. The MSW (see Fig. 3.8a) peaked at a value of ~13 m s^{-1} and remained above 4 m s^{-1} until 2215, which indicates turbulent motions likely associated with convection (S95; Cifelli and Rutledge, 1998). The S-pol radar images (Fig. 3.1a-c) indicate cellular structure with reflectivity values exceeding 40 dBZ over the profiler (x =16 km E.; y = 38 km N.) from 2130 to 2150. However, at 2200, the reflectivity values shown in the radar image (Fig 3.1d) fall off to below 30 dBZ and no longer indicate cellular structure over the profiler. The radar image at this time (2200) tends to indicate that the precipitation should have been classified as transition, yet the MSW values were still above 4 m s^{-1}, and the W95 algorithm maintained a convective classification.

The remainder of the period was classified as transition starting at 2115, consistent with a period of low reflectivity values starting around this time (Fig. 3.8a). By 2220, the S-pol radar image (Fig. 3.1f) also indicated low reflectivity values (< 20 dBZ) over the profiler. The rain rates from G27 fell below 1 mm h^{-1} after 2220. Low precipitation rates are expected in the transition zone as particle evaporation and advection are occurring in this region (Houze, 1993). Therefore, the low precipitation rates recorded by rain gauge #27 combined with the qualitative radar data observations suggest that the transition classification is correct.

3.3.2 February 15, 1999

The algorithm captured four convective events for this case (Fig. 3.9b). In each case, the convective classification corresponds to a peak in MZ and MSW. The profiler image

(Fig. 3.8b) shows three distinct times in which the reflectivity was greater than 40 dBZ and the spectral width exceeded 4 m s^{-1}, likely indicators of convection (S95; Cifelli and Rutledge, 1998). These times are correlated with those that the algorithm indicated were convective (0350-0400; 0435-0455; 0540-0550). The S-pol radar images (Fig. 3.3b, 3.3d, and 3.3e) also show cellular structure over the profiler (x =16 km E.; y = 38 km N.) during each of these periods.

The final convective event as indicated by the W95 algorithm occurred from 0620 to 0640. Fig. 3.8b does not show this event, however G27 recorded rain rates between 20 and 50 mm h^{-1} during this time. Furthermore, the radar images (Fig. 3.3g-h) also show high values of reflectivity (> 45 dBZ) and cellular structure over the profiler during this period.

The W95 algorithm produced a stratiform classification from 0400 to 0435, 0500 to 0525, 0610 to 0620, and at 0700. During each of these periods, the profiler image indicates the presence of a bright band in the reflectivity (Fig. 3.8b). The S-pol radar images also show weak reflectivity values over the profiler during these periods. The use of vertical cross sections from the radar data was not possible for this case, as the radar scans did not provide sufficient vertical resolution. The rain rates at G27 were 10 mm h^{-1} and decreasing at 0400 and remained below 5 mm h^{-1} until 0433. At 0500, the G27 rain rate was 14 mm h^{-1} and decreased to 4 mm h^{-1} by 0505 and remained below 5 mm h^{-1} until 0530. During the final two periods classified as stratiform by the W95 algorithm, the G27 rain rates were below 3 mm h^{-1}. In each case, the stratiform classification appears to be correct.

3.3.3 February 17, 1999

Fig. 3.9c shows that the MZ and MSW reached very high values for this case. As previously mentioned, this case was a very strong convective event. The W95 algorithm produced a convective classification from 1705 to 1750, and a transition period from 1750 to 1800. The profiler image (see Fig. 3.8c) shows reflectivity values in excess of 40 dBZ and spectral width values greater than 4 m s^{-1} for most of the case. The S-pol radar images indicate cellular structure over the profiler (x =16 km E.; y = 38 km N.) until 1750, at which time the convective line was to the west of the profiler (Fig. 3.4f, x = 10 km; y = 25 km).

3.3.4 February 27, 1999

The results for this case are shown in Fig. 3.9d. The algorithm classified this case as stratiform from 1005 to 1200. The profiler image (Fig. 3.8d) shows a well-defined bright band in the reflectivity for the entire case, which is consistent with these results. The MSW for this case remained below 2.5 m s^{-1}, and the MVG exceeded 2 m s^{-1} km^{-1} for the entire case. The S-pol radar images show low values of reflectivity over the profiler (x =16 km E.; y = 38 km N.) throughout the period. The mean rain rate at G27 was slightly below 5 mm h^{-1}, with a brief period (1056 to 1059) in which the rain rates were above 10 mm h^{-1}. Again, the radar and rain gauge data are consistent with the W95 stratiform classification.

3.4 Reflectivity-based classification results

The S95 classification algorithm was applied to all of the case studies. Fig. 3.10 to 3.15 show a solid contour that indicates the convective region as classified by the algorithm. In addition to the qualitative results, the total convective area, total area producing precipitation (henceforth, denoted as "total area"), and convective fraction from each case are presented in this section.

The convective fraction was measured by first calculating the total area of each radar scan that exceeds 20 dBZ at 1 km AGL. Using the Z-R relationship found via the PMM (discussed in Chapter 2), a value of 20 dBZ corresponds to a rain rate of approximately 1 mm h^{-1}. Therefore, the value of 20 dBZ was chosen to represent the total area within each scan producing precipitation. Once the total area was calculated, the convective area was divided by the total area, yielding the convective fraction. The total convective area and convective fraction from each case are shown in Table 3.1. The values shown in the table are representative of the areas calculated at a height of 1 km AGL for this and all algorithms discussed in this chapter.

3.4.1 January 23, 1999

Fig. 3.10 shows that the S95 algorithm successfully identified the cellular structure in the radar images. Especially noteworthy is the performance at 2230 (see Fig. 3.10g), in which the algorithm successfully identified seven isolated convective regions. The total area classified as convective was 11196 km^2, and the convective fraction was 62%.

3.4.2 January 26, 1999

From 2100 to 2300, the S95 algorithm successfully identified regions of high reflectivity that exhibited cellular structure (see Fig. 3.11a-e). However, the results at 2330 and 2350 (Fig. 3.11f-g) indicate that the algorithm identified convection in regions of relatively uniform reflectivity. These regions have likely been misclassified, as the vertical cross section (see Fig. 3.16) at 2350 shows a bright band in the reflectivity, indicative of stratiform precipitation. The total area classified as convective was 15464 km^2, and the convective fraction was 36%.

3.4.3 February 15, 1999

The S95 algorithm successfully identified the cellular structure from 0340 to 0500 (see Fig. 3.12a-d). However, at 0530, 0600, and 0630 (Fig. 3.12e-g) several regions were identified as convective that exhibited relatively uniform reflectivity values. The rain gauges in the vicinity were recording rain rates between 5 and 10 mm h^{-1}. Vertical cross sections from the S-pol radar data could not be investigated since the radar data did not provide sufficient vertical resolution. It is therefore difficult to conclude that these regions have been misclassified since the vertical structure could not be investigated. The total area classified as convective was 68836 km^2, and the convective fraction was 34%.

3.4.4 February 17, 1999

Fig. 3.13 shows that the algorithm was successful in classifying the isolated convective cells for this case. At each time shown, the algorithm captured the cellular structure. The total area classified as convective was 13666 km^2, and the convective fraction was 70%.

3.4.5 February 23, 1999

Fig. 3.14 shows the classification results for this case. The algorithm performed well for most of this case (2100 to 2130), but did identify several small regions in the later periods as convective that did not exhibit cellular structure. These regions, which may be misclassified, are, however, small and isolated. The total area classified as convective was 3632 km^2, and the convective fraction was 25%.

3.4.6 February 27, 1999

Fig. 3.15 shows the classification results for this case. In the early period of the analysis (1000 to 1030), the algorithm identified several small regions of isolated convection. The rain gauges recorded rain rates between 5 and 15 mm h^{-1} at 1000, indicating that moderate rainfall was occurring in the region, but the radar image shows a relatively uniform reflectivity field, with the exception of a small region exceeding 40

dBZ (x = -4 km; y = 40 km). The total area classified as convective was 5636 km^2, and the convective fraction was 14%.

3.5 Improved reflectivity-based classification results

The BL00 classification algorithm was applied to the January 26 and February 23 case studies. Fig. 3.17 and 3.18 show a solid contour that indicates the convective region as classified by the algorithm. The total convective area, total area, and convective fraction from each case are presented in Table 3.1.

3.5.1 January 26, 1999

Fig. 3.17 shows that the algorithm performed well on this case until 2330. At 2330 and 2350 (Fig. 3.17f and 3.17g) the algorithm identified a few small regions of relatively uniform reflectivity as convective. As mentioned above, a vertical cross section (see Fig. 3.16) at 2350 shows a bright band in the reflectivity, indicative of stratiform precipitation. The total area classified as convective was 11408 km^2, and the convective fraction was 26%.

3.5.2 February 23, 1999

Fig. 3.18 shows the classification results for this case. The algorithm captured the cellular structure for most of this case. However, several small regions were identified as

convective late in this case that exhibited weak, uniform reflectivity in the radar image. The total area classified as convective was 3452 km^2, and the convective fraction was 24%.

3.6 Multiparameter-based classification results

The MP classification algorithm was applied to all of the case studies. Fig. 3.19 to 3.24 show a solid contour that indicates the convective region as classified by the algorithm. The total convective area, total area, and convective fraction for all of the cases are shown in Table 3.1.

3.6.1 January 23, 1999

The MP algorithm was successful in isolating the cellular structure shown in the radar images (see Fig. 3.19). However, at 2230, the algorithm may have misclassified several small regions as convective. These regions lay outside the convective cores in areas of weak reflectivity (20-25 dBZ), but the K_{dp} rain estimator indicated rain rates greater than 10 mm h^{-1}. These regions were therefore classified as convective. The total area classified as convective was 9992 km^2, and the convective fraction was 55%.

3.6.2 January 26, 1999

Again, the algorithm identified the cellular structure well for this case, especially in the early period of analysis (see Fig. 3.20). It did, however, classify a region of somewhat uniform reflectivity as convective at 2350 (see Fig. 3.20g, x= -20 to 0; y= -50 to 0). This region appeared to be trailing stratiform precipitation, in which case the convective classification would be in error. Also, a bright band in the reflectivity did exist as indicated by a vertical cross section through this region (see Fig. 3.16). Thus, it seems likely that the algorithm misclassified this region. This type of misclassification did not occur as dramatically at earlier times (see Fig. 3.20f). The total area classified as convective was 15412 km^2, and the convective fraction was 36%.

3.6.3 February 15, 1999

Fig. 3.21 shows that the MP algorithm performed well on this case, except at 0630 (see Fig. 3.21g). At this time, the algorithm classified a region of homogeneous reflectivity values as convective (Fig 3.21g, x = -60 to 0; y = 50 to 85). A vertical cross section was investigated; however, the scanning strategy did not provide sufficient vertical coverage of the storm for analysis. The rain gauges in the vicinity recorded rain rates between 5 and 10 mm h^{-1}. The algorithm also classified several localized regions of uniform reflectivity as convective at 0700 (Fig. 3.21h, x = -40 to 10; y = 50 to 100). The rain gauges in the vicinity again indicated rain rates between 5 and 10 mm h^{-1}. It is therefore difficult to conclude that this is stratiform precipitation and that the

classification is in error. The total area classified as convective was 56237 km^2, and the convective fraction was 28%.

3.6.4 February 17, 1999

The MP algorithm captured the convective cells very well in this case (see Fig. 3.22). The storm exhibited strong convection, producing rain rates exceeding 100 mm h^{-1}. The radar images (1km AGL) show isolated cellular structure throughout the case (Fig. 3.22). The accurate identification of convection is therefore expected for this case and was achieved. The total area classified as convective was 12442 km^2, and the convective fraction was 61%.

3.6.5 February 23, 1999

Fig. 3.23 shows the MP classification results for the February 23 case. The MP algorithm successfully isolated the cellular structure in the early periods of the storm (2100 to 2120). At 2130 (Fig. 3.23d), the algorithm continued to identify isolated regions of weak convection. By 2140, a new cell had developed (Fig. 3.23e) and was identified by the algorithm throughout the remainder of the period of analysis. The total area classified as convective was 3266 km^2, and the convective fraction was 22%.

3.6.6 February 27, 1999

The MP classification results for this case are shown in Fig. 3.24. In the early period of the analysis (1000 to 1030), the algorithm identified many small regions of isolated convection. The radar image (Fig. 3.24a) does indicate an isolated cell with 40 dBZ reflectivity (x = -3 km; y = 40 km), which the algorithm labeled convective. However, the classification results in the region to the west of this area (x = -40 km; y = 30 to 40 km) required further investigation. Once again, the K_{dp} rain estimator indicated rain rates greater than 10 mm h^{-1} in these regions. The radar image (Fig. 3.24a) shows a relatively uniform reflectivity field, however, a vertical cross section (Fig. 3.25, y = 40 km N.) does not clearly show a bright band. The coverage by the radar failed to capture the complete vertical structure, but the cross section does not indicate a bright band in the reflectivity field. The structure shown in the cross section is more indicative of weak, decaying convection than stratiform precipitation. The total area classified as convective was 3593 km^2, and the convective fraction was 9%.

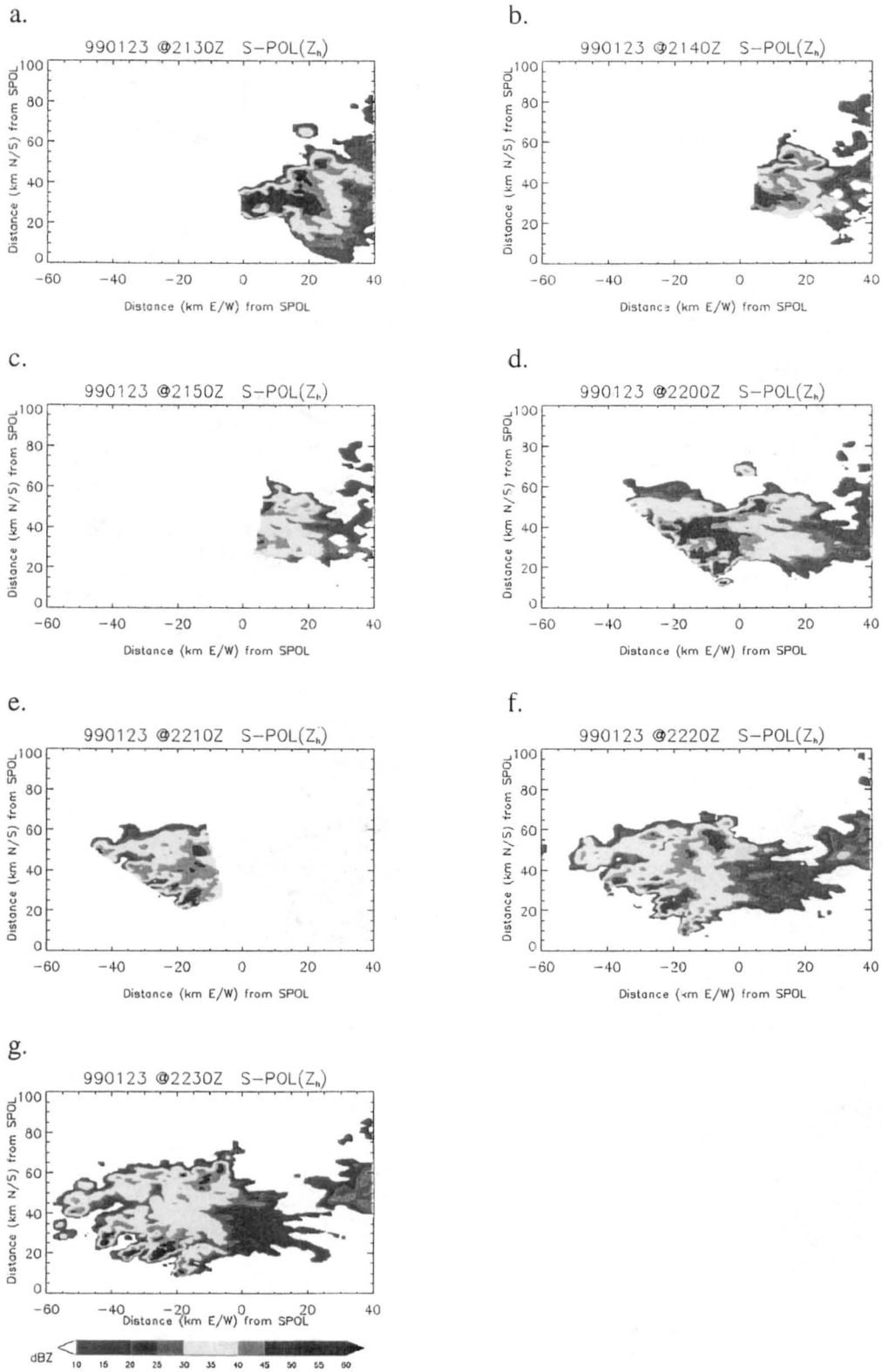

Figure 3.1. Horizontal cross sections of S-pol reflectivity (dBZ) at 1 km AGL on January 23, 1999, showing storm evolution. Images from (a) 2130 UTC, (b) 2140, (c) 2150, (d) 2200, (e) 2210, (f) 2220, and (g) 2230.

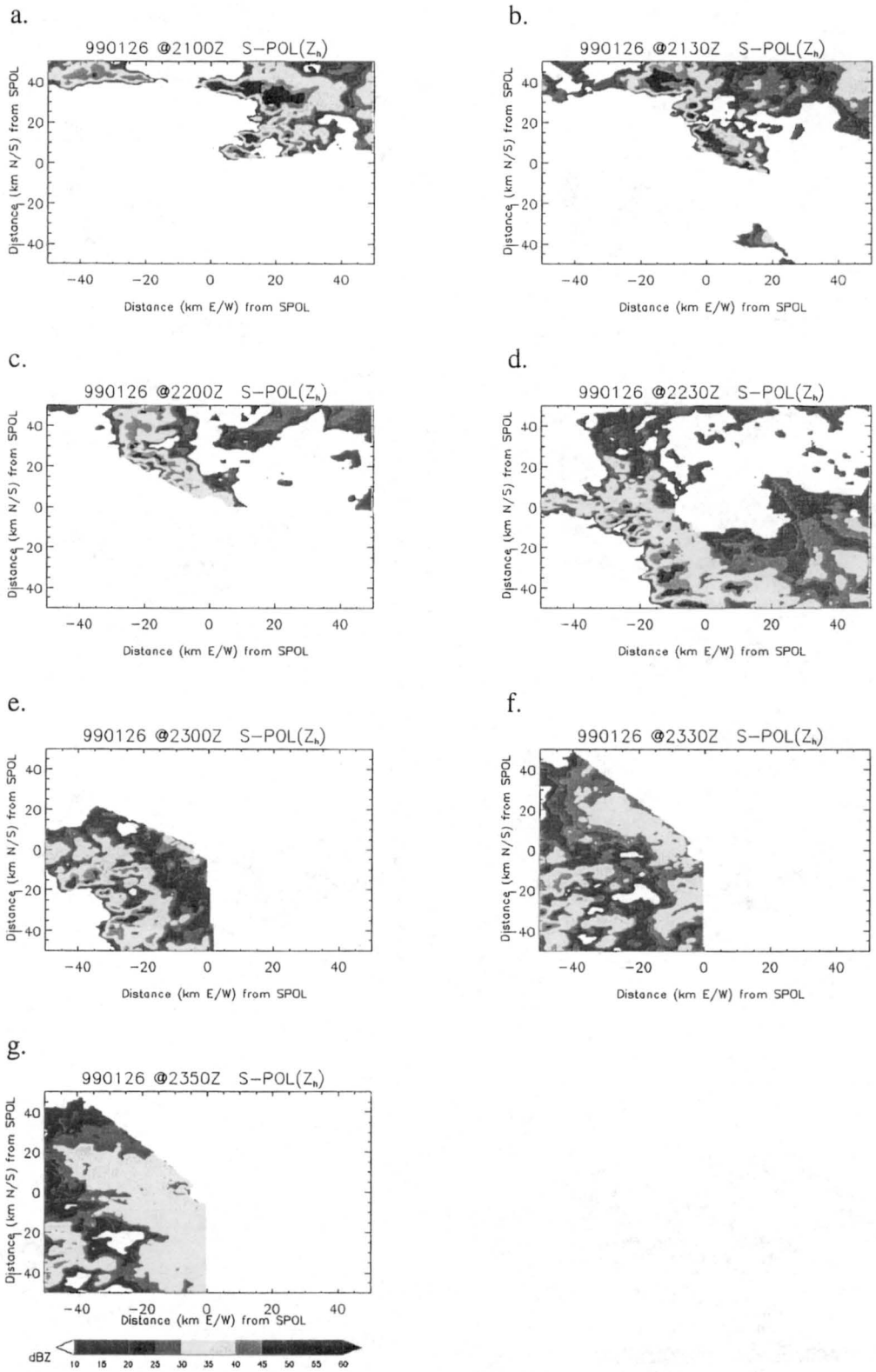

Figure 3.2. Horizontal cross sections of S-pol reflectivity (dBZ) at 1 km AGL on January 26, 1999, showing storm evolution. Images from (a) 2100 UTC, (b) 2130, (c) 2200, (d) 2230, (e) 2300, (f) 2330, and (g) 2350.

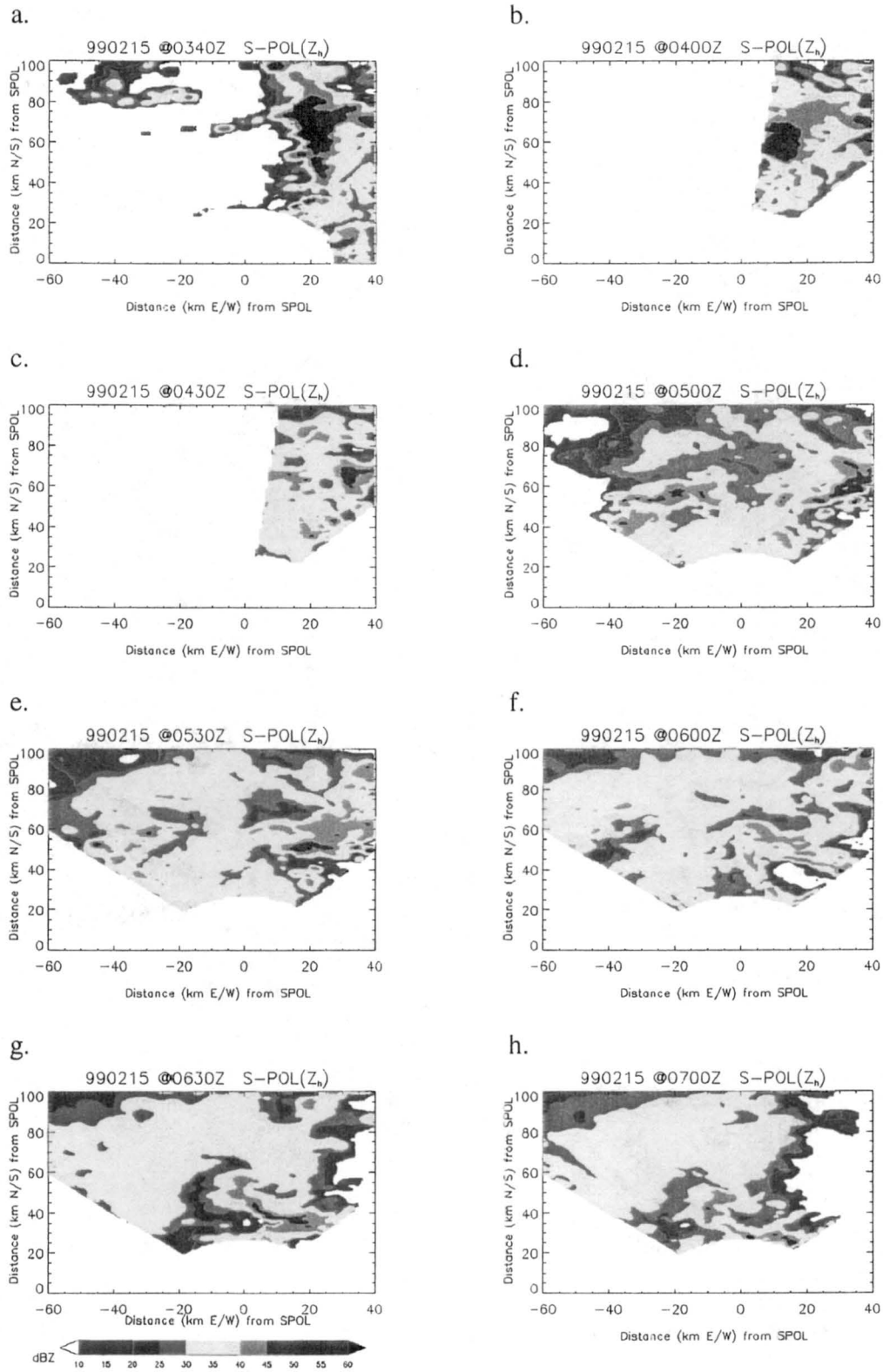

Figure 3.3. Horizontal cross sections of S-pol reflectivity (dBZ) at 1 km AGL on February 15, 1999, showing storm evolution. Images from (a) 0340 UTC, (b) 0400, (c) 0430, (d) 0500, (e) 0530, (f) 0600, (g) 0630, and (h) 0700.

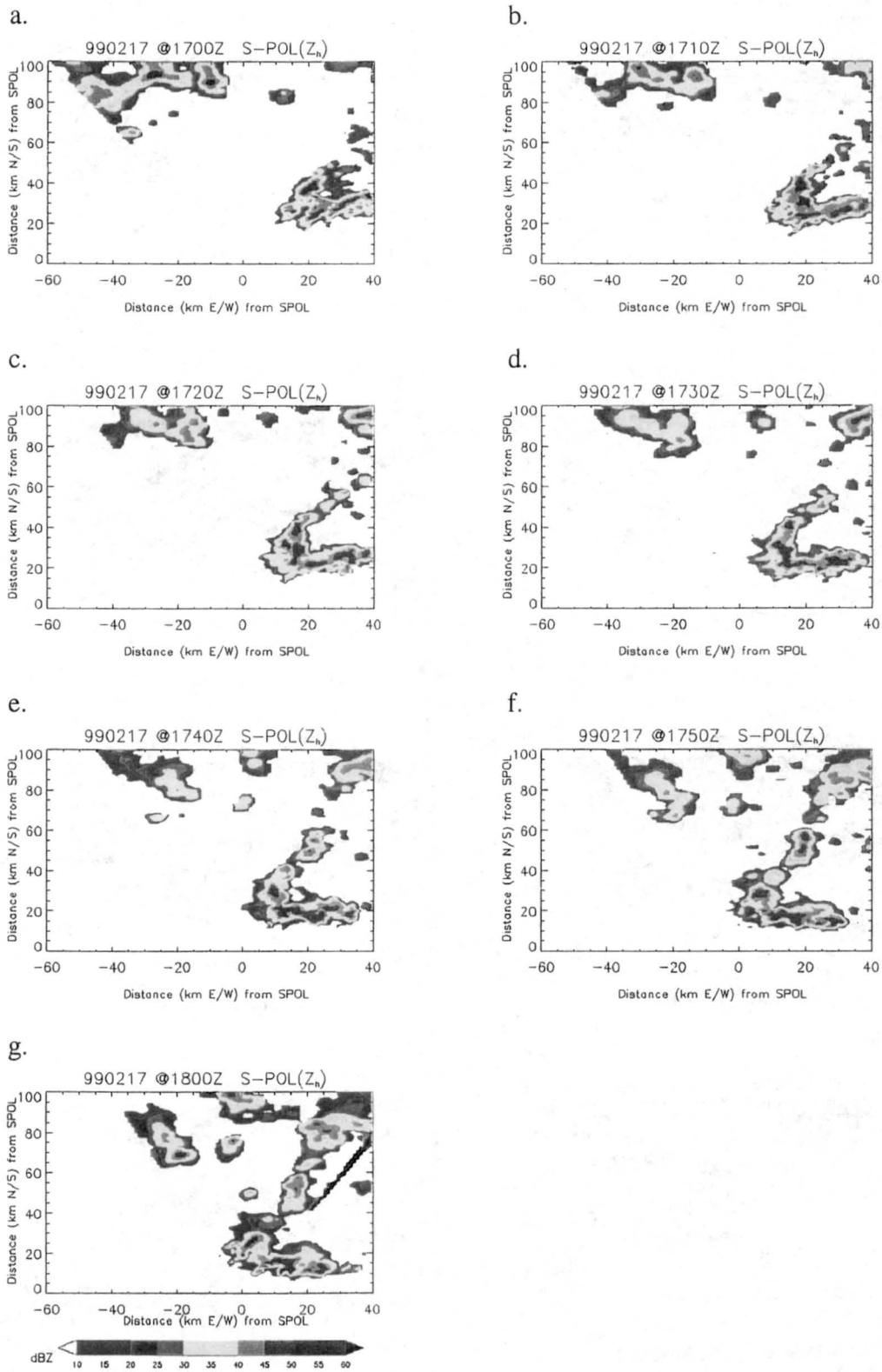

Figure 3.4. Horizontal cross sections of S-pol reflectivity (dBZ) at 1 km AGL on February 17, 1999, showing storm evolution. Images from (a) 1700 UTC, (b) 1710, (c) 1720, (d) 1730, (e) 1740, (f) 1750, and (g) 1800.

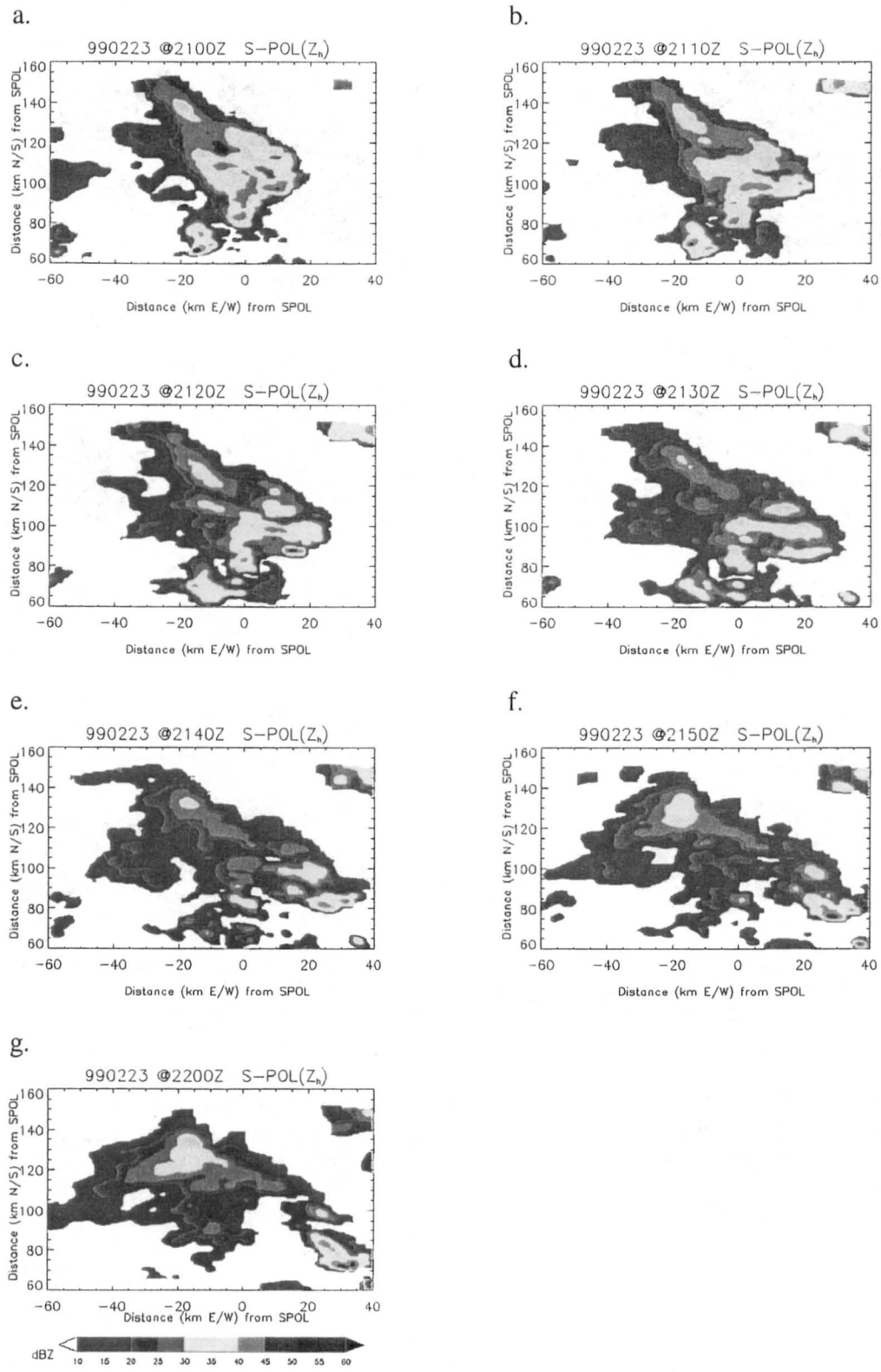

Figure 3.5. Horizontal cross sections of S-pol reflectivity (dBZ) at 1 km AGL on February 23, 1999, showing storm evolution. Images from (a) 2100 UTC, (b) 2110, (c) 2120, (d) 2130, (e) 2140, (f) 2150, and (g) 2200.

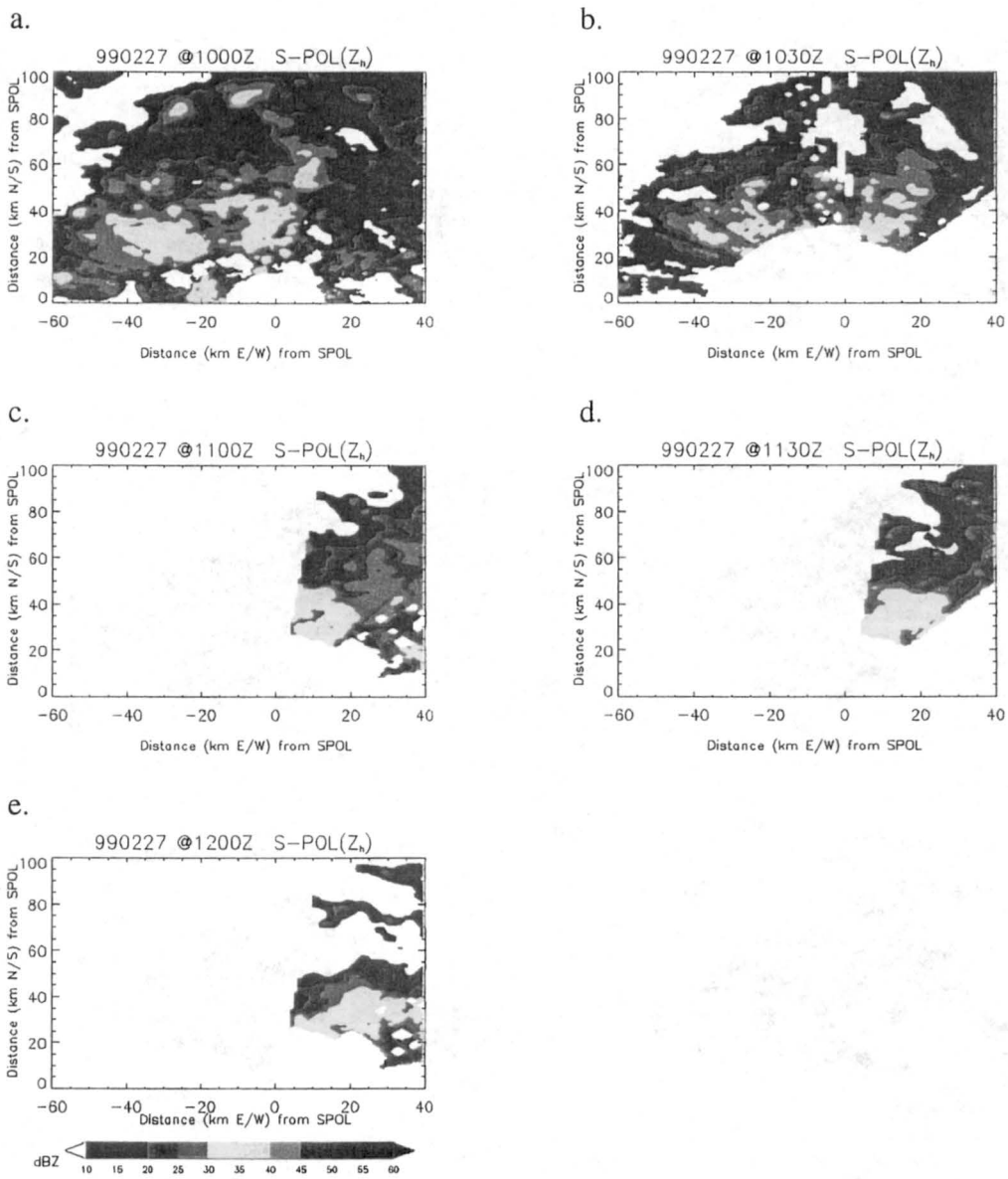

Figure 3.6. Horizontal cross sections of S-pol reflectivity (dBZ) at 1 km AGL on February 27, 1999, showing storm evolution. Images from (a) 1000 UTC, (b) 1030, (c) 1100, (d) 1130, and (e) 1200.

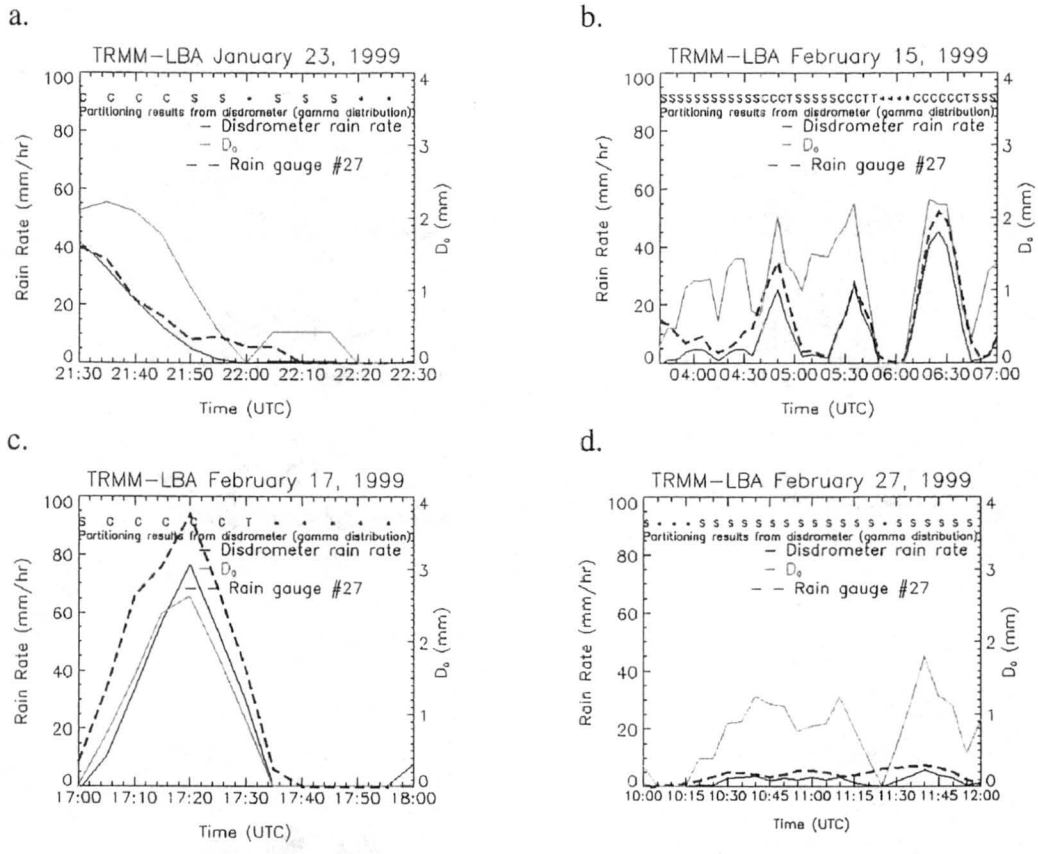

Figure 3.7. Partitioning results from the A99 algorithm on (a) January 23, (b) February 15, (c) February 17, and (d) February 27.

a.

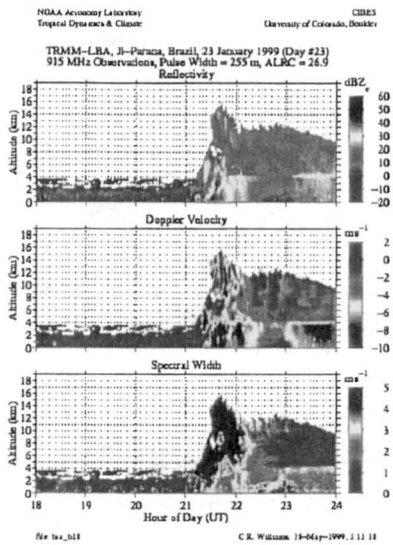

b.

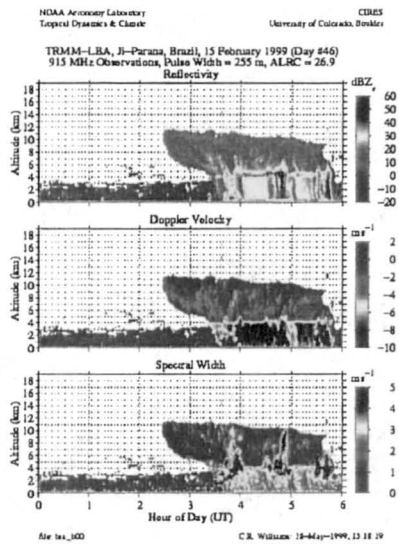

c.

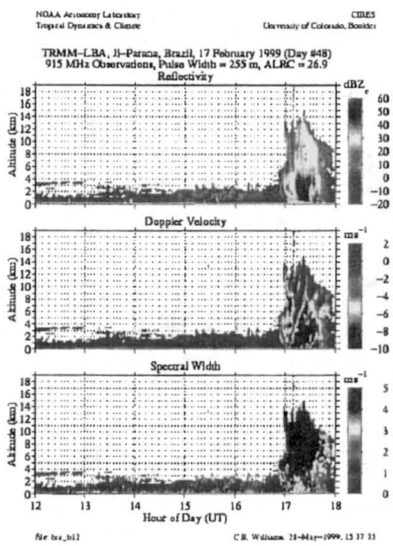

d.

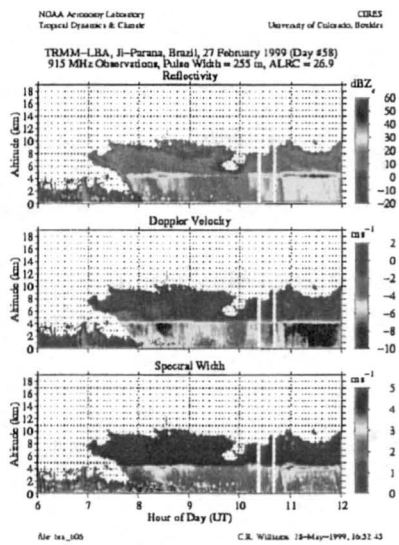

Figure 3.8. 915 MHz Profiler images from (a) January 23, (b) February 15, (c) February 17, and (d) February 27.
Source: NOAA-AL (http://www.al.noaa.gov/WWWHD/pubdocs/trmmlba/al915).

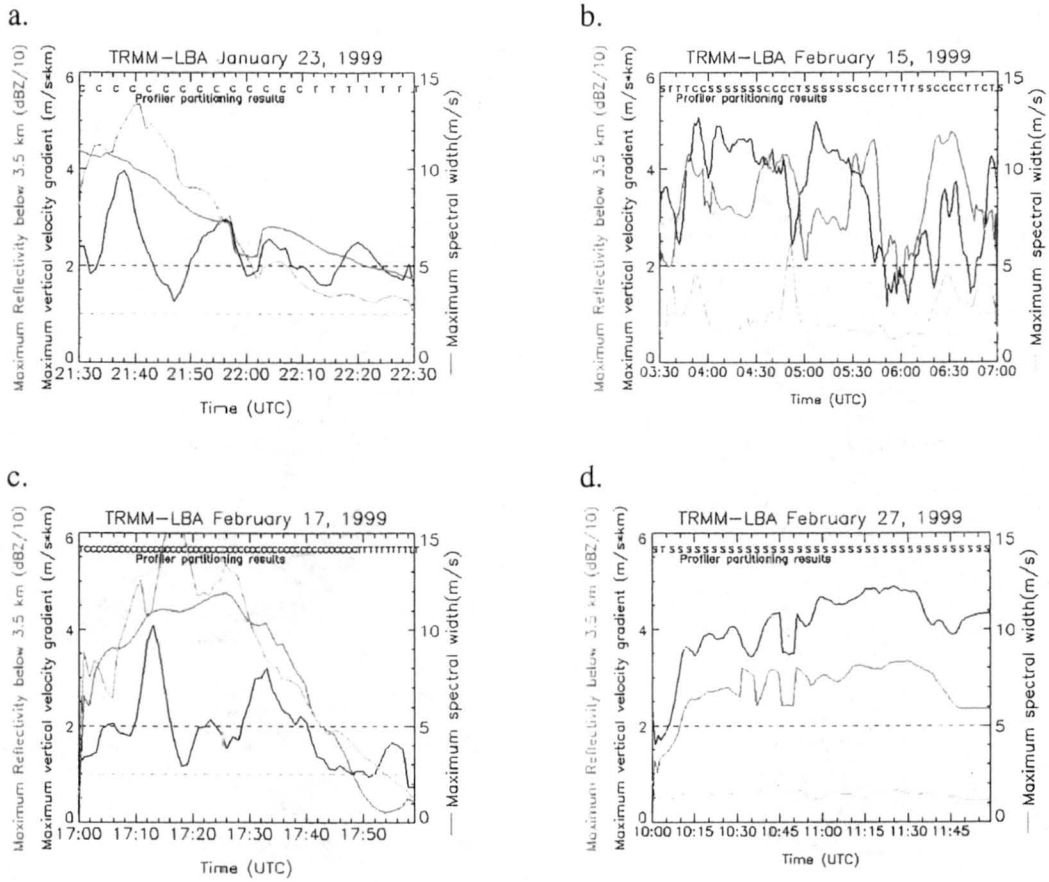

Figure 3.9. Partitioning results from the W95 algorithm on (a) January 23, (b) February 15, (c) February 17, and (d) February 27.

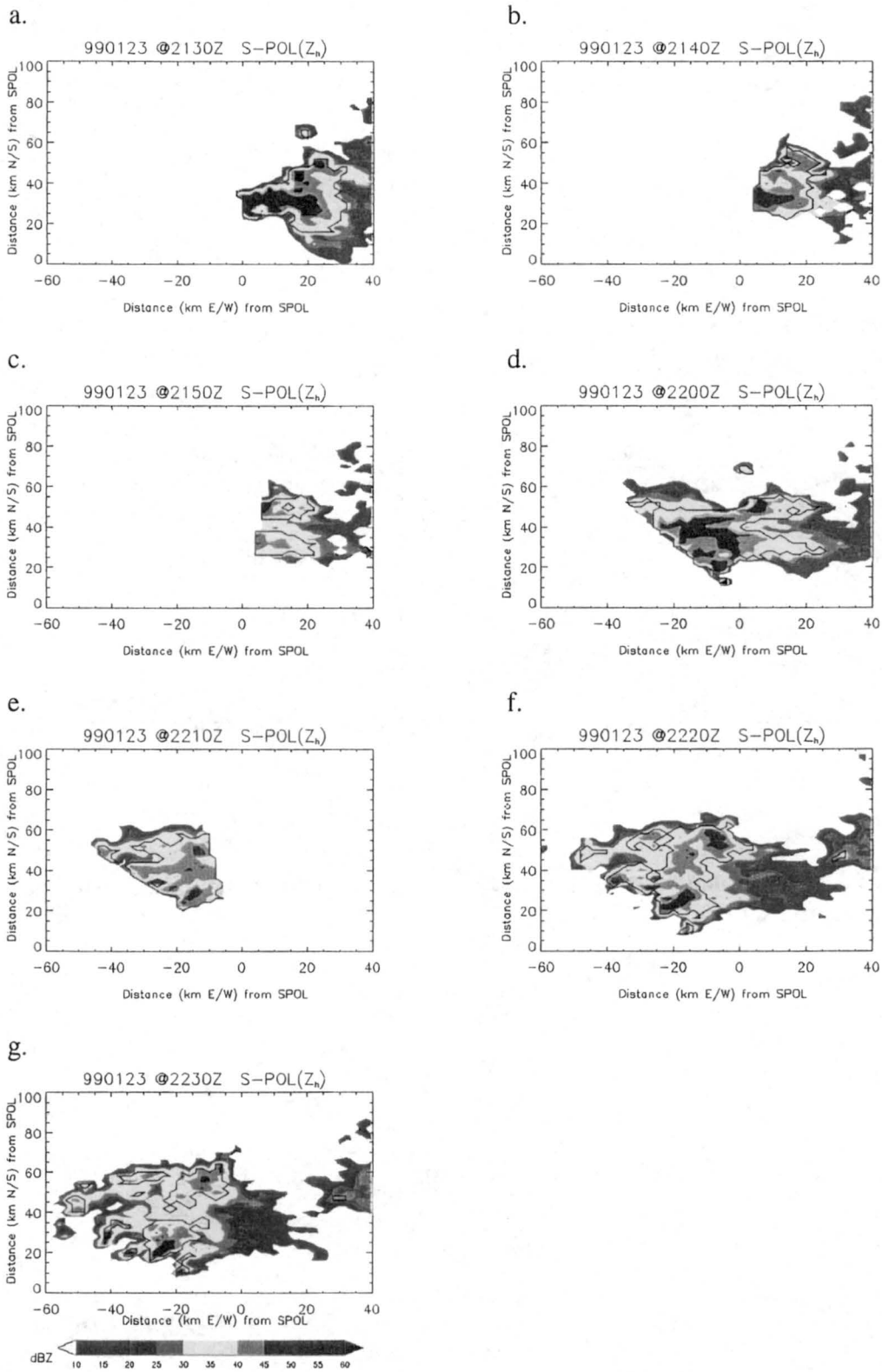

Figure 3.10. Horizontal cross sections of S-pol reflectivity (dBZ) at 1 km AGL on January 23, 1999, showing S95 results (solid contour). Results at (a) 2130 UTC, (b) 2140, (c) 2150, (d) 2200, (e) 2210, (f) 2220, and (g) 2230.

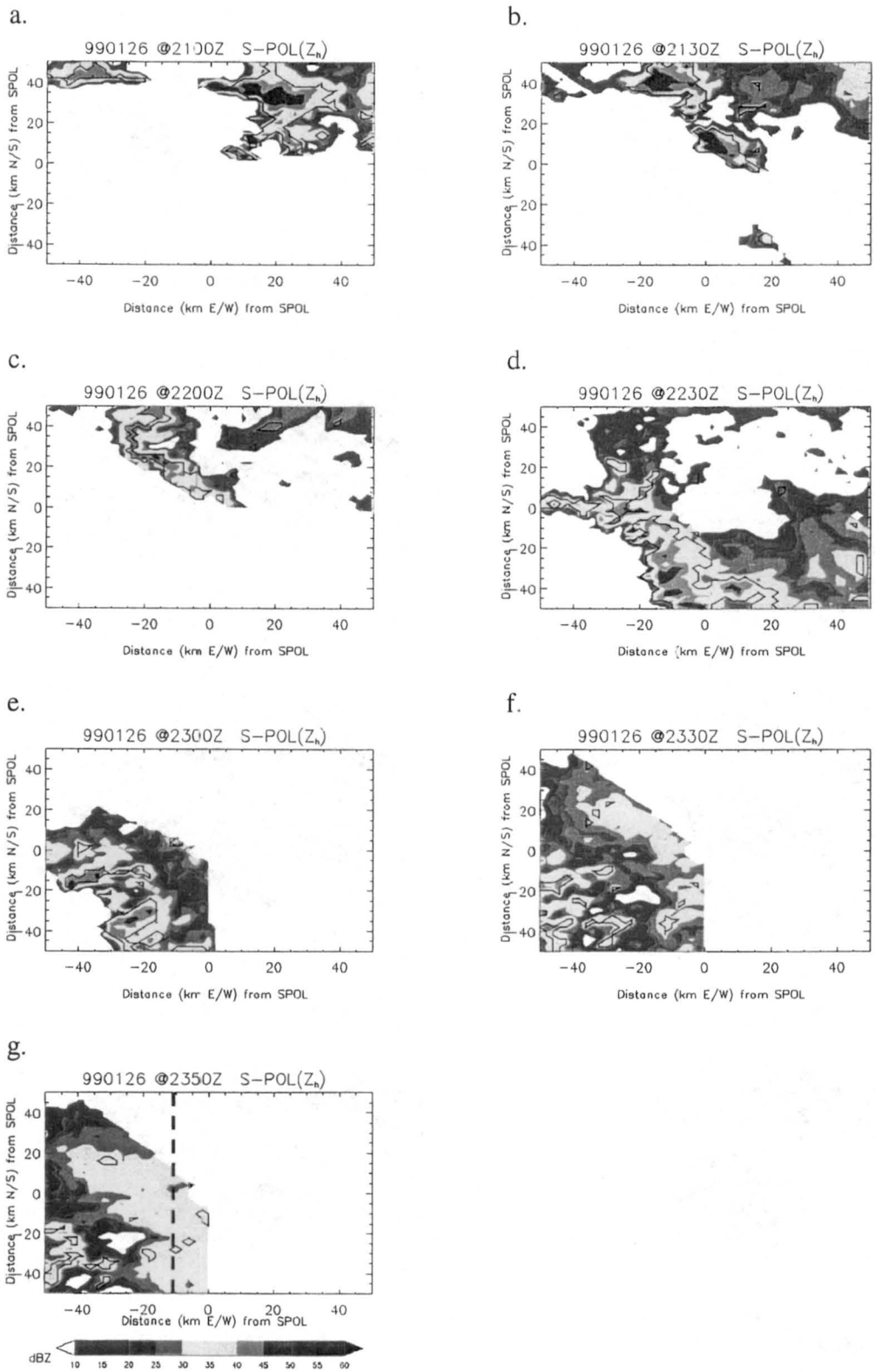

Figure 3.11. Horizontal cross sections of S-pol reflectivity (dBZ) at 1 km AGL on January 26, 1999, showing S95 classification results (solid contour). Results at (a) 2100 UTC, (b) 2130, (c) 2200, (d) 2230, (e) 2300, (f) 2330, and (g) 2350 (Dashed line indicates vertical cross section shown in Fig. 3.16).

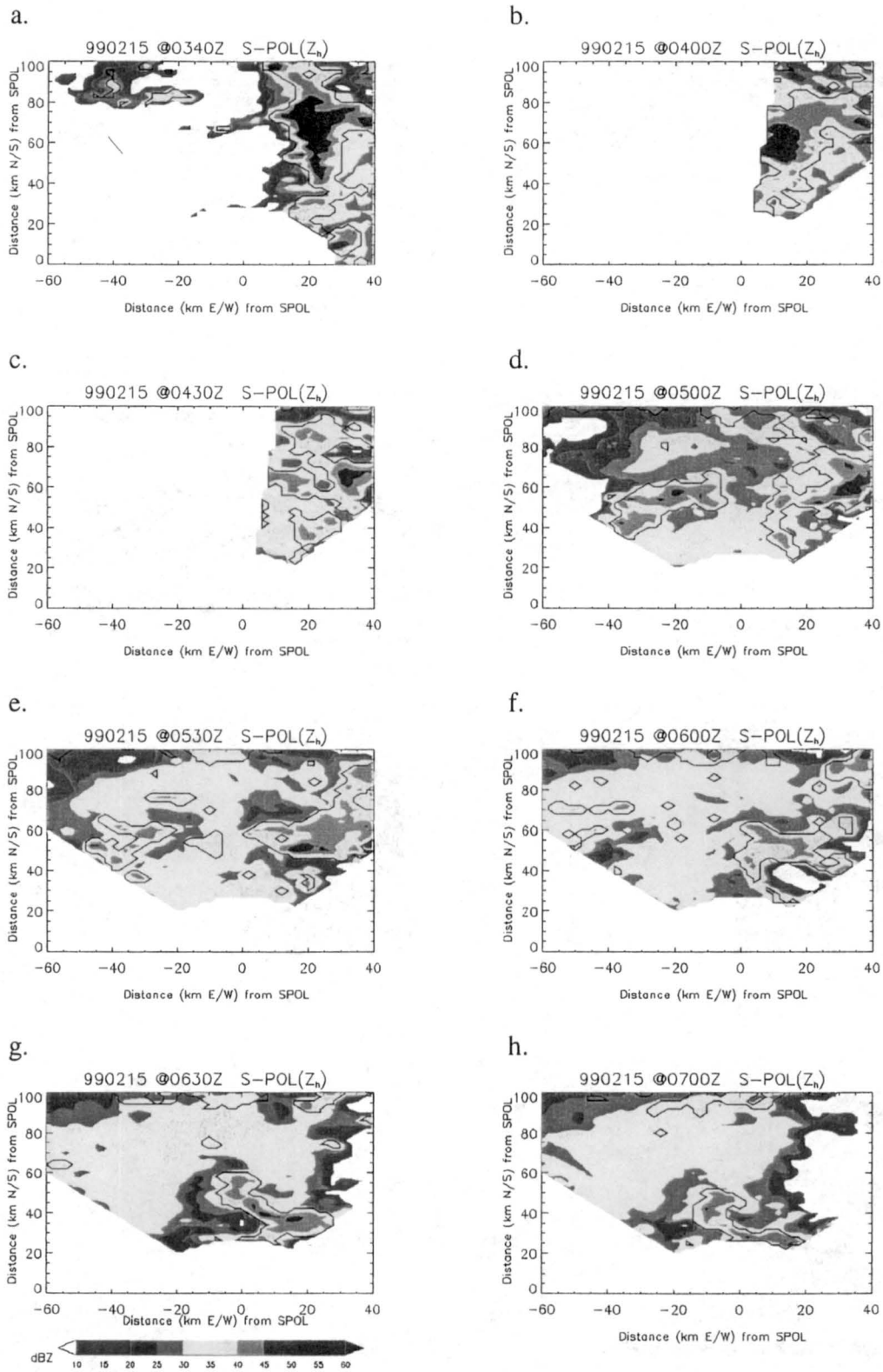

Figure 3.12. Horizontal cross sections of S-pol reflectivity (dBZ) at 1 km AGL on February 15, 1999, showing S95 results (solid contour). Results at (a) 0340 UTC, (b) 0400, (c) 0430, (d) 0500, (e) 0530, (f) 0600, (g) 0630, and (h) 0700.

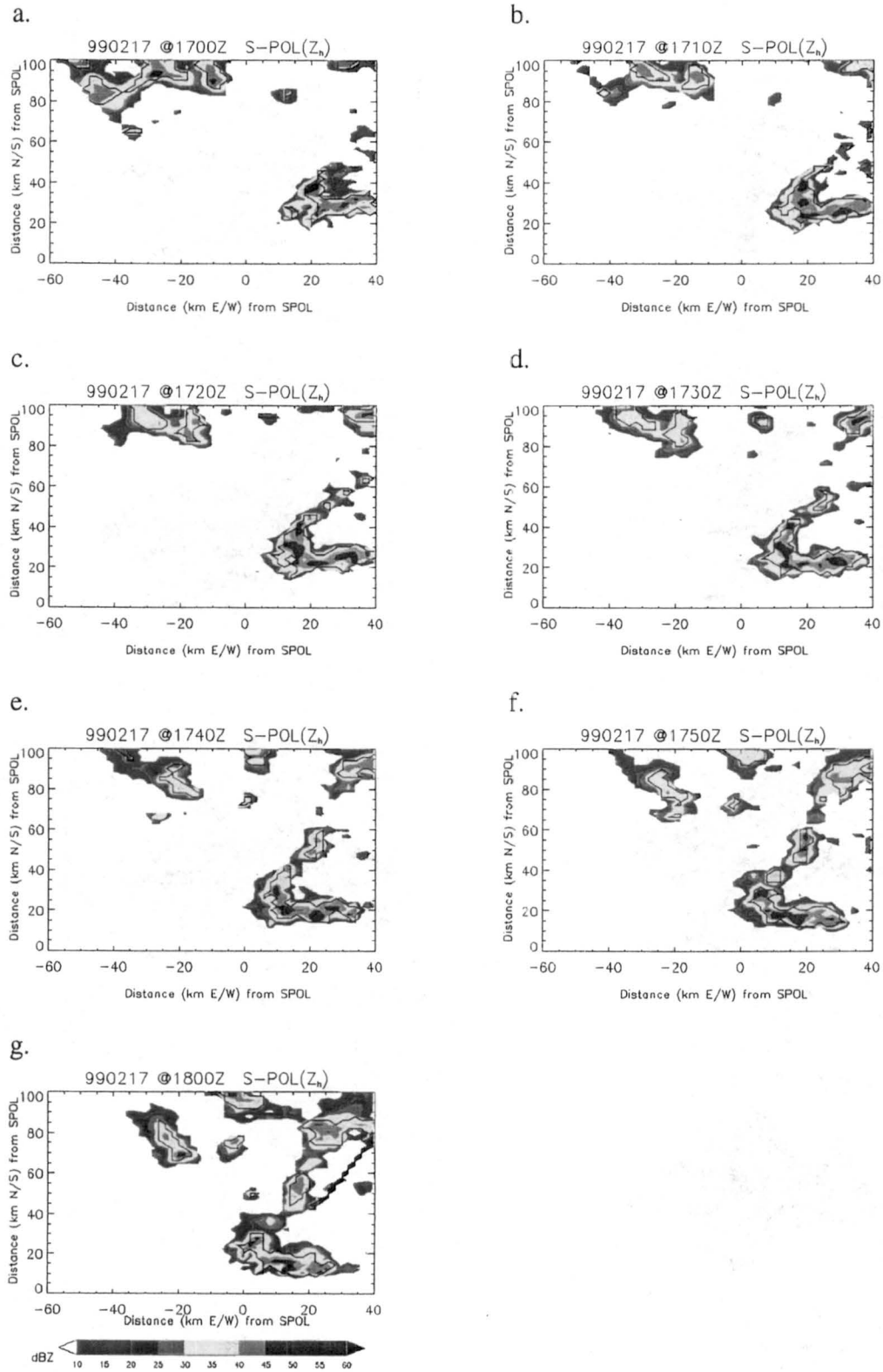

Figure 3.13. Horizontal cross sections of S-pol reflectivity (dBZ) at 1 km AGL on February 17, 1999, showing S95 results (solid contour). Results at (a) 1700 UTC, (b) 1710, (c) 1720, (d) 1730, (e) 1740, (f) 1750, and (g) 1800.

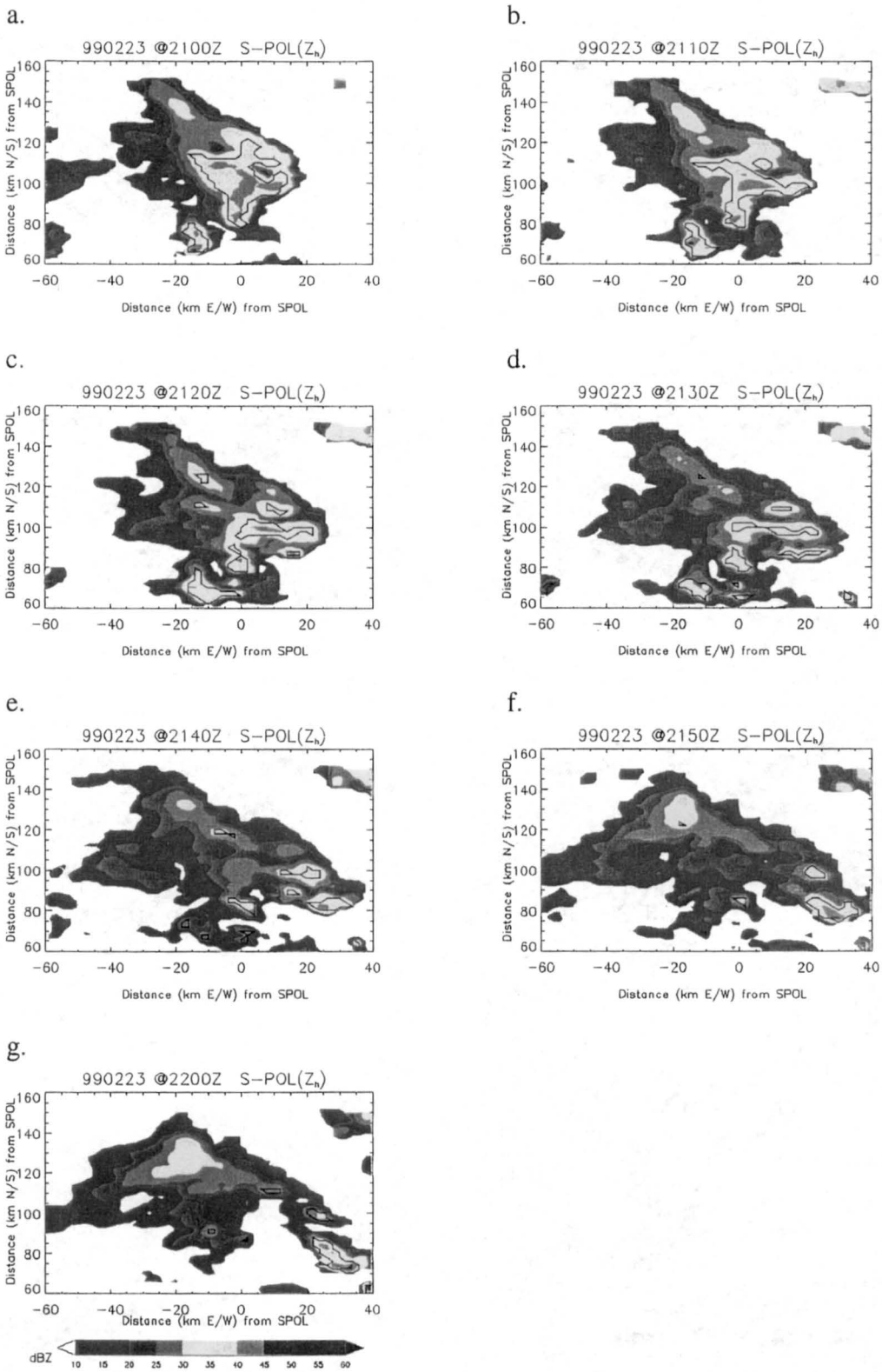

Figure 3.14. Horizontal cross sections of S-pol reflectivity (dBZ) at 1 km AGL on February 23, 1999, showing S95 results (solid contour). Results from (a) 2100 UTC, (b) 2110, (c) 2120, (d) 2130, (e) 2140, (f) 2150, and (g) 2200.

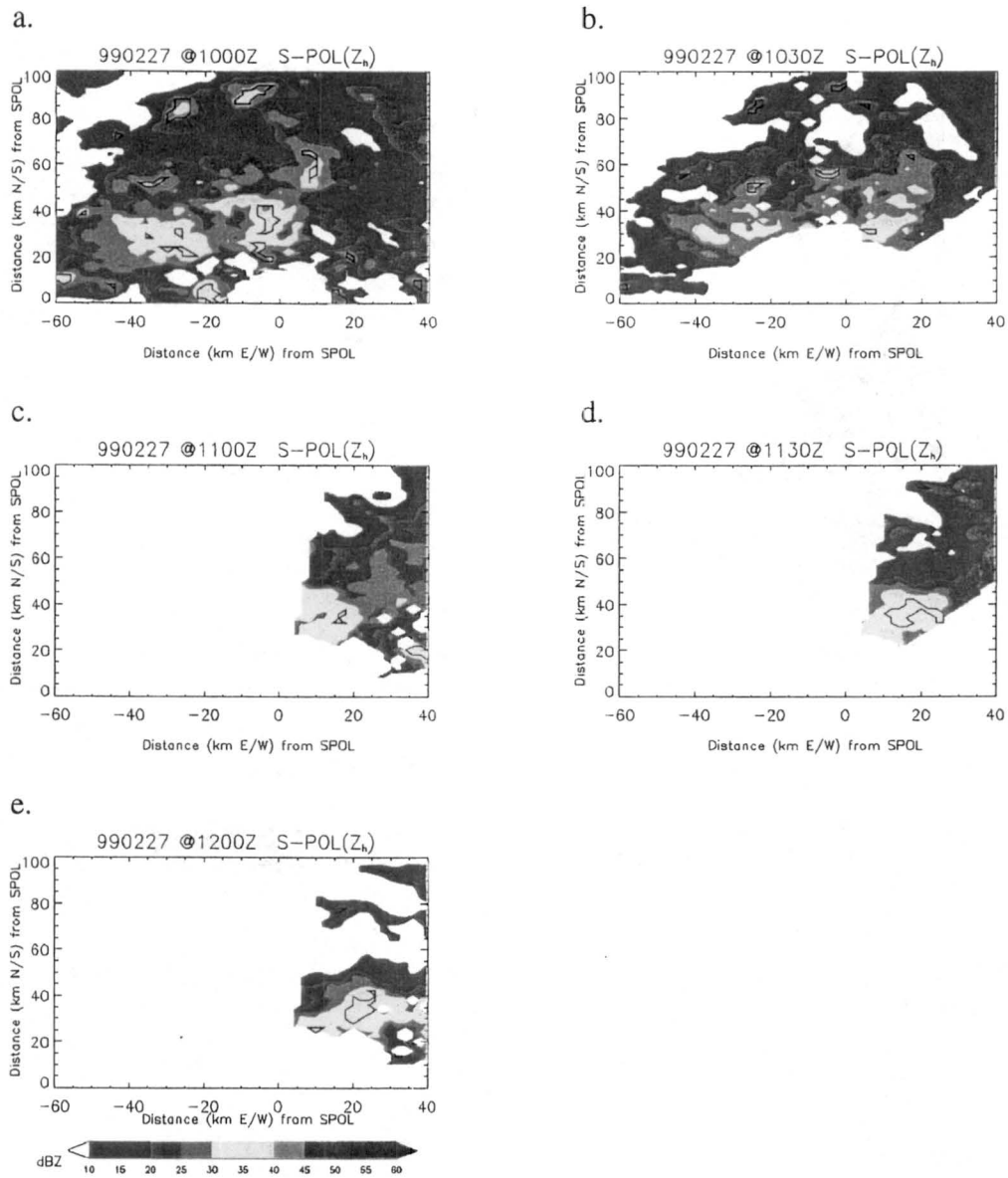

Figure 3.15. Horizontal cross sections of S-pol reflectivity (dBZ) at 1 km AGL on February 27, 1999, showing S95 results (solid contour). Results from (a) 1000 UTC, (b) 1030, (c) 1100, (d) 1130, and (e) 1200.

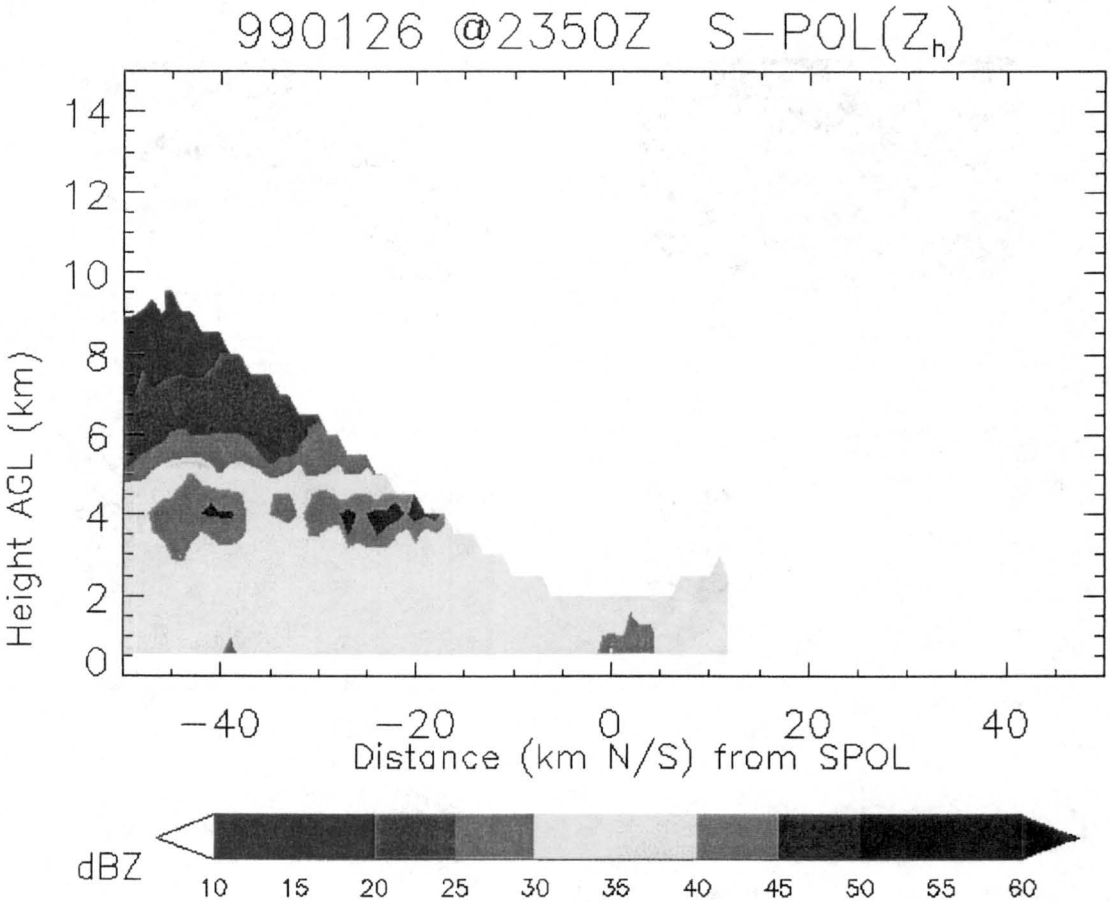

Figure 3.16. North-south vertical cross section of S-pol reflectivity (dBZ) at x = -10 km (see Figure 3.11g).

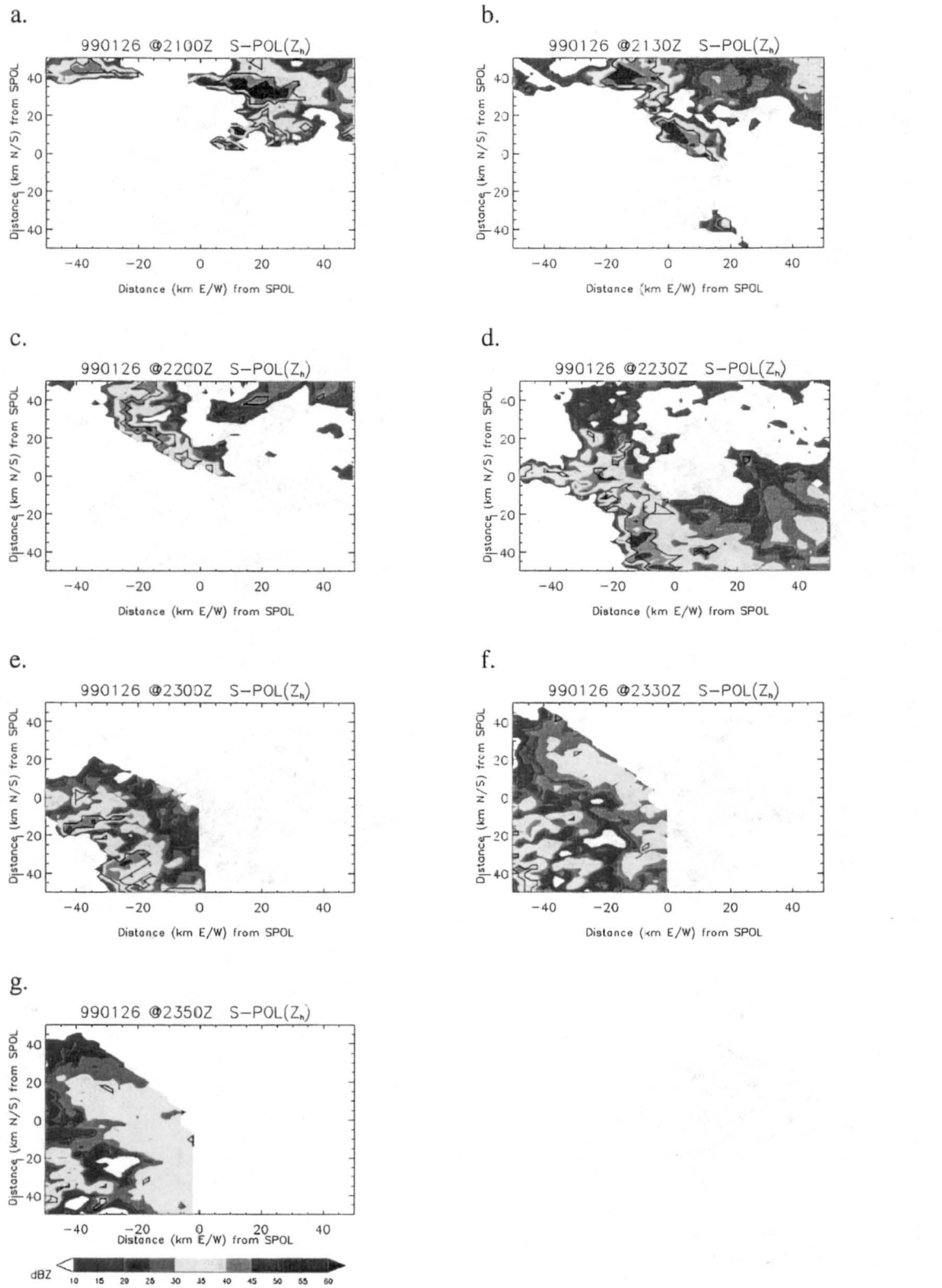

Figure 3.17. Horizontal cross sections of SPOL reflectivity at 1 km AGL on January 26, 1999, showing BL00 partitioning results (contour). Results from (a) 2100 UTC, (b) 2130, (c) 2200, (d) 2230, (e) 2300, (f) 2330, and (g) 2350.

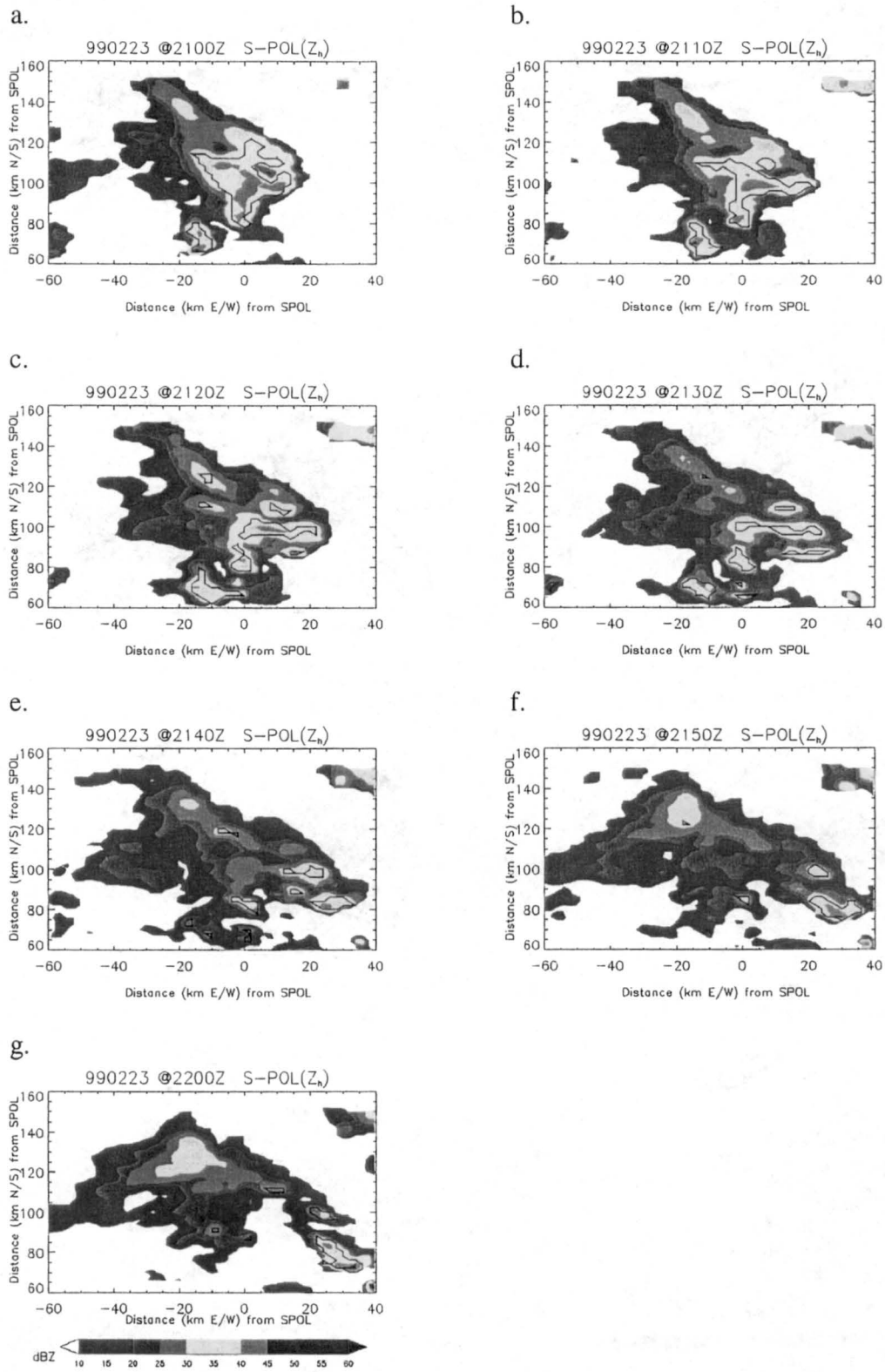

Figure 3.18. Horizontal cross sections of SPOL reflectivity at 1 km AGL on February 23, 1999, showing BL00 partitioning results (contour). Results from (a) 2100 UTC, (b) 2110, (c) 2120, (d) 2130, (e) 2140, (f) 2150, and (g) 2200.

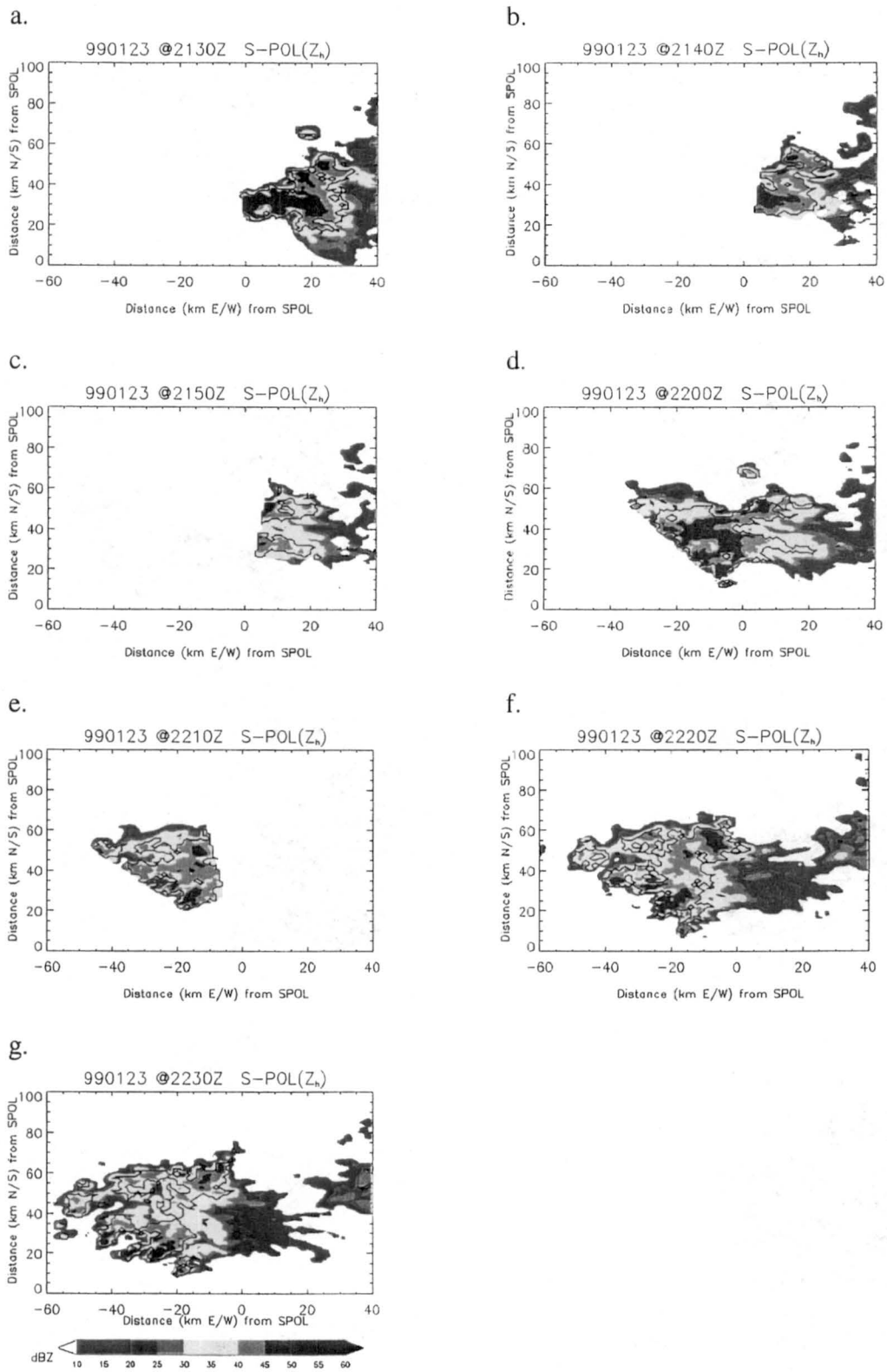

Figure 3.19. Horizontal cross sections of S-pol reflectivity (dBZ) at 1 km AGL on January 23, 1999, showing MP results (solid contour). Results at (a) 2130 UTC, (b) 2140, (c) 2150, (d) 2200, (e) 2210, (f) 2220, and (g) 2230.

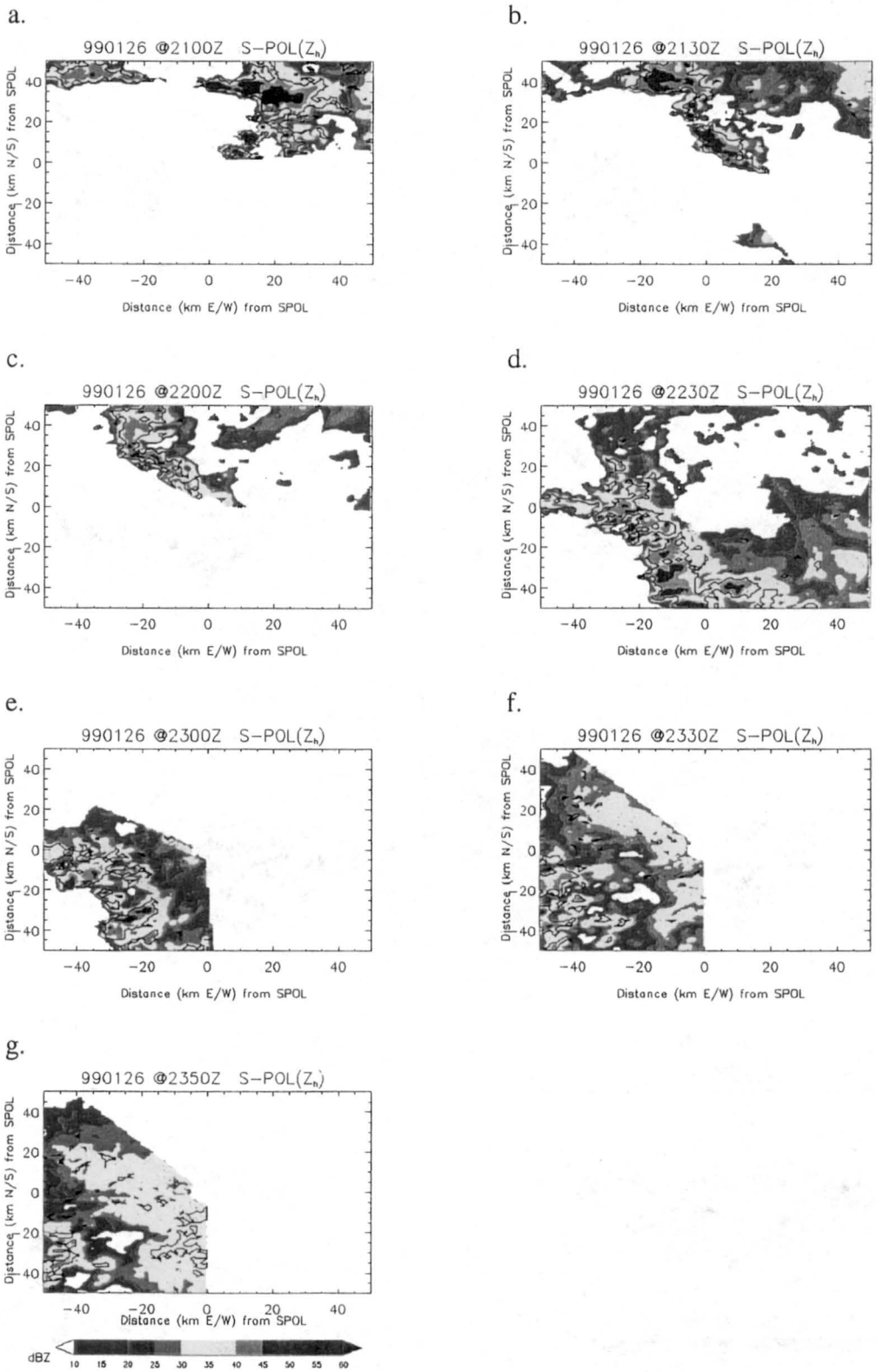

Figure 3.20. Horizontal cross sections of S-pol reflectivity (dBZ) at 1 km AGL on January 26, 1999, showing MP classification results (solid contour). Results at (a) 2100 UTC, (b) 2130, (c) 2200, (d) 2230, (e) 2300, (f) 2330, and (g) 2350.

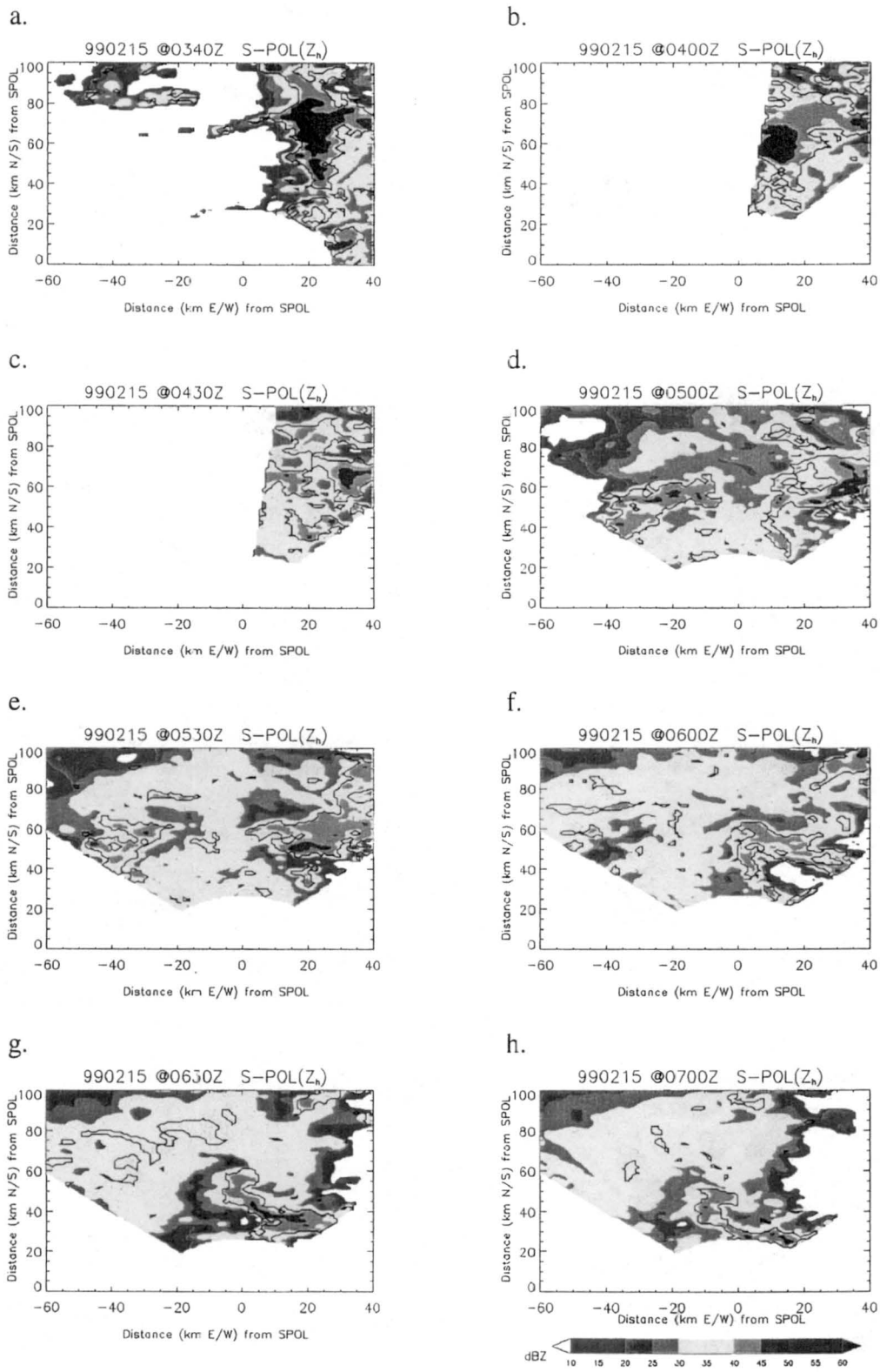

Figure 3.21. Horizontal cross sections of S-pol reflectivity (dBZ) at 1 km AGL on February 15, 1999, showing MP results (solid contour). Results at (a) 0340 UTC, (b) 0400, (c) 0430, (d) 0500, (e) 0530, (f) 0600, (g) 0630, and (h) 0700.

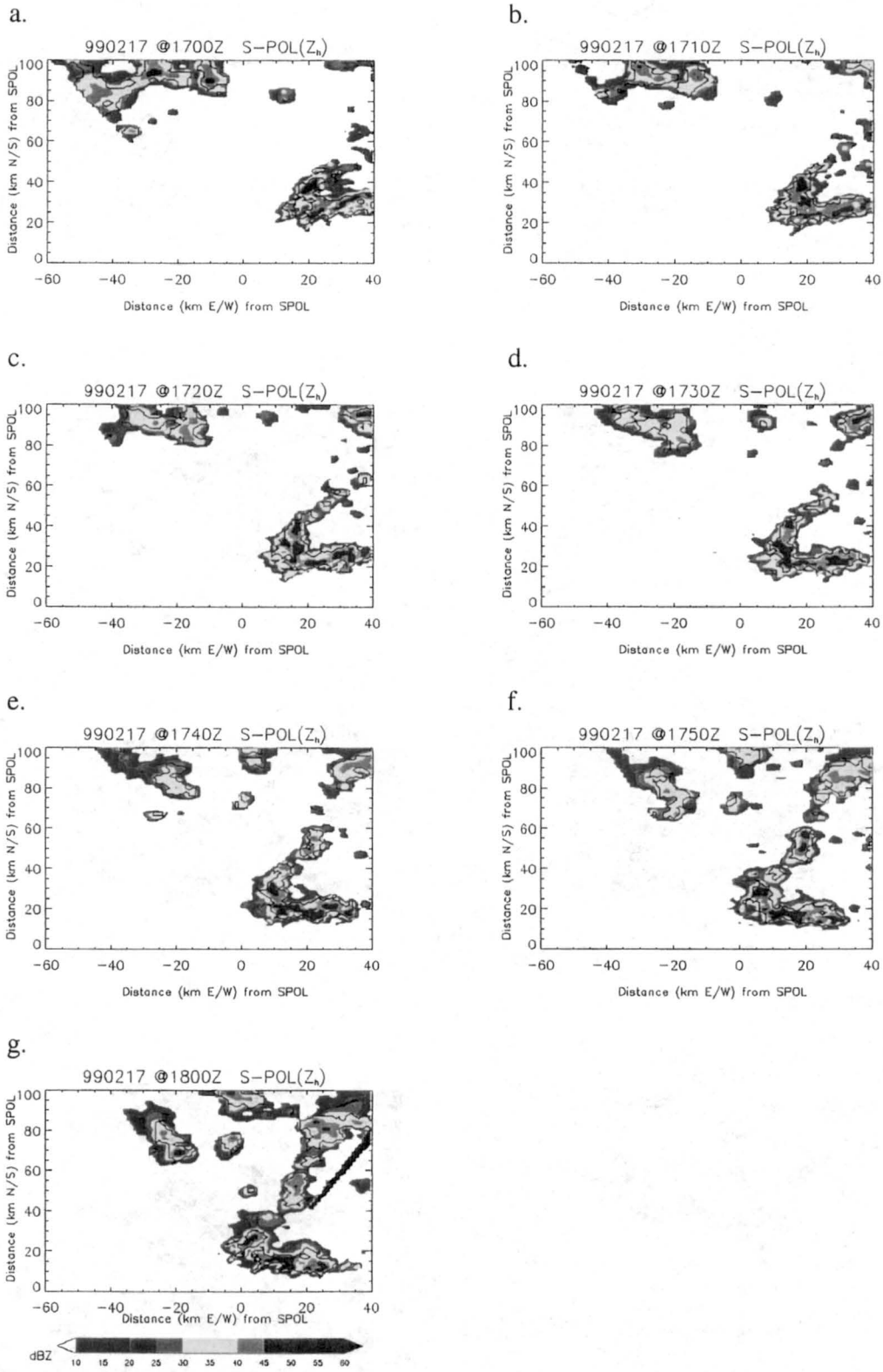

Figure 3.22. Horizontal cross sections of S-pol reflectivity (dBZ) at 1 km AGL on February 17, 1999, showing MP results (solid contour). Results at (a) 1700 UTC, (b) 1710, (c) 1720, (d) 1730, (e) 1740, (f) 1750, and (g) 1800.

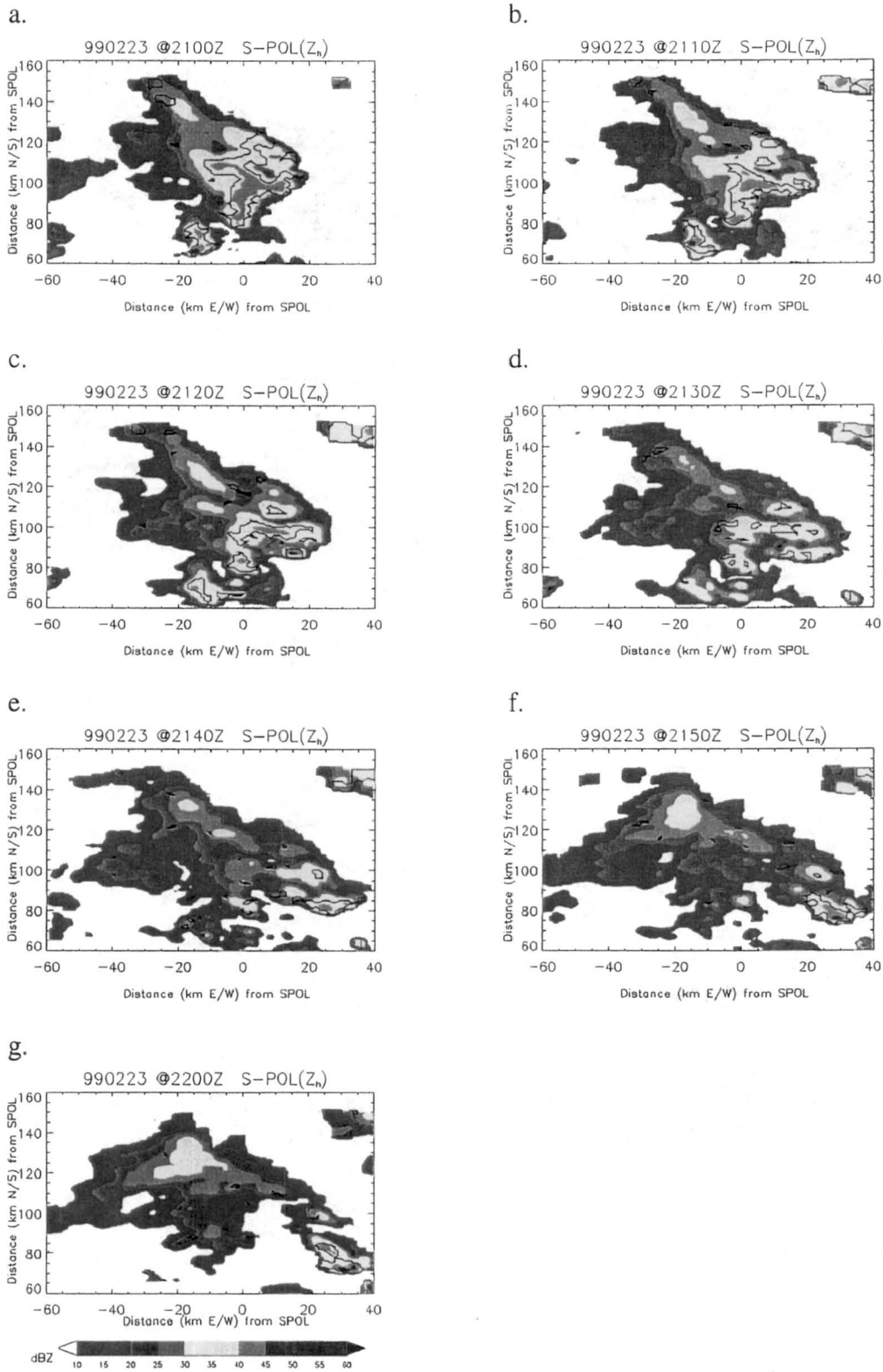

Figure 3.23. Horizontal cross sections of S-pol reflectivity (dBZ) at 1 km AGL on February 23, 1999, showing MP results (solid contour). Results from (a) 2100 UTC, (b) 2110, (c) 2120, (d) 2130, (e) 2140, (f) 2150, and (g) 2200.

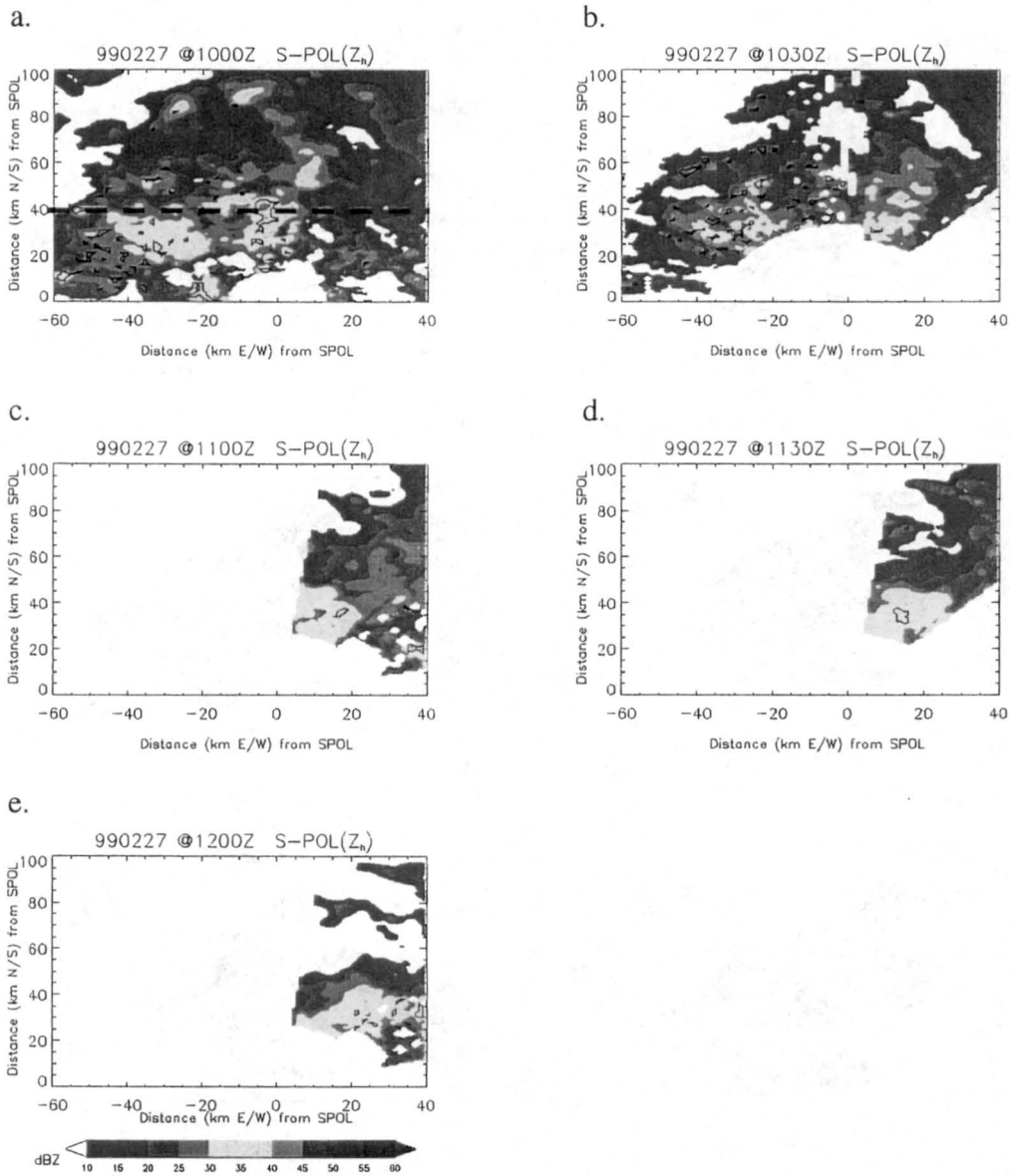

Figure 3.24. Horizontal cross sections of S-pol reflectivity (dBZ) at 1 km AGL on February 27, 1999, showing MP results (solid contour). Results from (a) 1000 UTC, (b) 1030, (c) 1100, (d) 1130, and (e) 1200.

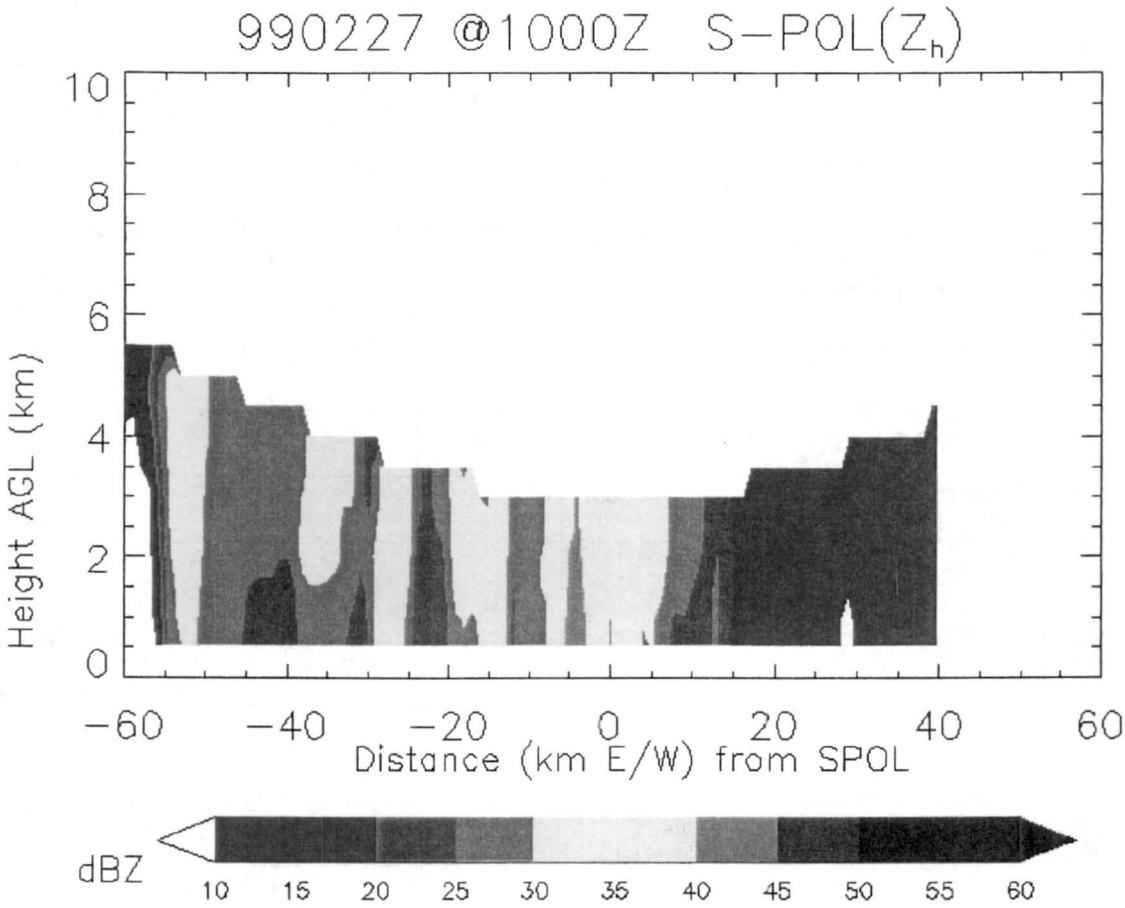

Figure 3.25. East-west vertical cross section of S-pol reflectivity (dBZ) at y = 40 km (see Figure 3.24a).

	Algorithm (Convective area km^2)			*Algorithm (Convective fraction %)*		
Case	*MP*	*S95*	*BL00*	*MP*	*S95*	*BL00*
January 23	9992	11196	-	55	62	-
January 26	15412	15464	11408	36	36	26
February 15	56237	68832	-	28	34	-
February 17	12442	13666	-	60	70	-
February 23	3266	3632	3452	22	25	24
February 27	3593	5636	-	9	14	-

Table 3.1. Convective area and convective fraction for MP, S95, and BL00 algorithms for all cases.

CHAPTER 4

Comparisons between all algorithms

This chapter compares the instantaneous classification results from the MP, A99, W95, and S95 algorithms applied to the 23 January, 15 February, 17 February, and 27 February cases. The classification results are shown at 5-minute intervals. The A99 and W95 algorithms classify precipitation at a single point (i.e. directly over the instruments), while the MP and S95 algorithms classify the entire storm.

In order to compare the instantaneous results of these four algorithms, the results from the MP and S95 algorithms are obtained from the grid-point corresponding to the location of the profiler and disdrometer (Latitude: –10.875°, Longitude: -61.851°). These comparisons provide the opportunity to investigate the accuracy of each classification algorithm during both the "monsoon" and "break-period" meteorological regimes.

The MP and S95 algorithms provided estimates of the total convective area and convective fraction for each case and the BL00 algorithm provided these estimates for the 26 January and 23 February cases. While the ability to classify precipitation instantaneously is important, so to is the ability of the algorithms to identify convection on the storm-scale. These results will also be investigated and compared in this chapter.

Finally, the vertical structure of convection and stratiform from the January 26 case study is investigated. Averaged vertical profiles of the polarimetric variables [Z_h,

Z_{dr}, LDR, K_{dp}, and $\rho_{hv}(0)$] from regions of convection and stratiform (as classified by the MP, S95, and BL00 algorithms) will be compared and analyzed. The radar data for this case provided sufficient vertical coverage to conduct this type of analysis. Furthermore, this case is somewhat representative of all precipitation events investigated in this study (i.e. leading convection/trailing stratiform precipitation).

4.1. Classification comparisons

4.1.1 January 23, 1999

The MP, A99, and S95 algorithms produced identical results for this case (see Table 4.1). The precipitation was classified as convective from 2130 to 2145 and as stratiform for the remainder of the period. The W95 algorithm classified the precipitation as convective from 2130 to 2210 and transition for the remainder of the period. The reflectivity image from the profiler (Fig. 3.8a) does show a region of weaker reflectivity shortly after 2200 and a bright band does not appear until later in the storm (after 2300). This evidence indicates that a transition classification is reasonable. However, the MP and S95 produced a stratiform classification throughout this period (2200 to 2230) since these algorithms only identify convective and stratiform precipitation.

The W95 algorithm maintained a convective classification for a period of 30 minutes beyond the other algorithms. At 2150, the maximum reflectivity values fell below 30 dBZ (Fig. 3.9a), and the rain rate became stable with values around 5 mm h^{-1} (Fig. 3.7a). This indicates that the MP and S95 classification results are likely correct in switching

from convective to stratiform at 2145. The W95 algorithm maintained a convective classification until 2215 due to the high values of spectral width, which remained above 4 m s^{-1} until 2215. In order to correctly identify convection in the presence of high DVG values, we have tuned the W95 algorithm to identify regions of high spectral width as convective (i.e. MSW $\geq$ 4 m s^{-1}). However, in this case it appears that this threshold caused the W95 algorithm to misclassify precipitation.

The absence of a transition period in the A99 results is surprising. However, the classifications shown are at 5-minute intervals. While it is possible to classify precipitation at one-minute intervals using the A99 and W95 algorithms, the MP and S95 algorithms are applied to the radar data at 5-minute intervals. Upon inspection of the A99 results at one-minute resolution, a transition classification did occur from 2146 to 2148. However, since the results presented in Table 4.1 are at five-minute intervals, the times in which the A99 algorithm produced a transition classification do not appear in the table.

4.1.2 February 15, 1999

There is disagreement among the classification results during this case at several different times (see Table 4.2). At the beginning of the case (0340), G27 recorded rain rates in excess of 10 mm h^{-1}, which fell off to around 3 mm h^{-1} by 0415. The reflectivity in the lower levels (Fig. 3.8b) exceeded 40 dBZ for a short period at 0400 while the MSW exceeded 4 m s^{-1} (Fig. 3.9b). The MP, W95, and S95 algorithms correctly identified convection at this time, while the A99 algorithm indicated stratiform

precipitation. The rain rates recorded by the disdrometer during this period were below 5 mm h^{-1}, thus contributing to the misclassification.

At 0430, the rain rate began to increase as did the reflectivity and MSW recorded by the profiler. The W95 algorithm indicated the onset of a second convective event, while the S95 classification was convective five minutes earlier. The MP algorithm indicated convection starting at 0420, while the A99 algorithm maintained a stratiform classification until 0440. It is reasonable to expect this type of mistiming during the event among the four algorithms given the wide variety of thresholds that produce a convective classification. However, based on the time at which the rain rate began to increase, it appears that the S95 algorithm most accurately captured the onset of convection.

By 0500, all of the algorithms indicated a stratiform classification. At 0525, the rain rate exceeded 10 mm h^{-1}, and began increasing. The reflectivity and D_0 (see Fig. 3.7b) also began to increase indicative of the onset of the third period of convection. By 0530, all of the algorithms are in agreement, indicating convection. At 0535, the MP, W95, and S95 results show a short stratiform period followed again by a convective classification. This suggests that the precipitation at this time was likely weak, disorganized convection. This was confirmed by inspecting the time-series of radar images (not shown) at this time, which indicated an area of weak convection over the profiler, which rapidly decayed.

At 0605, the rain rate and D_0 began to increase sharply (see Fig. 3.7b) as did the MZ (see Fig. 3.9b), indicating the onset of the final convective event during the time period analyzed. By 0610, the A99 and S95 results indicate convection, and the MP results

show convection at 0615. The W95 results show a transition classification starting at 0545, but then switches to stratiform at 0610. The W95 convective classification began at 0620, slightly later than the remaining algorithms.

4.1.3 February 17, 1999

The rain rate and D_0 (see Fig. 3.8c) began increasing at the beginning of this case (1700), while MZ and MSW (see Fig. 3.10c) also increased at this time. The G27 rain rate exceeded 10 mm h^{-1} at 1705 and rose to a peak of 97 mm h^{-1} by 1725, associated with a strong convective shower. The reflectivity values shown in the profiler image (see Fig. 3.8c) clearly indicate a strong isolated convective cell. All of the algorithms are in agreement (see Table 4.3) indicating convection at 1705. The A99 algorithm terminated the convective classification at 1730, followed by a brief transition period. From 1735 to the end of the period, the A99 algorithm was unable to classify the precipitation, since the disdrometer was no longer recording data beyond this point.

The MP and S95 algorithms indicated stratiform precipitation from 1740 to the end of the period of analysis. The W95 algorithm did, however, continue to indicate convection until 1750, followed by a transition classification until the end of the period. The MSW remained above the 4 m s^{-1} convective threshold until 1750 causing the W95 algorithm to maintain a convective classification for a longer period than the A99, S95, and MP algorithms.

4.1.4 February 27, 1999

All of the algorithms produced similar results for this case (see Table 4.4) throughout most of the period of analysis. The A99 and W95 results show a stratiform classification from 1010 until 1155. The MP and S95 results show a stratiform classification from 1005 to 1130 and a convective classification from 1130 to 1145. During this period (1130-1145), D_0 increased to almost 2 mm (see Fig. 3.7d), and the rain rates approached 7 mm h^{-1}. The profiler image (see Fig. 3.8d) indicated a melting layer signature throughout the case, but does show an increase in the Doppler velocity (up to 10 m s^{-1} downward) around 1130. The radar images (see Fig. 3.6a-d) indicate the presence of a weakening convective cell, however the S95 and MP algorithms appear to be in error at 1130.

4.2. Convective area and fraction

4.2.1 January 23, 1999

The total convective area and storm convective fraction results produced by the three algorithms (MP, S95, and BL00) are in reasonable agreement (see Table 3.1). The S95 algorithm produced 12% more convective area than the MP algorithm for this case. The convective fraction produced by S95 was 62% (7% greater than the MP results). This result is substantially higher than the results obtained by S95 (12%), in which the S95 algorithm was applied to an entire month of radar data (February, 1988) in Darwin,

Australia. However, the radar scanning strategy could easily influence the convective fraction for a given storm. By focusing on individual cells rather than scanning large areas, the convective fraction would increase.

4.2.2 January 26, 1999

The MP, S95, and BL00 algorithms were applied to this case, with the MP and S95 convective area and fraction results in near perfect agreement (see Table 3.1). The BL00 convective area results are nearly 36% lower than the MP and S95 results, and the convective fraction is 10% lower. As mentioned in section 3.4.2 and 3.6.2, the S95 and MP algorithms produced convective classifications in regions of weak, uniform reflectivity that were likely misclassified. The BL00 algorithm was successful in reducing the errant classifications as observed in the lower convective area and convective fraction results.

4.2.3 February 15, 1999

The time period for this case was the longest of all of the case studies. The large values of convective area (see Table 3.1) are evidence of this. The S95 algorithm produced 22% more convective area than the MP algorithm, and the S95 convective fraction was 6% higher than the MP results. As mentioned in section 3.4.3 and 3.6.3, both algorithms classified regions of uniform reflectivity as convective near the end of the analysis period (see Fig. 3.12 and 3.21). The scanning strategy for this precipitation

event did not provide sufficient vertical coverage to apply the BL00 algorithm. However, a horizontal gradient threshold was applied to the S95 algorithm results (see Fig. 4.1), and the convective area decreased, suggesting that the BL00 algorithm would likely produce a lower value for the convective area.

4.2.4 February 17, 1999

The MP and S95 convective area and fraction results were within 10% of each other for this case (see Table 3.1). This case was a very strong convective event (discussed in section 3.1) and the convective fraction values reflect this point. The S95 algorithm classified 70% of the rain as convective with a value of 60% shown in the MP results.

4.2.5 February 23, 1999

The S95 convective area results were 11% higher than the MP and 5% higher than the BL00 results for this case (see Table 3.1). The convective fraction results produced by each algorithm are in good agreement, indicating that a significant portion of the precipitation from this event was stratiform. A TRMM satellite overpass occurred in the region covered by the S-pol radar early in this case (2100 and 2105). The TRMM-2A23 algorithm was applied to the PR data at 2100 and produced a convective area of 1024 km^2 (see Fig. 4.2). The MP, S95, and BL00 algorithms produced 730 km^2, 820 km^2, and 816 km^2 respectively, for the same time period. The TRMM-2A23 algorithm was applied to a larger area than the MP, S95, and BL00 algorithms, which included several

cells outside the region analyzed by the S95, BL00, and MP algorithms. These additional regions lead to a higher estimate of convective area by the TRMM-2A23 algorithm.

4.2.6 February 27, 1999

This case produced mostly stratiform precipitation, and this is reflected in the lower convective area results from each algorithm (see Table 3.1). The S95 convective area results were 56% higher than the MP results. However, as noted in section 3.4.6 and 3.6.6, the S95 and MP algorithms may have over-estimated convection for this storm. The convective fraction results may also be slightly high, especially given the fact that the rain rates during the period of analysis rarely exceeded 5 mm h^{-1}.

4.3. Vertical structure

The vertical profiles of Z_h, Z_{dr}, LDR, K_{dp}, and $\rho_{hv}(0)$ averaged at each level (0.5 to 8.0 km AGL) in convective and stratiform precipitation (as classified by the MP, S95, and BL00 algorithms) will now be investigated. The inclusion of the multiparameter radar variables in this type of analysis provides information about the size, shape and thermodynamic phase of the hydrometeors, and they can be used to test consistencies with the various algorithms. The goal here is to confirm that the vertical structure (inferred) of the polarimetric variables, in regions identified as convective and stratiform by the various algorithms, are consistent with convective and stratiform precipitation processes. Doviak and Zrnić (1993) provide a thorough discussion concerning the use of

the multiparameter radar variables to infer hydrometeor phase and type. The discussion that follows utilizes information provided by these authors.

The results shown in Fig. 4.3, 4.4, and 4.5 were produced using the MP, S95, and BL00 classification results respectively. The magnitudes of each profile from the MP results are higher than the S95 and BL00 at lower levels. The MP algorithm was applied to radar data of higher resolution and less smoothing likely occurred during the Cartesian interpolation, thus producing higher values in the averaged profiles. However, given the similarity in the trends of the profiles, only the MP based results will be discussed here.

The convective Z_h profile is nearly 10 dB higher than the stratiform profile at 1 km. This confirms that the algorithm is successfully identifying regions containing more hydrometeors (i.e. higher rain rates) as convective. The convective Z_h profile also decreases gradually from 2 km up to 6 km, inferring the absence of a melting layer. The stratiform Z_h profile increases with height up to 4 km and indicates a bright band signature at this level, 1 km below the melting level (0° C isotherm). The convective and stratiform profiles decrease with height below 1 km, implying drop break-up and evaporation processes are occurring. The convective Z_h profile shows slightly lower values than the stratiform profile in the region above 7 km. The storm passed directly over the S-pol radar thus limiting the vertical coverage of the convection. This likely reduced the magnitude of the convective Z_h profile in the upper levels.

The convective Z_{dr} profile is 0.5 dB higher than the stratiform profile at 1 km, implying the presence of larger raindrops in the convective profile than in the stratiform profile at this level. In convective precipitation, the primary growth mechanism is collision and coalescence (Houze, 1993). In stratiform precipitation, the dominant

microphysical processes are vapor deposition and aggregation of ice particles (Houze, 1993). The magnitude of the convective Z_h and Z_{dr} profiles suggest that collision and coalescence processes are likely occurring, producing larger drops than those observed in the stratiform profile. The stratiform Z_{dr} profile exhibits a sharp increase slightly below the melting level (4 km AGL) inferring that the snow and ice crystals are melting, thus taking on a liquid coating, consistent with the stratiform Z_h profile. A bright band in the stratiform LDR profile is also observed at this height along with a minimum in the $\rho_{hv}(0)$ profile, further confirming the melting process and the presence of mixed phase hydrometeors. Again, this evidence confirms that the algorithms are producing reliable results.

The stratiform LDR profile approaches a value of –26 dB at 7km, while the stratiform K_{dp} profile shows values near zero at this level. These results, combined with the low values of Z_h and Z_{dr}, imply the presence of ice crystals. The stratiform profile of $\rho_{hv}(0)$ is greater than 0.99 and increasing above 7 km, suggesting a uniform distribution of shapes and sizes. This evidence suggests the hydrometeors at this level are of one exclusive type and phase (i.e. exclusively ice crystals). In stratiform precipitation, snow and ice crystals are the dominant hydrometeors found at this level (Houze, 1993). This evidence from the LDR, Z_h, Z_{dr}, and $\rho_{hv}(0)$ profiles suggest the algorithm is correctly identifying stratiform precipitation.

The convective K_{dp} profile indicates much higher values than the stratiform K_{dp} profile, indicating more oblate hydrometeors and a significantly larger amount of liquid water in the lower levels of convective precipitation. This result is not surprising since convective precipitation is generally more intense than stratiform precipitation, and

would exhibit higher amounts of liquid water in the lower levels. However, the low values of K_{dp} in the stratiform profile could also be due to a less dependable estimate of this variable in regions of low Z_h. Nonetheless, the convective K_{dp}, Z_h, and Z_{dr} profiles suggest the algorithm is correctly identifying convection.

a)

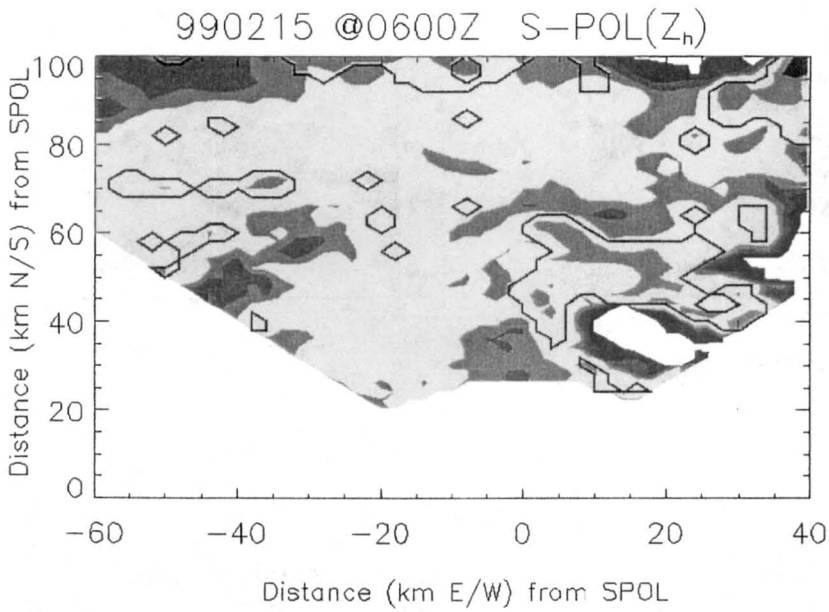

b)

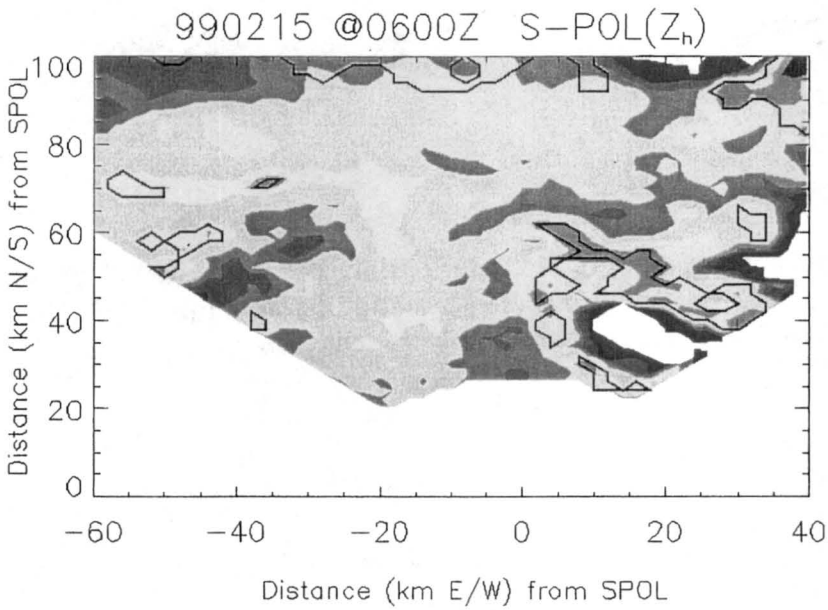

Figure 4.1. Horizontal cross sections of SPOL reflectivity (dBZ) at 1 km AGL on February 15, 1999 (0600), showing S95 results (contour). Results from (a) without and (b) with horizontal reflectivity threshold applied.

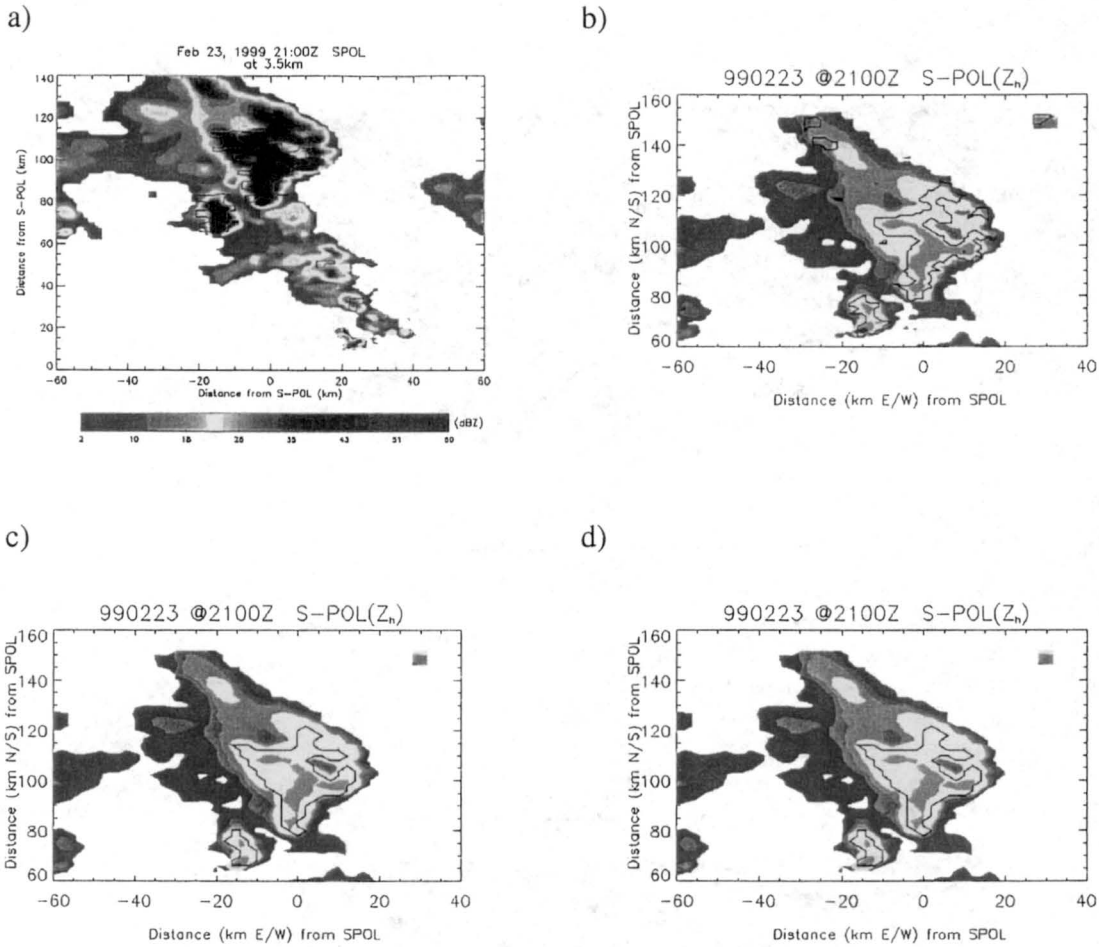

Figure 4.2. Horizontal cross sections of SPOL reflectivity at 1 km AGL on February 23, 1999 (2100), showing classification results (contour). Results from (a) TRMM-2A23, (b) MP, (c) S95, and (d) BL00 algorithms. Note change of scale in (a).

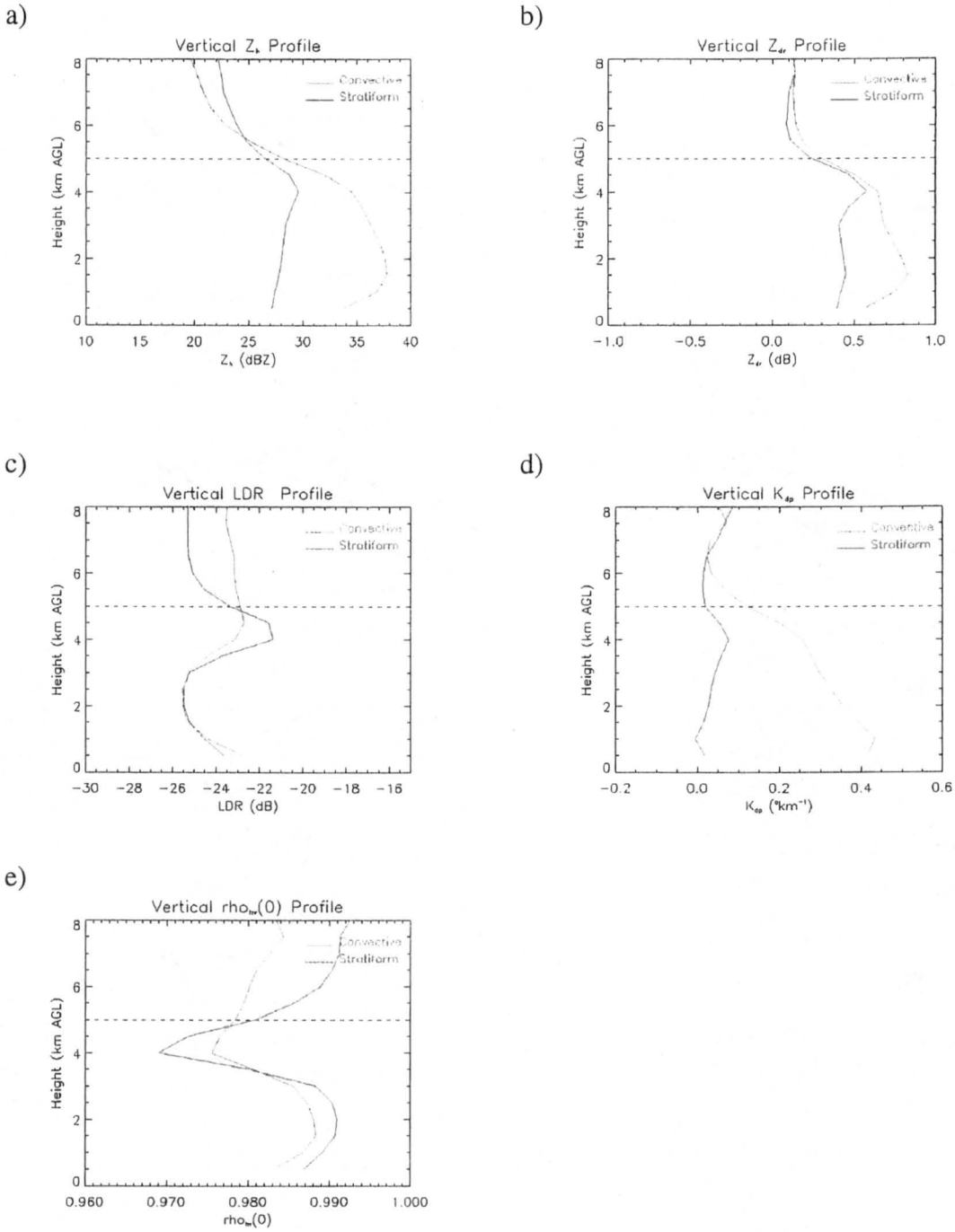

Figure 4.3. Vertical profile of averaged (a) Z_h, (b) Z_{dr}, (c) LDR, (d) K_{dp}, and (e) $\rho_{hv}(0)$ from January 26, 1999 (2100 to 2350) based on MP convective/stratiform classification results. The dashed line indicates the height of the 0° C isotherm.

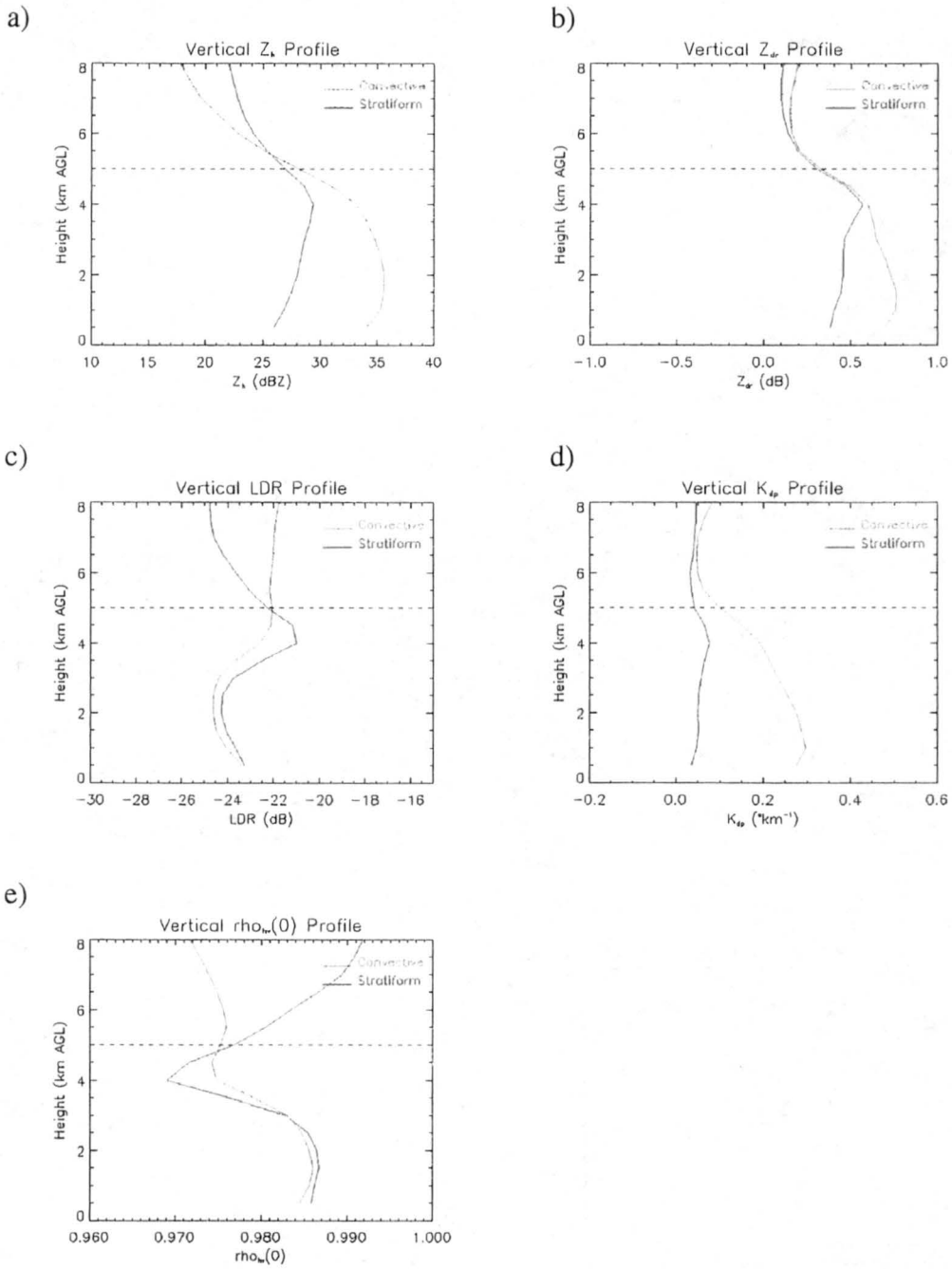

Figure 4.4. Vertical profile of averaged (a) Z_h, (b) Z_{dr}, (c) LDR, (d) K_{dp}, and (e) $\rho_{hv}(0)$ from January 26, 1999 (2100 to 2350) based on S95 convective/stratiform classification results. The dashed line indicates the height of the 0° C isotherm.

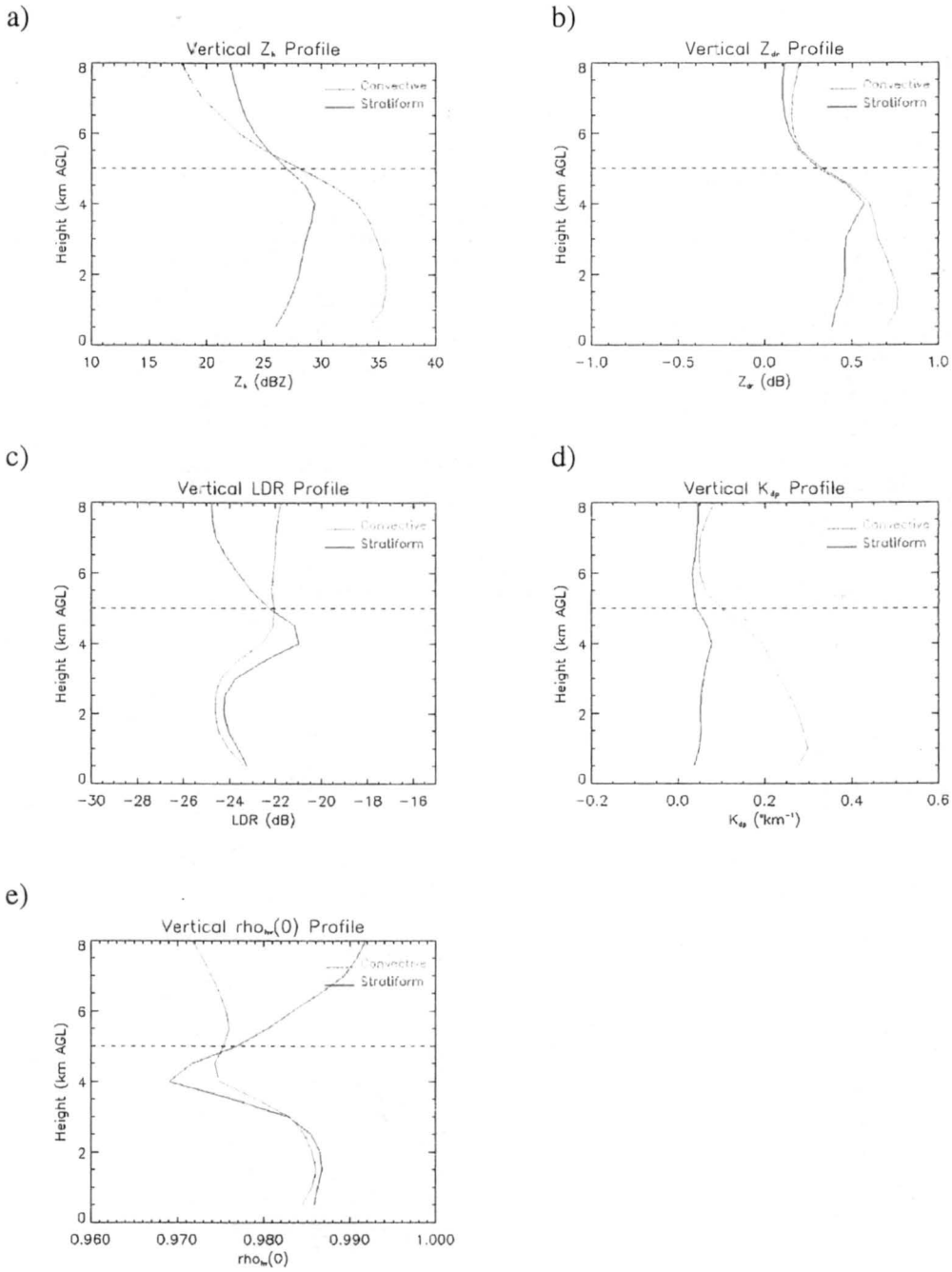

Figure 4.5. Vertical profile of averaged (a) Z_h, (b) Z_{dr}, (c) LDR_{hv}, (d) K_{dp}, and (e) $\rho_{hv}(0)$ from January 26, 1999 (2100 to 2350) based on BL00 convective/stratiform classification results. The dashed line indicates the height of the 0° C isotherm.

	Classification Algorithm			
Time	MP	A99	W95	S95
21:30	C	C	C	C
21:35	C	C	C	C
21:40	C	C	C	C
21:45	C	C	C	C
21:50	S	S	C	S
21:55	S	S	C	S
22:00	S	S	C	S
22:05	S	S	C	S
22:10	S	S	C	S
22:15	S	S	T	S
22:20	S	S	T	S
22:25	S	S	T	S
22:30	S	S	T	S

Table 4.1. Classification results from January 23, 1999.

	Classification Algorithm			
Time	MP	A99	W95	S95
3:40	C	S	T	C
3:45	C	S	T	C
3:50	C	S	C	C
3:55	C	S	C	C
4:00	C	S	S	C
4:05	C	S	S	C
4:10	S	S	S	S
4:15	S	S	S	S
4:20	C	S	S	S
4:25	C	S	S	S
4:30	C	S	S	C
4:35	C	S	C	C
4:40	C	T	C	C
4:45	C	C	C	C
4:50	C	C	C	C
4:55	C	T	T	C
5:00	S	S	S	S
5:05	S	S	S	S
5:10	S	S	S	S
5:15	S	S	S	S
5:20	S	S	S	S
5:25	S	T	S	S
5:30	C	C	C	C
5:35	S	C	S	S
5:40	C	T	C	C
5:45	S	T	C	S
5:50	S	U	T	S
5:55	S	U	T	S
6:00	S	U	T	S
6:05	S	U	T	S
6:10	S	C	S	C
6:15	C	C	S	C
6:20	C	C	C	C
6:25	C	C	C	C
6:30	C	C	C	C
6:35	C	C	C	C
6:40	S	T	T	C
6:45	S	S	T	S
6:50	S	S	C	S
6:55	S	S	T	S
7:00	S	S	S	C

Table 4.2. Classification results from February 15, 1999.

	Classification Algorithm			
Time	MP	A99	W95	S95
17:00	S	S	T	S
17:05	C	C	C	C
17:10	C	C	C	C
17:15	C	C	C	C
17:20	C	C	C	C
17:25	C	C	C	C
17:30	C	T	C	C
17:35	C	U	C	C
17:40	S	U	C	S
17:45	S	U	C	S
17:50	S	U	T	S
17:55	S	U	T	S
18:00	S	U	T	S

Table 4.3. Classification results from February 17, 1999.

	Classification Algorithm			
Time	MP	A99	W95	S95
10:05	S	U	T	S
10:10	S	S	S	S
10:15	S	U	S	S
10:20	S	U	S	S
10:25	S	S	S	S
10:30	S	S	S	S
10:35	S	S	S	S
10:40	S	S	S	S
10:45	S	S	S	S
10:50	S	S	S	S
10:55	S	S	S	C
11:00	S	S	S	S
11:05	S	S	S	C
11:10	S	S	S	S
11:15	S	S	S	S
11:20	S	S	S	S
11:25	S	S	S	S
11:30	C	S	S	C
11:35	C	S	S	C
11:40	C	S	S	C
11:45	C	S	S	C
11:50	S	S	S	S
11:55	S	S	S	S

Table 4.4. Classification results from February 27, 1999.

CHAPTER 5

Summary and Conclusions

We have investigated five precipitation classification algorithms using data from several remote-sensing platforms deployed during TRMM-LBA. The instantaneous results from the A99, W95, S95, and MP algorithms were compared for four of the case studies. The ability of the S95, BL00, and MP algorithms to classify precipitation on the storm-scale was also investigated. This chapter provides a summary of the classification results from each algorithm and recommendations for future research.

5.1 Summary of classification results

The A99 and W95 algorithms have been used to classify precipitation from four TRMM-LBA case studies. The results comprise a total of 430 minutes of precipitation at five-minute resolution. The S95 and MP classification results from the 1-km grid corresponding to the location of the disdrometer and profiler were also used in the analysis.

Of the 430 minutes, the A99 algorithm classified 21% of the precipitation as convective, 8% as transition, 57% as stratiform, and 14% as unclassified. The W95 algorithm classified 36% of the precipitation as convective, 21% as transition, and 43%

as stratiform. The S95 algorithm classified 41% of the precipitation as convective, and 59% as stratiform, while the MP algorithm classified 40% as convective, and 60% as stratiform.

The S95 and MP algorithms provided estimates of the total convective area at 1-km AGL for six TRMM-LBA case studies. The S95 algorithm produced a total combined estimate of 118426 km^2, while the MP algorithm estimated 100942 km^2. The BL00 algorithm provided this estimate for two of the six cases: January 26 and February 23. For these two cases, the S95 algorithm estimated 19096 km^2 of convective area, the BL00 algorithm estimated 14860 km^2, and the MP estimated 18678 km^2.

5.2 Conclusions

The scientific objectives of this study were to develop a classification algorithm using multiparameter radar data, and to apply existing precipitation classification algorithms to the TRMM-LBA data set. These objectives have been accomplished and have provided the opportunity to investigate the performance of each algorithm for a variety of precipitation events.

5.2.1 Development of a multiparameter classification algorithm

The use of multiparameter radar data can lead to accurate precipitation estimates by incorporating the additional measurements of Z_{dr} and K_{dp}. These additional measurements along with Z_h provide information about the size, shape and liquid water

content of the hydrometeors in the radar volume. By including these additional measurements, precipitation estimates can be made that do not rely only on a specific Z-R relationship. However, the ability to accurately estimate precipitation is only the first step in the development of a precipitation classification algorithm.

Once accurate precipitation measurements are made, a rain rate describing convective precipitation is required to classify the precipitation. The threshold of 10 mm h^{-1} was chosen in this study to identify convective precipitation as evidence (see Fig. 2.3b) indicated that most (>90%) stratiform precipitation produced rain rates below this threshold. Since the rain rate describing convective precipitation is variable, the trend in rain rate was also used as a test in the MP algorithm. This additional test permitted the development of a classification algorithm that does not depend on the choice of a specific rain rate describing convective precipitation.

The results produced by the MP algorithm were investigated and compared to four classification algorithms. The qualitative results indicated that the MP algorithm successfully identified the cellular structure of the precipitation events investigated in this study. Furthermore, the quantitative results were shown to be in good agreement with the W95, S95, and BL00 algorithms. In several instances, the algorithm produced errant convective classifications due to high values of Z_h and K_{dp}. However, these misclassifications were typically isolated to small regions.

5.2.2 The application of existing classification algorithms

This study has also investigated the performance of four existing classification algorithms. The A99 and W95 algorithms were applied to the disdrometer and profiler data respectively. The S95 algorithm was applied to the S-pol radar data from six precipitation events, while the BL00 algorithm was applied to two of these cases. Including the A99, W95, S95, and BL00 algorithms provided the opportunity to compare the classification results from five different classification algorithms, each with a different physical basis.

The A99 algorithm failed to classify 14% of the data, and classified the least amount of convective precipitation (21%). This algorithm is highly dependent on the trend in rain rate and is therefore problematic during times in which the disdrometer was not recording precipitation. Furthermore, misclassifications were probable during periods that the disdrometer underestimated the rain rates (see Fig. 2.2). The A99 algorithm was developed from a sound physical basis, however the inaccuracies associated with the disdrometer (i.e. instrument saturation and dead time) had adverse effects on the classification results.

The W95 algorithm was able to classify all of the data from the four cases. The additional thresholds on MZ and MSW improved the results, especially during periods of strong convection. While the W95 classification results appeared to be accurate, validation was conducted using qualitative information from the profiler and radar images. However, the classification results were in good agreement with the S95 and MP algorithms.

The S95 results demonstrated the algorithm's ability to identify the cellular structure in Z_h typically associated with convection. There was however times in which the algorithm produced convective classifications within regions of weaker, homogeneous reflectivity. This type of misclassification occurred in two of the monsoon cases (23 February and 27 February). These cases exhibited less organized convection than the remaining cases, which typically showed a strong convective line preceding the stratiform region. The results from the S95 and MP algorithms tend to indicate that the convective area may have been overestimated for these cases. The S95 and MP instantaneous classification results were in good agreement (within 1%). The accuracy of this algorithm does however depend on the height (AGL) of analysis. For example, if the algorithm were applied at a height in which a bright band in Z_h existed, the area would likely be misclassified as convective.

The BL00 algorithm utilizes the S95 results and also requires additional tests on the horizontal and vertical gradients in Z_h to overcome this problem. In convection, Z_h typically decreases rapidly with increasing distance from the convective core. The use of a horizontal gradient test in Z_h will therefore minimize the potential of misclassifying stratiform precipitation exhibiting high Z_h values (i.e., a bright band). The inclusion of the test on the vertical gradient in Z_h also serves to reduce this type of misclassification. The application of this algorithm does however require complete horizontal and vertical coverage by the radar. Of the six case studies investigated, only two fully satisfied these requirements. In each case, the BL00 algorithm produced lower values of convective area and fraction.

5.2.3 Comparisons between the classification algorithms

The agreement in the instantaneous results between the A99 algorithm and the remaining algorithms was poor. The A99 algorithm is highly dependent on rain rates recorded by the disdrometer. In several instances, the disdrometer failed to record precipitation, even though the co-located rain gauge (G27) was recording precipitation. However, the W95, S95, and MP algorithms were in good agreement, classifying 36%, 41%, and 40% of 430 minutes of precipitation as convective respectively.

The total convective area produced by each algorithm also provided insight into the performance of the S95, BL00, and MP algorithms. Based on the results of the total convective area from all of the cases, the S95 algorithm estimated nearly 17% more convective area than the MP algorithm. However, the S95 and MP results for the January 26 case were in agreement within 2%. The BL00 algorithm estimated 26% less convective area than the S95 algorithm for this case. This result demonstrates the effect of the additional thresholds on the horizontal and vertical reflectivity gradient. However, these results do not provide conclusive evidence that the S95 and MP algorithms are overestimating convection.

5.3 Future research

In many cases, the evaluation of the classification results in this and other studies are based on qualitative analysis, and more tests based on objective analysis would aid in the assesment of the performance of each algorithm investigated here. One such test would

be the incorporation of dual-Doppler derived vertical motion estimates. Stratiform precipitation occurs in regions in which the vertical velocity of the air is less than the terminal fallspeed of ice crystals (Houze, 1993). Therefore, regions with small updrafts (~1-3 m s^{-1}) would confirm the presence of stratiform precipitation, providing an objective means to asses the performance of the algorithm. However, if the precipitation existed within a moderate downdraft, this test alone would fail to identify the type of precipitation occurring.

The focus of this study was on classification algorithms using ground-based data (e.g. radar, disdrometer, and profiler). The results from the MP and S95 comparisons indicate that the S95 algorithm provides reasonable estimates of convective and stratiform precipitation. The BL00 classification results indicated that the additional testing of the reflectivity gradients tends to reduce convective classifications in regions exhibiting uniform reflectivity or steep vertical lapse rates in reflectivity (i.e., a melting layer signature).

One example of a comparison between the ground-based and satellite-based precipitation classification algorithms was presented here (see Fig. 4.2). The validation of the satellite-based precipitation classification algorithm (TRMM-2A23) is necessary in order to obtain accurate diabatic heating estimates from TRMM. The example provided in this study indicated that the TRMM-2A23 algorithm results were in agreement with the S95, BL00, and MP algorithms. However, more comparisons of this type are required to fully assess the performance of the TRMM-2A23 classification algorithm.

References

Atlas, D., and C. W. Ulbrich, 1977: Path- and area-integrated rainfall measurement by microwave attenuation in the 1-3 cm band. *J. Appl. Meteor.*, **16**, 1332-1331.

_ , C. W. Ulbrich, F. D. Marks Jr., E. Amitai, and C. R. Williams, 1999: Systematic variation of drop size and radar-rainfall relations. *J. Geophys. Res.*, **104**, 6155-6169.

Barber, P. and C. Yeh, 1975: Scattering of electromagnetic waves by arbitrarily shaped dielectric bodies. *Applied Opt.*, **14**, 2864-2872.

Biggerstaff, M. I., and S. A. Listemaa, 2000: An Improved Scheme for Convective/Stratiform Echo Classification Using Radar Reflectivity. *J. Appl. Meteor.*, Submitted.

Carey, L. D., and S. A. Rutledge, 1998: Electrical and multiparameter radar observations of a severe hailstorm. *J. Geophys. Res.*, **103**, 13979-14000.

Cifelli, R., and S. A. Rutledge, 1998: Vertical motion, diabatic heating, and rainfall charachteristics in N. Australia convective systems. *Quart. J. Roy. Meteor. Soc.*, **124**, 1133-1162.

Doviak, R. J., and D. S. Zrnić, *Doppler Radar and Weather Observations*, 2nd ed., 562 pp., Academic, San Diego, Calif., 1993.

Garstang, M., H. L. Massie, Jr., J. Halverson, S. Greco, and J. Scale, 1994: Amazon coastal squall lines. Part I: Structure and kinematics. *Mon. Wea. Rev.*, **122**, 608-622.

Gorgucci, E., G. Scarchilli and V. Chandrasekar, 1997: A technique to obtain a multiparameter radar rainfall algorithm using the probability matching procedure. *Il Nuovo Cimento, 20 C, N.2,* 147-164.

Houze, R. A., Jr., 1997: Stratiform Precipitation in Regions of Convection: A Meteorlogical Paradox? *Bull. Amer. Meteorol. Soc., 78,* 2179-2196.

– , *Cloud Dynamics*, 573 pp., Academic, San Diego, Calif., 1993.

Hubbert, J., and V. N. Bringi, 1995: An iterative filtering technique for the analysis of copolar differential phase and dual-frequency radar measurements. *J. Atmos. Oceanic Technol.*, **12**, 643-648.

Jameson, A. R., 1985: Microphysical interpretation of multiparameter radar measurements in rain. Part III: Interpretation and measurements of propagation differential phase shift between orthogonal linear polarizations. *J. Atmos. Sci.*, **42**, 607-614.

Keenan, T., L. D. Carey, D. S. Zrnić, P. T. May, 2000: Sensitivity of 5 cm Wavelength Polarimetric Radar Variables to Raindrop Axial Ratio and Dropsize Distribution. *J. Appl. Meteor.*, Submitted.

Kinnell, P. I. A, 1977: A Preliminary Report on the Commercial Version of the Joss-Waldvogel Rainfall Disdrometer. Division of Soils Divisional Report No. 21, Commonwealth Scientific and Industrial Research Organization, Canberra, A. C. T., Austrailia, ISBN 0 643 02080 2, 12 pp.

Nystuen, J. A, 1999: Relative Performance of Automatic Rain Gauges under Different Rainfall Conditions. *J. Atmos. Oceanic Technol.*, **16**, 1025-1043.

Pruppacher, H. R., and K. V. Beard, 1970: A wind tunnel investigation of the internal circulation and shape of water drops falling at terminal velocity in air. *Quart. J. Roy. Meteor. Soc.*, **96**, 247-256.

Rosenfeld, D., D. Wolff, E. Amitai, 1994: The Window Probability Matching Method for Rainfall Measurements with Radar. *J. Appl. Meteor.*, **33**, 682-693

Rutledge, S. A., R. Avissar, V. Bringi, L. Carey, W. Petersen, E. Williams, J. Wilson, and E. Zipser, 1998: TRMM-LBA Brazil Implementation Plan (Draft), A Science Overview for the NSF Component of TRMM-LBA/Brazil. http://olympic.atmos.colostate.edu/lba_trmm, 1999.

– , W.A. Petersen, R. Cifelli, and L.D. Carey, 2000: Early Results from TRMM-LBA: Kinematic and Microphysical Characteristics of Convection in Distinct Meteorological Regimes. Preprint Volume, American Meteorological Society *24th Conference on Hurricanes and Tropical Meteorology*, Fort Lauderdale, Florida, 29 May - 2 June, 2000.

Ryzhkov, A. V., and D. S. Zrnić, 1995: Comparison of Dual-Polarization Radar Estimators of Rain. *J. Atmos. Oceanic Technol.*, **12**, 249-256.

– , 1998: Polarimetric Rainfall Estimation in the presence of Anomalous Propagation. *J. Atmos. Oceanic Technol.*, **15**, 1320-1330.

Seliga, T. A., V. N. Bringi, 1976: Potential Use of Radar Differential Reflectivity Measurements at Orthogonal Polarizations for Measuring Precipitation. *J. Appl. Meteor.*, **15**, 69-75.

Simpson, J., R. F. Adler, and G. R. North, 1988: A proposed Tropical Rainfall Measuring Mission (TRMM) satellite. *Bull. Amer. Meteor. Soc.*, **69**, 278-295.

Steiner, M., R. A. Houze Jr., S. A. Yuter, 1995: Climatological Characterization of Three-Dimensional Storm Structure from Operational Radar and Rain Gauge Data. *J. Appl. Meteor.*, **34**, 1978-2005.

Tokay, A., D. A. Short, 1996: Evidence from tropical raindrop spectra of the origin of rain from stratiform versus convective clouds. *J. Appl. Meteor.*, **35**, 355-371.

_ , D. A. Short, C. R. Williams, W. L. Ecklund, K. S. Gage, 1999: Tropical Rainfall Associated with Convective and Stratiform Clouds: Intercomparison of Disdrometer and Profiler Measurements. *J. Appl. Meteor.*, **38**, 302-320.

Ulbrich, C. W., 1983: Natural Variations in the Analytical Form of the Raindrop Size Distribution. *J. Clim. and Appl. Meteor.*, **22**, 1764-1775.

Van de Hulst, H. C., *Light Scattering by Small Particles,* pp. 85-102, John Wiley, New York, 1957.

Vivekanandan, J., W. M. Adams and V. N. Bringi, 1991: Rigorous Approach to Polarimetric Radar Modeling of Hydrometeor Orientation Distributions. . *J. Appl.* Meteor., **30**, 1053-1063.

Wallace, J. M., and P. V. Hobbs, 1977: *Atmospheric Science, An Introductory Survey,* 216 pp., Academic, San Diego, Calif.

Williams, C. R., W. L. Ecklund, K. S. Gage, 1995: Classification of Precipitating Clouds in the Tropics Using 915 MHz Wind Profilers. *J. Appl. Meteor.*, **12**, 996-1012.

Appendix A*

Dr. Larry Carey derived the T-matrix estimators using DSD results from the Joss-Waldvogel disdrometer deployed during TRMM-LBA. The individual steps in this derivation are as follows:

1. Obtain processed DSD from the J-W disdrometer data over the complete TRMM-LBA data set.
    - Use Van Wijngaarden-Dekker-Brent method to fit incomplete gamma functions to J-W DSD data (e.g. Keenan et al. 2000)
    - Dead time correction (Kinnell, 1977) applied
    - $R > 0.5$ mm/hr and # drops > 100
    - Gaps between bins allowed
2. T-matrices (e.g. Barber and Yeh, 1975) were calculated for drop diameters ranging from 0.5 to 5.3 mm at 0.1 mm intervals for the drop shape relationship (Keenan et al. 2000) assuming a temperature of 20° C and a wavelength of 10.7 cm (S-band). The incomplete gamma DSD's and appropriate T-matrices were

* The T-matrix method as outlined above was provided by Dr. Larry Carey per personal communication.

3. input to Mueller matrix (Van de Hulst, 1957) scattering code. From the Mueller matrices, radar observables (e.g. Z_h, Z_{dr}, and K_{dp}) were calculated for each gamma DSD, assuming an elevation angle of 1.1^o and a Gaussian distribution of the canting angle with a mean of 0^o and a standard deviation of 10^o (Vivekanandan et al., 1991). The rain rate was calculated from the binned J-W disdrometer data.

4. Multiple linear regression was applied to output from scattering calculations to derive rain rate equations. For equations involving K_{dp}, only DSD's with $K_{dp} \geq 0.25^o$ km^{-1} were utilized.

The following software was used in the development of the T-matrix estimators:

1. T-Matrix and Mueller matrix scattering code: Prof. V. N. Bringi and collaborators at CSU EE with modifications by Dr. Larry Carey.

2. Van Wijngaarden-Dekker-Brent method for estimating incomplete gamma DSD's: Dr. Tom Keenan with modifications by Dr. Larry Carey and Mr. Larry Belcher

3. Multiple Linear Regression code: Dr. Larry Carey